Spectroscopy and Dynamics of Metal Clusters

A thesis submitted for the
degree of Doctor of Philosophy

Suzanne Hamilton

Michaelmas Term, 2010

Supervisor: Dr Stuart Mackenzie

Department of Chemistry

University of Oxford

Spectroscopy and Dynamics of Metal Clusters

Suzanne Hamilton, Wolfson College

A thesis submitted for the degree of Doctor of Philosophy

Michaelmas Term, 2010

A range of spectroscopic and computational techniques have been applied to the study of three metal cluster systems: vanadium monoxide, the Au_2 molecule, and $Rh_nN_2O^+$ clusters.

A new instrument has been built for spectroscopy experiments on metal clusters, consisting of a laser ablation cluster source and a linear time-of-flight mass spectrometer. The instrument was characterised using nitric oxide spectroscopy and applied to the electronic REMPI spectrum of vanadium oxide in the visible region. The rotational constants and band origins of several known states have been determined, and the observation of a new spin-forbidden transition has been used to connect the energies of the quartet and doublet manifolds of VO. A new $3\,^2\Pi$ state was also observed and characterised.

The photoionisation and photodissociation of Au_2 were then studied at 157 nm, and between 35500 and 37200 cm^{-1} with another new instrument recently constructed in the group. Excited and ground state Au photofragments were produced in both spectral regions, and have been detected and assigned using velocity map imaging. The 157 nm photodissociation produced gold atom products in the seven highest-energy accessible channels in a single-photon dissociation process. The complex near-UV spectrum involved two-photon excitation to two 0_g^+ excited states close to their dissociation thresholds, followed by predissociation to thirteen different Au product channels. The branching ratios for dissociation into each of these channels varied across the spectrum as different dissociation limits and curve crossings occurred.

The mid- and far-infrared multiple-photon dissociation spectra of $Rh_nN_2O^+$ clusters have been recorded using the argon-tagging action spectroscopy technique and free electron laser radiation. The results have been compared to density functional theory calculations to deduce the nature of the binding and the likely low-lying electronic and geometrical structures. The N_2O was found to be molecularly adsorbed on the surface of the cluster but, upon infrared heating of the complex via the N_2O vibrational modes, was observed to undergo a reaction, producing N_2 and cluster oxides Rh_nO^+. The reaction is believed to be thermal and mode-independent, but the efficiency of the surface reaction does vary with cluster size, with the $n = 5$ cluster showing no detectable reaction.

Acknowledgements

This thesis would not have been possible without the help and support of a number of people.

Firstly, I would like to thank Dr Stuart Mackenzie for the guidance and great support he has provided throughout my research. None of this work would have been possible without him. I am also very grateful to the rest of the group, especially to Dr Scott Hopkins, whose expertise, patience and unfailing enthusiasm have been an enormous help over the past three years.

Working in collaboration with Dr André Fielicke at the FELIX facility has been a fantastic experience, and my thanks go to him for his generosity in allowing us to use his cluster experiment during our visits there. I would also like to thank the other members of his group for their help in running the experiment and giving advice on the analysis, especially Dr Philipp Grüne, Marko Härtelt and Christian Kerpal. I also greatly appreciate the help that Dr Tiff Walsh and Dr Dan Harding of Warwick University have given me in running calculations to support the FELIX work.

I am also very grateful to the metal workshops of the Oxford PTCL and the Cambridge Chemistry Department, in particular to Simon Dowe for his time and expertise in machining the parts for the time-of-flight instrument. Paul Mitchell and the other members of Lab Services deserve thanks for ensuring that the relocation to Oxford was as smooth as possible.

The computing facilities of the National Service for Computational Chemistry Software (NSCCS) and the Oxford Supercomputing Centre (OSC) were invaluable in performing the density functional theory calculations.

Finally, heartfelt gratitude goes to my parents, Lesley and Dougie, and to my friends in Cambridge and Oxford for their constant encouragement and support.

List of publications

Publications arising from this work

1. W. Scott Hopkins, Suzanne M. Hamilton and Stuart R. Mackenzie, *The electronic spectrum of vanadium monoxide across the visible: New bands and new insight*, J. Chem. Phys., **130**, 144308 (2009)
2. W. Scott Hopkins, Suzanne M. Hamilton, Paul D. McNaughter and Stuart R. Mackenzie, *VUV photodissociation dynamics of diatomic gold, Au_2: A velocity map imaging study at 157 nm*, Chem. Phys. Lett., **483**, 10 (2009)
3. Suzanne M. Hamilton, W. Scott Hopkins, Dan J. Harding, Tiffany R. Walsh, Philipp Gruene, Marko Haertelt, André Fielicke, Gerard Meijer and Stuart R. Mackenzie, *Infrared induced reactivity on the surface of isolated size-selected clusters: dissociation of N_2O on rhodium clusters*, J. Am. Chem. Soc., **132**, 1448-1449 (2010)
4. Suzanne M. Hamilton, W. Scott Hopkins, Dan J. Harding, Tiffany R. Walsh, Philipp Gruene, Marko Haertelt, André Fielicke, Gerard Meijer and Stuart R. Mackenzie, *Infrared-induced reactivity of N_2O on small gas-phase rhodium clusters*, J. Phys. Chem. A, **accepted**

Other publications

1. Dan J. Harding, Tiffany R. Walsh, Suzanne M. Hamilton, W. Scott Hopkins, Stuart R. Mackenzie, Philipp Gruene, Marko Haertelt, Gerard Meijer and André Fielicke, *The structure of Rh_8^+ in the gas-phase*, J. Chem. Phys., **132**, 011101 (2010)
2. Dan J. Harding, Philipp Gruene, Marko Haertelt, Gerard Meijer, André Fielicke, Suzanne M. Hamilton, W. Scott Hopkins, Stuart R. Mackenzie, Simon Neville and Tiffany R. Walsh, *Probing the structures of gas-phase rhodium cluster cations by far-infrared spectroscopy*, J. Chem. Phys., **133**, 214304 (2010)

Contents

Abstract i
Acknowledgements ii
List of publications iii

1 Introduction **1**
1.1 Metal cluster sources 2
1.1.1 Oven sources 2
1.1.2 Sputtering sources 3
1.1.3 Laser vapourisation sources 4
1.1.4 Pulsed-arc cluster ion sources 5
1.2 Geometric and electronic structure of metal clusters 6
1.2.1 Abundance spectroscopy 6
1.2.2 Chemical probes 8
1.2.3 Ion mobility 9
1.2.4 Trapped ion electron diffraction 10
1.2.5 Photodissociation 10
1.2.6 Argon-tagging techniques 15
1.2.7 Photoionisation 16
1.3 Metal cluster reactivity 18
1.3.1 Experimental techniques 19
1.3.2 Cluster reactivity results 20
1.4 Computational studies 21
1.4.1 Density functional theory 22
1.4.2 Applications of DFT to metal clusters 24
1.5 Thesis overview 25

2 ToF instrument **27**
2.1 Overview of the experiment 27
2.2 Design of a new metal cluster source 30
2.3 Cluster detection 32
2.3.1 Time-of-flight mass spectrometry 32

2.3.2 Simulations of ion trajectories . . . 34
2.3.3 Electrode design . . . 37
2.4 Instrument characterisation: REMPI spectrum of nitric oxide . . . 38
2.4.1 Introduction . . . 38
2.4.2 Methods . . . 41
2.4.3 Results . . . 42
2.5 Neutral and cationic vanadium oxide clusters . . . 45
2.5.1 Cationic $V_nO_m^+$ clusters . . . 45
2.5.2 Neutral V_nO_m clusters . . . 47
2.5.3 Cluster formation and mass slippage . . . 48
2.6 Calibration: REMPI spectrum of atomic V . . . 49
2.7 Conclusions . . . 50

3 REMPI spectrum of vanadium monoxide (VO) 53
3.1 Introduction . . . 53
3.2 Methods . . . 55
3.3 Results and discussion . . . 56
3.3.1 Broadband spectra . . . 56
3.3.2 $C\,^4\Sigma^- - X\,^4\Sigma^-$ transition . . . 58
3.3.3 $B\,^4\Pi - X\,^4\Sigma^-$ transition . . . 65
3.3.4 $2\,^2\Pi - X\,^4\Sigma^-$ transition . . . 68
3.3.5 $3\,^2\Pi - X\,^4\Sigma^-$ transition . . . 71
3.3.6 Conclusions and outlook . . . 73

4 Velocity map imaging studies of Au_2 75
4.1 Introduction . . . 75
4.2 Photodissociation . . . 76
4.2.1 Imaging techniques . . . 79
4.2.2 Image reconstruction . . . 82
4.3 Gold clusters and Au_2 . . . 85
4.3.1 Au_2 . . . 87
4.4 Methods . . . 88
4.4.1 VMI instrument . . . 88
4.4.2 Photodissociation imaging experiments . . . 89
4.5 VUV photodissociation of Au_2 . . . 90
4.5.1 One-colour images . . . 90
4.5.2 Two-colour images . . . 93
4.5.3 Conclusions . . . 95
4.6 Near-UV photodissociation of Au_2 . . . 96
4.6.1 Au_2 spectroscopy . . . 97

4.6.2 Au_2 near-UV VMI . . . 103
4.6.3 VMI images across the UV spectrum . . . 107
4.7 Conclusions and future work . . . 109

5 N_2O on rhodium clusters 111
5.1 Introduction . . . 111
5.2 Cluster structure determination by IR-MPD . . . 112
5.2.1 Rare gas tagging . . . 113
5.2.2 IR-MPD of decorated clusters . . . 114
5.2.3 Free electron lasers . . . 115
5.3 Rhodium and adsorbed N_2O . . . 118
5.3.1 Rhodium cluster reactivity . . . 118
5.3.2 Electronic properties . . . 119
5.3.3 Rhodium cluster structures . . . 119
5.3.4 N_2O on rhodium metal surfaces . . . 120
5.4 Experimental methods . . . 122
5.4.1 Argon-tagging experiments . . . 123
5.4.2 Reactivity studies . . . 123
5.5 Computational methods . . . 123
5.5.1 Functional choice . . . 124
5.5.2 Basis sets . . . 125
5.5.3 Structure optimisation . . . 125
5.5.4 Reaction pathways . . . 126
5.6 $Rh_nN_2O^+$ spectroscopy . . . 127
5.6.1 Spectroscopy of the N_2O modes . . . 129
5.6.2 Metal cluster modes . . . 135
5.6.3 Absorptions in the 400-500 cm^{-1} range . . . 141
5.7 Infrared-induced $Rh_nN_2O^+$ reactivity . . . 142
5.7.1 Spectroscopic evidence . . . 142
5.7.2 DFT reaction pathways . . . 147
5.7.3 Discussion . . . 154
5.8 Conclusions . . . 155

6 Conclusions and outlook 158

Bibliography 163

Chapter 1

Introduction

Metal clusters are of interest because they represent an intermediate state between atoms and bulk material, the properties of which are very well understood. Naively, it might be imagined that as clusters increase in size, their physical and chemical properties (e.g. ionisation energies and reactivity) should smoothly and monotonically approach those of the bulk metal. Examples of properties that might be expected to show this trend include dissociation energy,[1] the transition from molecular to dissociative chemisorption,[2] and the appearance of plasmon resonance-like absorptions in clusters.[3]

Many cluster properties, however, do not vary monotonically between the atomic and bulk size regimes. In fact, in many cases, adjacent cluster sizes, i.e., M_n and M_{n+1}, show dramatic differences in their properties. This is particularly true of small clusters ($n < 50$) where it is not unknown for the addition of a single atom to a cluster to change, for example, the reactivity by four orders of magnitude. These dramatic size-dependent properties have led to a whole field of study treating the cluster regime as essentially a different state of matter, and considering explicitly the differences in geometric and electronic structure between neighbouring cluster sizes.[4–6]

In addition to their own unique properties, there is a tantalising possibility that metal clusters may also aid the understanding of the mechanisms of heterogeneous catalysis. Supported metal nanoparticles, and dispersed transition metals in general, are commonly used for catalysis, and even on extended metal surfaces the active sites are often defect sites on otherwise largely unreactive extended surfaces.[7] Metal cluster structures in many ways provide an experimentally and computationally tractable model of these defect sites. By considering clusters to be high concentrations of isolated defects, it is hoped that their catalytic activity can give insight into that of the metal surface.

1.1 Metal cluster sources

The first challenge in the gas phase spectroscopy of metal clusters is to produce atoms and ions of these metals in the gas phase, and then to induce the formation of clusters. Techniques for doing this have been developed over the last five decades, having begun with the conceptually simple sources in which metals are heated in low pressures, to more recent sources where metal is vapourised by intense laser pulses or electric discharges.

1.1.1 Oven sources

The original cluster sources were limited to low boiling-point metals such as alkali metals, but clusters can now be generated from the whole range of transition and main group metals. One of the earliest methods of generating clusters was developed by Robbins *et al.* in the late 1960s.[8] A low boiling-point metal (such as lithium or sodium) was heated in an oven and the resulting gas expands adiabatically through a nozzle, forming a continuous supersonic molecular beam. In this manner, small alkali clusters of a few atoms (up to $n \approx 10$) could be produced.

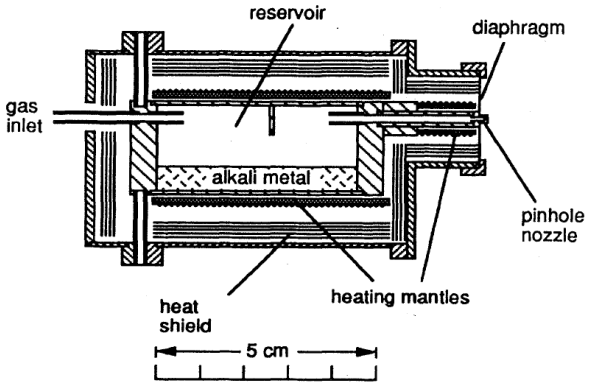


Figure 1.1: Seeded supersonic nozzle source used by de Heer *et al.*,[9] of a similar design to that used by Herschbach.

The design was later improved upon by Herschbach, who used an oven pressurised with an inert gas (Figure 1.1).[10] The metal vapour mixes with the inert gas, which expands to produce a molecular beam, as above. The carrier gas pressure may be several atmospheres, much larger than the partial pressure of the metal vapour, which is typically 10–100 mbar. This leads to more collisions in the molecular beam, including the three-body collisions key to initiating cluster growth, producing colder and hence larger clusters, since hot clusters can cool by evaporation. Clusters of hundreds of atoms can be produced by these seeded supersonic nozzle sources. The distribution can also be tuned crudely to optimise particular cluster size-ranges by careful choice of carrier gas and/or backing pressure.[11]

Both variations of the oven source produce intense continuous beams of clusters, but consume large quantities of material and are limited to metals with boiling points of $T_b < 1500$ K. Consequently, this type of source has typically been used in the study of alkali metal clusters.

1.1.2 Sputtering sources

Sputtering sources involve accelerating rare gas ions towards the metal target. In the case of ion sputtering, an ion gun produces the charged krypton or xenon atoms, which are fired at the metal target with a typical kinetic energy of several keV.[12] In magnetron

sputtering, an argon plasma is trapped in a magnetic field which then accelerates the plasma towards the target.[13]

Developed in the mid-1980s, sputtering sources allowed transition metal clusters to be studied for the first time because a solid metal target could be used. The clusters cool mainly by evaporation, so the measured distribution of cluster sizes reflects their relative stabilities. The clusters produced by sputtering sources tend to be fairly small, up to tens of atoms.

1.1.3 Laser vapourisation sources

The technique of vapourising high melting-point materials with laser radiation has been used for several decades.[14] In 1981, Smalley and Bondybey independently adapted this by entraining the metal vapour in a molecular beam to produce an intense, pulsed cluster source.[15,16] An inert gas is flowed over a metal target as it is ablated by a pulse of laser light (typically from a Nd:YAG or excimer laser) which produces a plasma of metal atoms and ions. The carrier gas flows through a nozzle and expands to produce a molecular beam. As the beam cools and expands, the metal atoms condense into both charged and neutral clusters.

Improvements were made to this source by extending the channel before the start of the free expansion from several millimetres to several centimetres. This increases the number of three-body collisions (necessary for clustering), resulting in the generation of larger clusters.[17] Cooling of the metal clusters by supersonic expansion can be improved by cryogenic cooling of part of the source, typically the clustering channel, such as the source used by Fielicke *et al.* with a channel surrounded by a reservoir of liquid nitrogen to reduce the temperature to 80 K.[18]

The original source designs contained an immobile sample of the metal of interest which over time is drilled into by the laser pulses. This was replaced by a rod or disc

target which could be rotated to expose a fresh metal surface to each ablation laser pulse.[17,19]

The intense local heating of the target by the laser pulse means that any metal can be used, without the limitations of the oven sources in which the whole of the cluster source had to be heated. Another feature of laser ablation sources is that they are inherently pulsed, because the intense radiation required for ablation typically comes from a pulsed laser, usually an excimer or Nd:YAG laser. The cluster production per second is typically low compared to the oven sources, with the result that although tiny quantities of the material are used, the maximum intensities within a gas pulse may be much higher. High instantaneous number densities are useful in pulsed laser spectroscopy experiments, and also in time-of-flight mass spectrometry, a common method of cluster detection. Both of these techniques will be used extensively in this project.

1.1.4 Pulsed-arc cluster ion sources

Neutral and ionic clusters can also be generated by vapourising the metal in an intense electric discharge, known as a pulsed-arc cluster ion source (PACIS). This source was developed in the early 1990s by Ganteför *et al.*, and can be used on a wide range of different metals.[20,21] The helium backing gas is pulsed between two electrodes which are connected to a capacitor. When the capacitor discharges the electrodes arc, forming a plasma which erodes the surface of the metal. The metal ions cool and condense through collisions with the carrier gas.

The PACIS is a more intense source than the laser vapourisation source discussed above (Section 1.1.3), can operate at higher repetition rates, and can vapourise liquids like mercury. However, the electric arc also converts the helium into a plasma, requiring more cooling than is needed in a laser vapourisation source.

1.2 Geometric and electronic structure of metal clusters

Determining the structure of metal clusters remains a challenging task for both experiment and theory. Traditional absorption spectroscopy techniques, even modern variants like cavity ring-down spectroscopy, are of little use because of the low concentrations of each cluster species (typical laser vaporization sources, for example, can generate around 10^6 clusters, ~ 1 attomole, of a particular size per pulse). The dipole moments of bare metal clusters are typically very small, so vibrational transition intensities are also small. Spectroscopic techniques typically used for trace detection such as cavity ringdown spectroscopy[22] and laser induced fluorescence have been applied to metal atom diatomics[16] and triatomics,[23] but even these are not generally sensitive enough to record cluster spectra.

Indirect methods of structure determination are common, however. These are typically based on mass spectrometric techniques, taking advantage of the ability to detect charged species with 100 % efficiency, so studies of ionic clusters are more common, but neutral clusters can also be investigated by action spectroscopy (Section 1.2.5) followed by ionisation and detection. Ab initio calculations are usually required to interpret the experimental spectra. The calculations are themselves challenging for transition metals with many *d*-electrons, and theoretical treatments of clusters are usually limited to the level of density functional theory.

1.2.1 Abundance spectroscopy

The simplest view of the structure of metal clusters is the jellium model in which it is assumed that clusters are spherical, positively charged spheres filled with an electron gas. The solutions to the time-independent Schrödinger equation for this potential are

orbitals with quantum numbers n, l and m_l, analogous with atomic orbitals. Clusters with the correct number of electrons to fill one of these shells are predicted to be particularly stable relative to clusters of neighbouring sizes, by analogy with electron shells in atoms. Using a potential which is intermediate between a three-dimensional spherical and square well potential, "magic number" clusters with closed shells are predicted to occur at n_e = 2, 8, 18, 20, 34, 40, 58, etc. For metals with one valence electron, the number of atoms in the most stable neutral clusters should also take these values.[24]

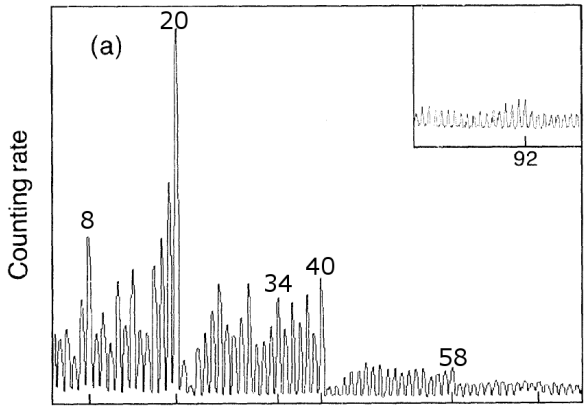


Figure 1.2: Sodium cluster abundance spectrum. Magic numbers are indicated above the relevant peaks. Large steps in abundance between closed shell clusters and larger clusters are present because larger clusters cool by evaporation until they reached a stable structure (after Knight *et al.*[24])

Given the crudity of the approximation involved, the agreement with experiment is surprisingly good for s^1 metals. Mass spectra of alkali metal clusters show peaks in abundance at the predicted magic numbers (Figure 1.2).[24] Similar peaks are also seen in abundance spectra of clusters of the coinage metals, which also have an electronic configuration of s^1,[12] though these are less prominent than those of the alkali metals.

The jellium model is less appropriate for metals with more electrons, however, even for the alkaline earths. Instead, for Be and Mg, peaks are observed which do not correspond to those predicted by the Jellium model but instead to geometrical structures consistent with icosahedral clusters.[25] Magic numbers due to closed electronic shells have not been observed for transition metal clusters, except the coinage metals. Bonding in these metals is typically more covalent and less delocalised compared to the alkali metals, so the jellium model is less applicable. An additional complication, however, is the

methods used for forming clusters of these types: alkali metal clusters are usually produced in oven sources (Section 1.1.1), and grow in equilibrium conditions, whereas the growth of transition metal clusters is limited by collisions in laser vapourisation sources (Section 1.1.3). Cold sodium clusters produced by laser vapourisation show much more uniform size distributions.[26]

1.2.2 Chemical probes

One indirect method used extensively for transition metal structure determination is to saturate the cluster surface with an adsorbate, and infer from this the number and geometry of surface binding sites.[27] This chemical probe technique was developed by Riley *et al.*, and has been used to investigate clusters of nickel, cobalt and iron atoms.[28]

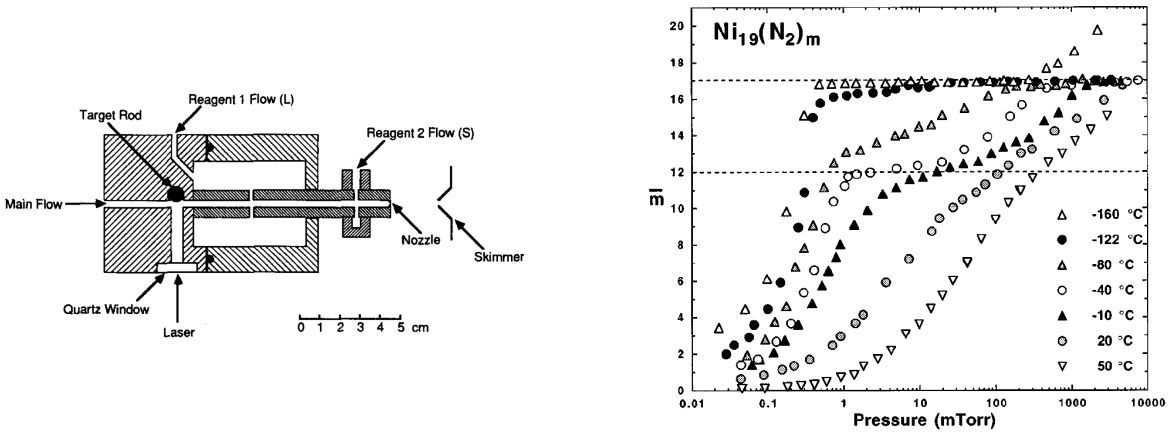


Figure 1.3: Chemical probe source design and flow-tube reactor (left),[29] and typical uptake plot of N_2 on Ni_{19} (right).[30] Two plateaus with $m = 12$ and $m = 17$ suggest that there are 12 of one geometry of surface atom, and 5 of another.

Clusters are produced in a laser vapourisation source in a flow of helium at the start of a flow-tube reactor (Figure 1.3). Once clusters have formed, the adsorbate gas is introduced into the channel at a controlled temperature and pressure. The reaction products expand from the end of the channel and the clusters are ionised and detected in a time-of-flight mass spectrometer.

The mass spectra are converted to plots of the average number of adsorbed molecules

with respect to reactant pressure. Plateaus in the uptake indicate that a binding site on the cluster has become saturated. For reactants like N_2 which can adsorb on several different binding sites, there are multiple adsorption plateaus, as can be seen in the example in Figure 1.3. The number of metal atoms of each geometry are then compared with likely cluster geometries in order to identify the structure.

1.2.3 Ion mobility

Another approach to measuring an ionic cluster's structure is ion mobility. First applied to the study of metal clusters by Kappes,[31] ion mobility is based on the principle that the time taken for an ion to traverse a pressurised cell will be proportional to its collision cross-section with a background buffer gas. By measuring the flight time of a cluster guided by an electric field through such a cell, its cross-section can be determined and compared with theoretical predictions. A time-of-flight mass spectrometer first size-selects a cluster with the required *m/z* before the drift cell, and a quadrupole mass spectrometer placed after the drift tube prevents fragmentation products reaching the detector.[32]

Kappes *et al.* have used ion mobility studies in conjunction with density functional theory simulations to determine that gold cluster cations of seven atoms or less are flat, and that the transition to more chemically intuitive three-dimensional geometries occurs at $n = 8$.[33]

Different isomers are readily identified by ion mobility, provided that they have different cross-sections, appearing as multiple peaks on the time-of-flight spectrum. Au_9^+ is one such cluster; its two isomers are predicted by DFT to have prism-like structures which can interconvert by breaking a single metal-metal bond. The cluster temperature can be controlled by cooling the helium buffer gas, and this allowed the determination of the temperature at which the isomers can interconvert. Below 140 K, both isomers of

Au_9^+ are identifiable in the beam, but their time-of-flight trace converges to a single peak when heated above this temperature.[34]

1.2.4 Trapped ion electron diffraction

Trapped ion electron diffraction (TIED) was pioneered by Parks *et al.*, who tested the concept on C_{60}^+ molecules.[35] A single cluster size is isolated in a radio-frequency quadrupole trap (see Figure 1.4). The trapped clusters are irradiated by a beam of electrons, and the resulting diffraction pattern is captured on a CCD camera. The diffraction pattern is compared to that predicted by a scattering function based on structures calculated by density functional theory.

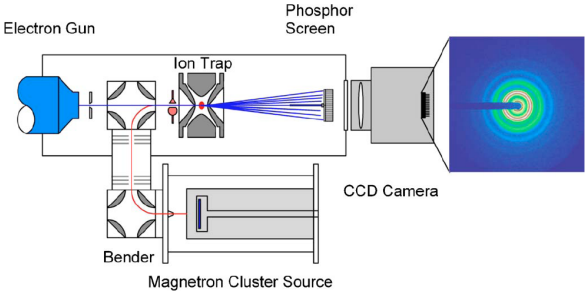


Figure 1.4: Schematic of the TIED experiment used by Kappes.[36]

Best suited to larger clusters, TIED has been applied to gold and silver clusters by Kappes *et al.* Evidence for a chiral cluster was found in their investigation of Au_{34}^- anions,[37] and Jahn-Teller distortions have been observed in Ag_{55}^- anions.[38]

1.2.5 Photodissociation

Although direct absorption by metal clusters is difficult to measure, absorption spectra can be measured indirectly using *action spectroscopy*, in which the vibrational or electronic excitation of the photon causes a more readily measurable change in the cluster. Key in the study of bare metal clusters and metal-containing clusters is photodissociation spectroscopy, whereby one or more photons are absorbed by a cluster, which

subsequently fragments. The mass spectrum of the fragments (after ionisation in the case of neutral clusters) is compared to the mass spectrum of the nascent clusters. Depletion of the parent peak and/or the growth of a fragment peak provides a signal for absorption by the parent cluster. Photodissociation spectroscopy may be used to study neutral and ionic species, and both electronic and vibrational spectroscopy are possible if the absorption provides enough energy to break bonds within the cluster.

Ionic clusters held in ion traps can be photofragmented in order to determine their dissociation energies.[39] The Penning trap allows the cluster of interest to be mass-selected, and all of its dissociation products to be detected. Comparing the fragment cluster distribution as a function of time with a theoretical model of dissociation rates allows the cluster dissociation energies to be calculated.[40]

Photodissociation spectroscopy experiments, however, typically use time-of-flight (TOF) spectrometers as the cluster detection method. These have lower resolution than, for example, Fourier transform ion cyclotron resonance (FT-ICR) cells and other ion traps, but their sensitivity is excellent: microchannel plate (MCP) detectors can, in principle, detect single ions with *ca.* 100 % efficiency, at least in the case of light ions. This feature makes photodissociation spectroscopy a more sensitive tool than absorption spectroscopy, in which the depletion of a small fraction of a light-source needs to be detected from a large background.

Linear TOF spectrometers will be discussed in more detail in Section 2.3. In application to clusters, neutral clusters are ionised between two plate electrodes, one of which has a grid in the centre to allow the passage of ions. A potential difference applied across the grids accelerates the ions in the direction of the detector. After passing through the first grid, the ions enter a stronger electric field which accelerates them to their final velocity, before traversing a longer field-free region. The same kinetic energy is imparted to all ions created at the same place, so ions with a smaller m/z leave the electric

field with a higher velocity, and so reach the detector before the larger ions. Accurate measurement of the arrival times (and therefore the time-of-flight) thus permits the determination of m/z for species present. Three-electrode TOF spectrometers of this type compensate for the initial distribution of the ions in space.[41]

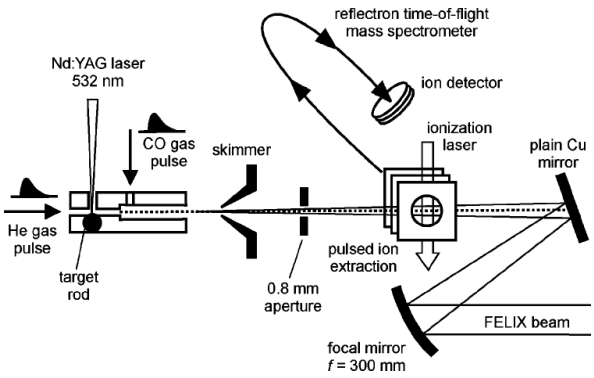


Figure 1.5: Mass spectrometric analysis of clusters after photodissociation and ionisation, using a reflectron (after Fielicke *et al.*[42])

Reflectron TOF spectrometers, such as that used by Fielicke *et al.* (Figure 1.5) have two sets of electrodes. The first are similar to those in a linear TOF, and these space-focus the ions into a second series of grids which decelerate the ions and reflect them at a small angle onto the detector. The deceleration and subsequent acceleration increases the ions' time-of-flight, giving better separation of different masses. Resolution is also improved by compensation for the ions' original kinetic energy: ions which started with higher on-axis kinetic energy penetrate further into the reflection region, which increases their time of flight to be closer to that of ions with lower kinetic energies.[43]

The study of neutral clusters is limited to the techniques just described, but ionic clusters may be additionally mass-selected before photodissociation, as well as after. Duncan *et al.* accomplish this using a modified reflectron TOF design (Figure 1.6).[44] All of the ionised clusters are accelerated in the first electric field, but once the different masses have separated, the pulsed mass gate deflects all cluster ions other than the one of interest. The mass-selected clusters are photodissociated in the reflector region, which then acts as a second TOF spectrometer to separate the different product fragments.

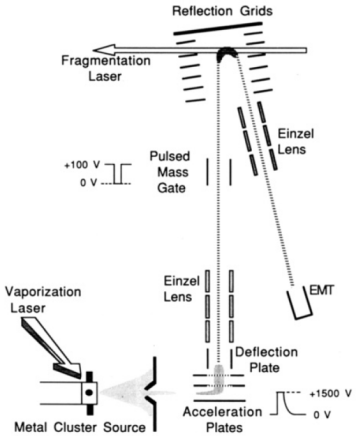


Figure 1.6: Photodissociation of ions in a reflectron time-of-flight mass spectrometer (after Duncan *et al.*[45])

Photodissociation spectroscopy has been used to study bare metal clusters and metal-containing clusters. Photofragmentation of bare metal clusters is possible if the metal-metal bonds are relatively weak. For example, Knight *et al.* found evidence of the surface plasmon resonance in the visible region absorption spectrum of small neutral sodium clusters.[46] The coinage metals have also been studied by photodissociation: for example, the vibrational band structure of Cu_4^+ was observed in its electronic spectrum,[47] and plasmon-like bands in the structure of small silver ions have also been studied.[3]

Metal-containing clusters

Metal-containing clusters and metal clusters with molecularly adsorbed ligands are excellent species for investigation by photodissociation studies because they typically contain a relatively weak metal-ligand bond which may be easily broken, illustrated in Figure 1.7. Many of the molecules commonly used in surface science studies have large dipole moments and hence strong vibrational absorptions. These clusters are of interest for several reasons, described below.

Mass-spectrometric measurements alone can provide kinetic measurements such as reactivity constants, but any structural information must be inferred. Structural determination of metal clusters with adsorbed molecules can be performed by analysing vibrational spectra of the adsorbates, which should also lead to a better understanding

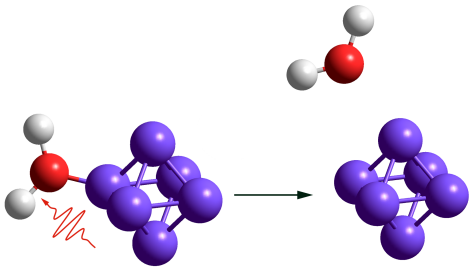


Figure 1.7: Schematic of infra-red photodissociation.

of their reactivities. The vibrational modes of adsorbed molecules are perturbed by the presence of the cluster or metal atom, which thus alters the absorption spectrum. The vibrational frequency of carbon monoxide, for example, is particularly sensitive to the nature of the binding site, since it forms a bond by sigma-donation to the metal surface and by accepting electron-density (back-bonding) into its π^* orbital. Carbon monoxide on small (n = 3 or 4) cationic rhodium clusters exhibits absorption peaks at lower frequencies compared to larger clusters, suggesting that the nature of the binding site changes with cluster size. Back-bonding of electron density into the CO π^* is greater for anionic clusters, and so the shift in the CO vibrational frequency is larger for anions than neutrals, and even lower on cations.[42]

Logically, the adsorption behaviour of a molecule on a cluster should, at some large cluster size, become indistinguishable from that adsorbed on an extended metal surface. Several studies have looked at how the ligand vibrational frequency changes with increasing cluster size. For example, the infrared photodissociation spectra of CO adsorbed on rhodium clusters[48] and water adsorbed on vanadium clusters[49] both show that the vibrational frequency of the ligand approaches that of a surface-adsorbed molecule when the metal cluster size is of the order of 10 atoms.

Rather than varying the size of the metal cluster, metal atoms with differing number of ligands can also be produced, which allows the onset of solvation effects to be studied.[50] Ammonia bonded to sodium atoms in $Na(NH_3)_n$ clusters shows two distinct peaks

in the N–H symmetric and antisymmetric stretching region until $n \geq 7$, when the absorption becomes a broad peak covering the same spectral region. This was interpreted as six ammonia molecules bonded directly to the sodium atom, with subsequent molecules forming a second solvation shell.[51]

1.2.6 Argon-tagging techniques

The photodissociation action techniques described above are limited to clusters containing a relatively weak bond. Even strongly-bound clusters can by studied by photodissociation spectroscopy, however, by introducing a new, weak bond into the system.[18] The principle is illustrated in Figure 1.8. The cluster of interest is "tagged" with one or more noble gas atoms, typically argon, which is bound weakly to the cluster. When the cluster or an adsorbed molecule absorbs a photon, the energy of the photon breaks the cluster-argon bond following rapid intramolecular vibrational redistribution. The depletion of the cluster-argon peak in the mass spectrum, or equivalently the growth of the naked cluster mass peak, signals an absorption by the cluster. The dissociation energy of a cluster-argon bond is low, around $400\,\mathrm{cm}^{-1}$ for cationic clusters, allowing single-photon absorptions to be detected even in the infrared region.

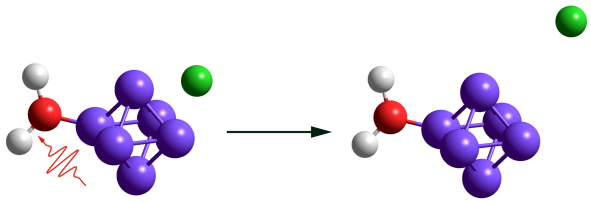


Figure 1.8: Schematic of infra-red photodissociation combined with argon tagging.

Argon is typically used because, unlike neon, krypton and xenon, it is monoisotopic, which simplifies the mass spectrum. Argon is also chosen as the inert tag because the metal-argon bond is stable enough to be able to form measurable numbers of argon-tagged clusters in an experiment, but does not perturb the electronic structure of the

cluster as much as would the more polarisable krypton or xenon atoms. It has been found that the presence of an argon atom can shift the position of electronic absorptions by around 0.1 eV in extreme cases.[52] Vibrational peaks are usually shifted by less than $10\,\mathrm{cm}^{-1}$.[18,53] In some cases the presence of the rare gas can cause IR-inactive modes to become active, producing large changes in the spectrum, but this is limited to small clusters with $n \leq 5$.[54]

The vibrational frequencies of bare metal clusters are in the far infrared region of the spectrum, so the weak cluster-argon bond enables these to be studied using photodissociation action spectroscopy. Fielicke *et al.* have used a free electron laser (FELIX in the Netherlands) to generate light in the far-infrared for the study of the vibrational structure of vanadium,[18] silver[53] and niobium[55] clusters. Photodissociation of metal-containing clusters has also been applied to the vibrational spectrum of water adsorbed to single metal ions, for example complexes of water with several different transition metals[56,57] and main group metals.[58]

This technique will be discussed in more detail in Chapter 5 where it is applied to $Rh_nN_2O^+$ complexes.

1.2.7 Photoionisation

The electronic structure of metal clusters can be probed by ionising the clusters, either from the neutral or anion state, using a variety of techniques. Photoionisation was one of the first spectroscopic techniques applied to gas-phase metal clusters, and was used to determine ionisation potentials as a function of cluster size.[59,60] The ionisation potential of many transition metal clusters decreases with cluster size, with some non-monotonic variation for small clusters, and approaches the bulk work function value as the cluster grows to hundreds of atoms: examples include cobalt, iron, niobium and tantalum.[61–63] These differ from the ionisation potentials of alkali metal[64] and coinage

metal clusters,[65,66] which show odd-even oscillations and certain clusters with anomalously high IPs due to electronic shell-closings described in Section 1.2.1.

Small clusters are also amenable to vibrationally-resolved ionisation studies, which yield more information on the geometric as well as the electronic structure of the clusters. Resonance-enhanced multiphoton ionisation (REMPI) spectra of transition metal dimers and trimers can be used to identify excited electronic states and their spectroscopic parameters. REMPI spectra have been recorded for Au_2,[67] Ni_2,[68] AgK,[69] NiAu and PtCu,[70] in some cases with rotational resolution. Vibrationally-resolved spectra of several coinage metal trimers have also been recorded.[71–73]

Another way of obtaining vibrationally-resolved ionisation spectra is through the zero electron kinetic energy (ZEKE) technique, which can yield high-resolution information on the spectroscopic constants of the neutral cluster and its cation. The cluster is photoexcited to a Rydberg level just below an ionisation threshold. A pulsed electric field then ionises the clusters and accelerates the electrons towards the detector. ZEKE has been applied to small bare metal dimers like V_2 and Ag_2,[74,75] and to larger complexes such as Nb_3O and Y_3C_2.[76,77] A review by Yang and Hackett summarises the applications of PFI-ZEKE to metal clusters from before 2000.[78] Where there are several species present in the mass spectrum, and therefore more than one possible source of electrons, mass slippage in the molecular beam can be used to distinguish the ZEKE spectra of the different clusters.[79] Much higher mass-resolution can be achieved by using the related technique of mass-analysed threshold ionisation (MATI), in which the field-ionised clusters are detected using mass spectrometry, rather than collecting the electrons.[80]

The production of metal cluster anions opened up the possibility of performing photoelectron spectroscopy (PES) on clusters.[81] Here, the anionic clusters are photoionised, and the kinetic energies of the photodetached electrons are measured. The electron kinetic energy is dependent on the final internal energy of the neutral cluster, provid-

ing information on its electronic and vibrational states as well as the cluster's electron affinity. Copper, silver and gold are found to have electron affinities which show similar odd-even oscillations and shell closings to their ionisation potentials.[82] The gaps between peaks in the PES of titanium and chromium oxide clusters approach the bulk band gap value with increasing cluster size.[83] For clusters which have more than one stable geometry, isomer-specific spectra can be recorded by titrating away the more reactive species.[84]

The photoelectron's kinetic energy can also be determined using velocity map imaging (VMI), in which the electrons are recorded by a position-sensitive detector, and their kinetic energies are calculated from their distance from the point of ionisation. This method also measures the angular distribution of the electron, which provides additional information on the molecular orbital symmetries of the clusters.[85] The anisotropy parameters of Hg_n^- photoelectrons evolves smoothly with cluster size as the electronic structure changes towards the bulk structure.[86] Vibrational resolution in gold hydride photoelectron images has been used to determine the structure of small clusters.[87]

1.3 Metal cluster reactivity

The reactivity of metal clusters with small organic and inorganic molecules is of great interest because of their relevance to heterogeneous catalysis. Ionic clusters can be mass-selected, so their reactivity and catalytic activity can be analysed as a function of cluster size. The most common techniques for studying the reaction kinetics of charged gas-phase clusters are described below.

1.3.1 Experimental techniques

In Fourier transform ion cyclotron resonance (FT-ICR) experiments, cluster ions are entrained in a molecular beam and then guided into an ion cyclotron resonance (ICR) cell. The magnetic field in the ICR cell traps the ions in circular cyclotron orbits with mass-dependent frequencies. The motion of the orbiting ions induces currents in a pair of detector plates positioned nearby. The Fourier transform of this measured image current gives the mass spectrum of the cell contents. Ions of a specific m/z can also be isolated by ejecting all other ions using radio-frequency pulses of the magnetic fields. A reactant gas is then leaked into the cell, which is filled to a known pressure (typically 10^{-8} mbar). The mass peak due to the reactants and all products can be followed with time, and from these the reactivity constants can be extracted. The reaction can be followed for several minutes since the loss rate of ions trapped in the ICR cell is very low.[4,88–90]

An alternative method of measuring ion reactivities is in a collision cell. The cluster of interest is selected using a quadrupole mass-filter and is then guided by an octopole ion guide through a collision cell pressurised with the reactant gas. The products are determined by mass spectrometry using a second quadrupole.[91–93] Electron multiplier detectors, which can detect single ions, are used in these experiments, so despite the poorer mass resolution of the quadrupole mass spectrometer, the sensitivity is much higher than that of FT-ICR. The velocity of the cluster within the cell can be accurately tuned using the octopole ion guide, allowing reactivity to be measured as a function of collision energy.[94,95]

FT-ICR and ion beam experiments can only be used on ions, but neutral clusters as well as ions can be studied using fast-flow reactors. Here, a reaction tube is placed immediately after the metal cluster source. This can be injected with one or more gases to mix with the carrier gas and react with the clusters as they exit the source. Following the reactor, the mixture expands into vacuum as a molecular beam, which, if neutrals

clusters are being studied, is intersected by a photoionisation laser in the extraction region of a mass spectrometer.[96]

1.3.2 Cluster reactivity results

Small clusters of some metals exhibit very different reaction rates with bulk metal surfaces,[97] and their reactivity is often strongly size-dependent: rhodium cluster reactions with N_2O or alkanes,[5,98] H_2 reactions with iron clusters,[99] and methanol reactions with cobalt clusters[100] all exhibit reaction rate constants that vary by several orders of magnitude between adjacent cluster sizes. Some metals show this variation in reactivity only with certain reactants. For example, O_2 reacts rapidly with niobium clusters at close to the collision rate, while N_2 and H_2 reactions are slower and size-dependent.[6]

The reason for these reactivity trends depends sensitively on the underlying cluster geometry and its electronic structure: the reactivity of N_2 with tungsten increases with cluster size, and appears to be dependent on the number of open surface sites available for dissociation,[101] while the Nb_n reaction rates show an inverse correlation with the cluster ionisation potential.[6] The electronic shell closings of the coinage metals influence their reactivity with oxygen, which reacts much more rapidly with gold, silver and copper cluster anions with an even number of atoms than an odd number.[102] Other studies have found that reactivity trends are due to both electronic and geometric structure: neutral copper clusters which are particularly unreactive are those with closed electronic shells, while some especially reactive clusters cannot be explained electronically but are geometric magic numbers with closed icosahedral shells.[103]

The influence of electronic structure on reactivity can also be seen in the dependence of reactivity on cluster charge state. Perhaps the most striking example is for the reaction of gold with O_2, which adsorbs on anionic clusters but not on cations (with the exception of $n = 10$), while the reverse is true for H_2 adsorption.[104] Other examples include CO

adsorption on vanadium, niobium and tantalum clusters, which for $n < 15$ react around 50 times faster in their cationic forms than as anions,[105] and anionic rhodium clusters, which show much less size-dependence than the corresponding cations in reactions with N_2O.[5]

Different isomers of an individual cluster size, whether geometric or electronic, can also have strikingly different reactivities. The presence of isomers has been inferred from biexponential decays in the cluster intensity over the course of a reaction, for example in the reaction of Rh_6^+ with NO,[106] or the reaction of N_2O with Rh_{12}^+, whose isomers' reactivities differ by more than two orders of magnitude.[5]

1.4 Computational studies

Determining the origin of the variations observed in cluster reactivity is one of the motives for many of the electronic and geometric structure experiments described in Section 1.2. Interpretation of these studies often requires quantum chemical calculations of the different cluster isomers and their interaction with other molecules.

Early metal cluster experiments were often interpreted with simple models like the jellium model or icosahedral packing models.[107] These models worked well for alkali and coinage metal clusters, but cannot describe the complexity of clusters of most transition metals. The large number of electrons in transition metal clusters make calculations computationally expensive. High-level calculations based on electron correlation, such as Møller-Plesset perturbation theory and coupled cluster methods, have been applied to only very small clusters of a few atoms.[108–110] Due to their computational cost, density functional theory (DFT), whose costs scale better with system size, is often chosen as a compromise between accuracy and computational efficiency.[111]

1.4.1 Density functional theory

DFT is based on the theorem of Hohenberg and Kohn which states that the electronic energy can be determined by the total electron density, given by Equation 1.1.[112]

$$\rho(\boldsymbol{r}) = \sum_{i=1}^{N} |\psi_i(\boldsymbol{r})| \tag{1.1}$$

where $\psi_i(\boldsymbol{r})$ are the molecular orbitals. The density depends only on three spatial coordinates, whereas the electron density described by the wavefunctions has $4N$ variables: three spatial and one spin coordinate for each electron. Hohenberg and Kohn also showed that the variational principle applies, so the ground state density can be found by minimising the energy. The aim of DFT is to find the best way to calculate the energy directly from the density. The methods of doing this are called density functionals, of which many have been developed.

Types of density functional

Attempts to build functionals which are only dependent on the density are only applicable to some metallic systems because they assume a uniform electron gas.[113] Most modern density functionals use molecular orbitals to calculate the kinetic energy of the electrons, which are assumed to be non-interacting. The exchange and correlation components, both of which are functionals of the density, are then added in order to account for the interaction of the electrons. The simplest of these models is the Local Density Approximation (LDA), which assumes that the density is locally uniform. The expressions for exchange and correlation are only dependent on the electron density, but different parameters are used by the various LDA functionals, such as the VWN functional of Vosko, Wilk and Nusair, or the PW functional of Perdew and Wang.[114]

Including the first derivative of the density as a variable in the exchange and cor-

relation functionals improves the accuracy of the energy compared to LDA approach. This model is called the Generalised Gradient Approximation (GGA), and includes empirical functionals whose parameters are fitted to experimental data like that of Lee, Yang and Parr (LYP),[115] and ab-initio functionals such as Perdew-Burke-Ernzerhof (PBE), whose parameters were chosen to produce physically correct values for some limiting cases.[116]

Meta-GGA functionals include second-order derivatives of the gradient to try to further increase the accuracy. Again, there are some empirical meta functionals, such as VSXC which has 21 parameters fitted to experimental data,[117] and some ab initio functionals. Tao-Perdew-Staroverov-Scuseria (TPSS) is one such functional, which was developed as an improvement to PBE.[118]

A further step is to combine the exchange density functional (which can be either a GGA or meta-GGA functional) with a proportion of Hartree-Fock exchange, which is calculated using molecular orbitals, producing what is known as a hybrid functional. The three-parameter hybrid functional of Becke, B3LYP,[119,120] is one of the most popular functionals in current use.[121] PBE and TPSS have been used as the basis of hybrid functionals by including 25 % and 10 % of Hartree-Fock exchange, respectively, creating the functionals PBE0 (also known as PBE1)[122] and TPSSh.[123]

There is no straightforward way of determining the “best” density functional, as this can depend heavily on the system of interest. B3LYP is very successful in calculating structures of small organic molecules which are close those used to fit the B3LYP parameters, but is much less accurate for transition metal systems.[124] Cramer and Truhlar have reviewed several hundred DFT studies on transition metal systems in their 2009 review, and found no functional which clearly performs best in all systems.[111] Although DFT is commonly used for transition metal cluster systems, most of the validation studies, where calculations are compared to experimental data, use atomic metals, bulk metals or ligated metal atoms as the test systems, so the choice of functionals for clus-

ters remains challenging.

1.4.2 Applications of DFT to metal clusters

When comparing DFT calculations to the results of experiment, the first task is to find the lowest-energy isomers of a cluster. This involves optimising several different starting structures to find local minima on the potential energy landscape of the cluster. The ordering of these isomers can depend on the functional used.[125] Once the minima have been found, the second derivative of the energy can be calculated to find the normal mode frequencies of the cluster with which to compare experimental infrared spectra.[126,127] Calculated structures are also essential for comparison with diffraction patterns,[128] ion mobility experiments,[129] and photoelectron spectra.[83]

Calculating the energies of the possible spin states is also important, as some transition metal clusters have large magnetic moments. The superparamagnetism of rhodium clusters was first predicted by DFT[130] before it was confirmed experimentally.[131] Similarly, the magnetic moments of manganese clusters[132] have been explained by DFT calculations of ferrimagnetic ordering within the clusters.[133]

Excited electronic state calculations require a time-dependent version of density functional theory (TD-DFT), in order to interpret the results of electronic photoabsorption spectra. Kappes and coworkers used a combination of photodissociation and TD-DFT to investigate the 2D-3D transition in gold clusters.[134] Harb *et al.* calculated absorption spectra of bimetallic Ag_nNi_n clusters, and found that the predicted spectra were very similar, regardless of which GGA or hybrid functional was used.[135] Other parts of the potential energy landscape can be explored by using DFT with optimisation algorithms to calculate transition states (potential energy saddle points) as well as minima. For example, transition states along the pathway of the Rh_6^+ reaction with NO have been calculated to understand the reaction rates in FT-ICR experiments.[136]

Only a few applications have been mentioned here, but DFT is the most commonly used method for calculating the properties of transition metal clusters, and has been used in an enormous number of studies. Many of these were reviewed by Cramer and Truhlar,[111] and the literature is still growing.

1.5 Thesis overview

A wide variety of the techniques described above have been applied to transition metal clusters in this thesis. A laser vapourisation source, adapted from the original Smalley design, has been built and characterised. Rotationally resolved photoionisation spectroscopy has been applied to vanadium monoxide to investigate its electronic structure. Au_2 has also been studied with photoionisation, and velocity map imaging has also been used to characterise its dissociation pathways. Finally, infrared multiple-photon dissociation has been combined with density functional theory calculations to determine the structures of rhodium cluster complexes and to understand their reactivity.

Chapter 2 describes the design and initial characterisation of a new instrument for studying the structure of neutral and ionic metal clusters. The experiment involves a combination of spectroscopic and mass spectrometric techniques which can be applied to the electronic and vibrational structure of pure metal clusters and metal-containing clusters. A new laser vapourisation source has been developed which involves the addition of a cryogenically-cooled clustering channel for attaching weakly-bound argon atoms to the clusters. A linear time-of-flight spectrometer has been simulated, designed and built, allowing mass-selective spectroscopic measurements to be made.

The new instrument has been applied to record the REMPI spectrum of vanadium monoxide across the visible spectral region, as described in Chapter 3. The spectroscopic constants of several bands in the $C\,^4\Sigma^-$ and $B\,^4\Pi(4,0)$ states were recorded. Two new formally spin-forbidden transitions were observed, allowing the relative energies of the

quartet and doublet manifolds to be determined for the first time.

Chapter 4 presents the first work on velocity map imaging of the gold dimer, Au_2. Photodissociation is observed at 157 nm and at the two-photon level between 35500 and 37200 cm^{-1}. Imaging the excited state Au atom fragments aids the interpretation of the spectroscopy, and provides additional information on the photodissociation channels available to excited-state Au_2.

Chapter 5 describes the infrared multiple photon dissociation spectra recorded for argon-tagged rhodium clusters complexed with N_2O molecules, and the comparison of the spectra with those calculated using density functional theory. Infrared absorption also causes decomposition of the adsorbed N_2O on the surface of all Rh_n^+ clusters $4 \leq n \leq 8$ with the exception of $n = 5$. This reaction is studied in the absence of argon-tagging, and the reaction pathway is investigated with density functional theory calculations of the transition states.

Chapter 2

ToF instrument

2.1 Overview of the experiment

The new instrument consists of two differentially-pumped chambers: the source chamber, in which the metal clusters are produced by laser ablation and entrained in a molecular beam; and the detection chamber, in which the clusters are ionised and detected.

Figure 2.1 shows a schematic of the experiment. The 2nd harmonic of a ~ 10 ns pulsed Nd:YAG laser enters the chamber and ablates a rotating metal target. A pulse of an inert gas (helium, argon or a mixture of the two) picks up the ablated metal particles, carrying it down a variable 2–7 cm cluster channel where clustering occurs by multiple collisions in a relatively high pressure region. The gas pulse exits the source through a narrow orifice and expands into vacuum, which further cools the clusters.

The cluster beam is skimmed to provide differential pumping and passes into the detection chamber. In order to allow the detection of neutral clusters, an ionising laser pulse intersects the clusters in the beam when they reach the centre of the chamber. The electric field between the time-of-flight electrodes accelerates the cluster ions perpendicularly towards the microchannel plate (MCP) detector. The perpendicular extraction

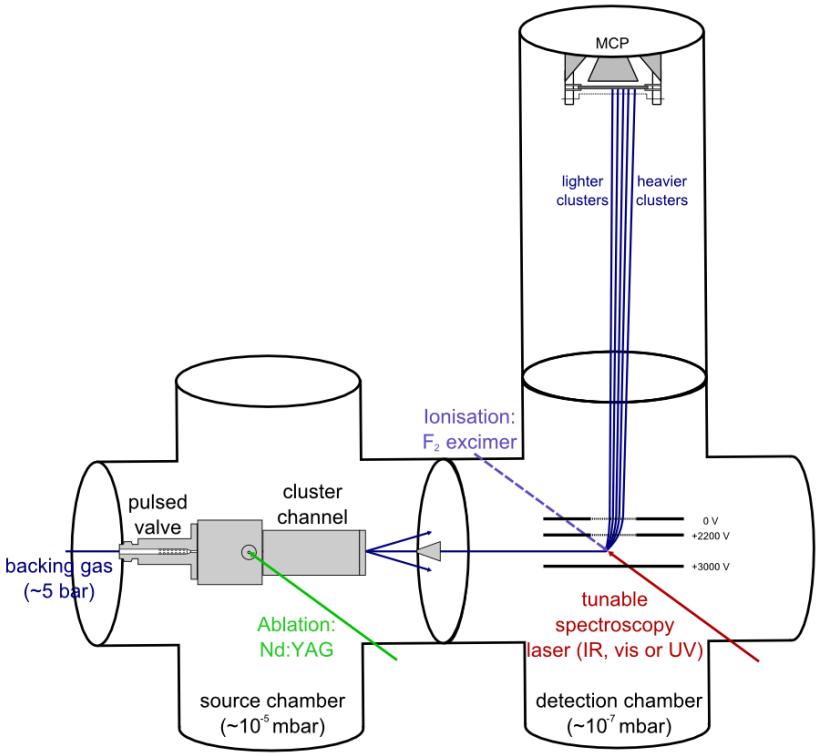


Figure 2.1: Schematic of chambers and laser beams.

has two advantages: firstly, the molecular beam does not hit the sensitive MCP; secondly, the distribution of velocities of ions in the molecular beam is narrower perpendicular to the beam, so the velocity spread does not substantially reduce the time-of-flight mass resolution.[137]

In the case of cationic clusters, no ionising pulse is required. Instead, the time-of-flight electrodes are held at zero potential until the ions arrive at the region beneath the extractor grid, at which point a voltage is applied to the electrodes to accelerate the ions towards the detector.

Figure 2.2 shows the assembled chambers with the surrounding optics. The instrument is designed as a flexible instrument for a range of experiments, such as cluster photodissociation and photoionisation. Pure metal clusters can be generated using laser ablation with helium as the carrier gas, but if another small molecule such as water is seeded in the helium then metal-containing clusters can be formed. Argon-tagged clus-

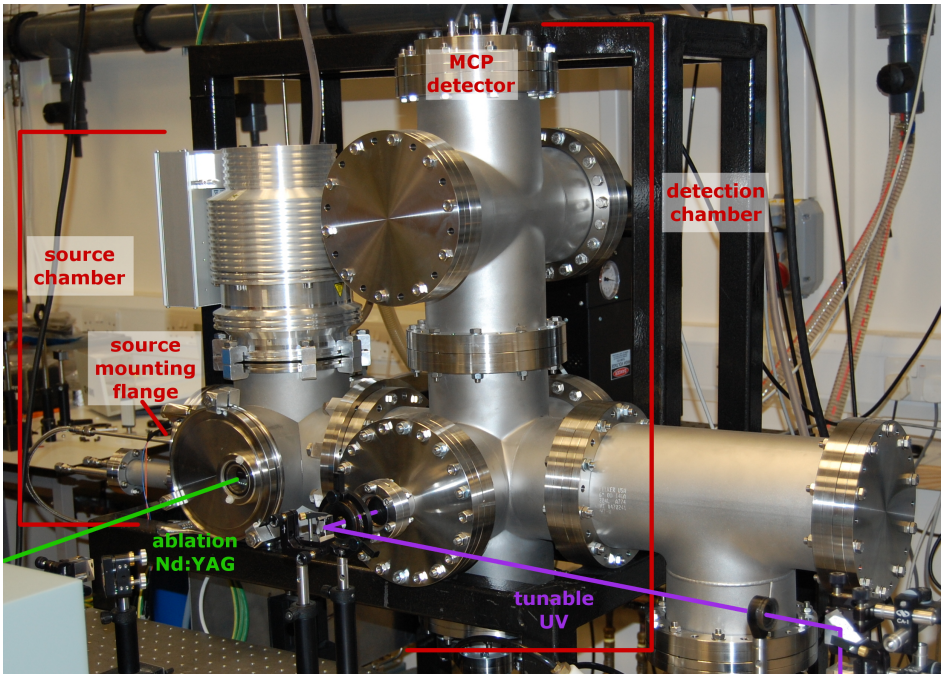


Figure 2.2: Overview of chambers and laser beams.

ters can be generated if argon is added to the backing gas, and the tagging efficiency is greatly improved if the source is cooled with liquid nitrogen.

The electronic structure of clusters can then be studied using the output of an optical parametric oscillator (operating in the visible spectral region) or a frequency-doubled dye laser (near-UV) to excite an electronic transition. This is followed by an ionising pulse of vacuum-ultra violet radiation from an F_2 excimer laser (157 nm), which is sufficient to ionise most transition metal clusters in a single-photon process. The OPO has medium resolution (5 cm^{-1}) but can be used to scan the whole visible region of the spectrum from 430 nm to the near infrared (4 μm). Where necessary, the structure of interesting regions of this spectrum can then be studied in more detail using the higher-resolution dye laser. The excited electronic states of transition metal clusters are very poorly characterised, and there is also interest in the onset of bulk properties such as conduction bands and surface plasmon resonances.

2.2 Design of a new metal cluster source

The cluster source was based on an earlier design used in the group for FT-ICR studies of metal clusters,[106] which in turn was a modified version of that used by Bondybey *et al*.[138] In these cluster sources, a rotating metal disc is ablated by a pulse of 532 nm radiation from the second harmonic of a Nd:YAG.[19] The laser pulse is synchronised with a short gas pulse (~ 40 μs) produced by a piezoelectric valve operating with backing pressures of 10 to 30 bar. The gas pulse passes through a narrow clustering channel before expanding into the source chamber.

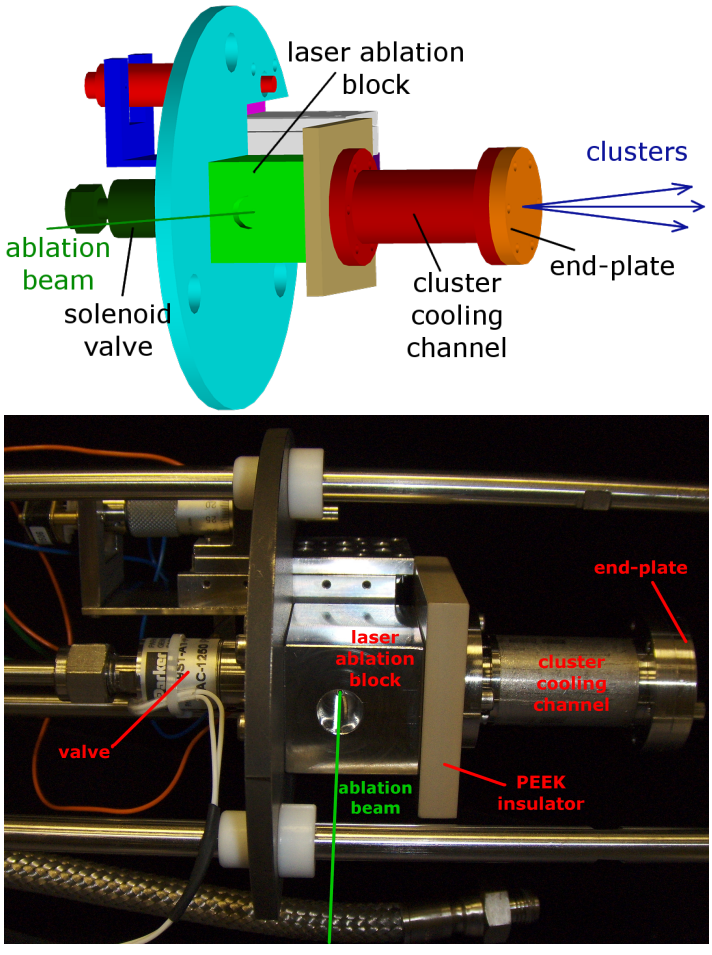


Figure 2.3: CAD drawing of source (above) and the assembled source (below).

Several modifications have been made in designing the source for the new metal cluster experiment, shown in Figure 2.3. Firstly, a solenoid valve is used in place of the

piezo valve. The solenoid valve consists of a coil of wire around a magnetic armature. This supports a teflon poppet which forms a seal between the gas in the valve and the vacuum chamber. When the valve is pulsed, the magnetic field produced by the coil pulls the armature and poppet into the body of the valve, opening the valve and releasing a pulse of gas. A spring then pushes the armature and poppet back into position at the end of the electrical pulse.

Although they have much longer pulse durations, necessitating the use of much larger (and more expensive) vacuum pumps, solenoid valves are more robust than piezo valves. Their major advantage, however, in spectroscopic experiments, is their superior shot-to-shot stability. The earlier designs described above produced clusters for FT-ICR experiments, in which the shot-to-shot stability was less critical, but even then extensive accumulation and averaging was required. For example, when studying reactions between Nb_n^+ clusters with small hydrocarbons, Bondybey allowed up to 40 pulses of niobium clusters to accumulate before introducing the reactant gas. In addition, these experiments followed the variation of species intensity with time, relative to their initial intensities. In contrast, the spectroscopy experiments described in this work require the ion signal and cluster distributions to be as uniform as possible as the ionisation laser is scanned.

Solenoid valves produce longer gas pulses on the order of 500 μs, since closing the valve depends on the relatively slow mechanical movement of a spring pushing the poppet, rather than the rapid deformation of a piezoelectric crystal. The gas released into the source chamber must be removed before the next gas pulse, typically 100 ms later, so lower backing pressures need to be used for the same pumping capacity. This may limit the size of the clusters which can be produced, but are sufficient for experiments on small clusters with $n \leq 20$.

A second significant modification is the inclusion of a cryogenically-cooled cluster

channel, which can produce clusters colder than those cooled by molecular beam expansion alone. The design is similar to that used by Fielicke *et al.* to study the far infrared absorptions of metal clusters.[18] If the source is not cooled, kT is similar to the dissociation energy of the weak argon-cluster van der Waals bond, $\sim 400\,\mathrm{cm}^{-1}$ corresponding to a temperature of $\sim 600\,\mathrm{K}$,[139,140] so very few argon-tagged clusters are produced. In the new source, the 2 mm-wide channel runs through a 50 mm-long cylinder of stainless steel containing an outer channel through which liquid nitrogen is flowed. This part is thermally insulated from the ablation block and valve by a block of polyetheretherketone (PEEK).

2.3 Cluster detection

2.3.1 Time-of-flight mass spectrometry

One method of detecting cluster ions is to use a time-of-flight (ToF) mass spectrometer, in which electric fields are used to separate clusters of different m/z. The simplest ToF configuration involves a constant electric field followed by a field-free drift region.[141] The accelerating field imparts the same kinetic energy to all ions, and so ions of the same charge but different mass leave the acceleration region with a velocity inversely proportional to $(m/z)^{1/2}$. The ions separate further in the field-free region, and so arrive at the detector in well-defined groups which are detected as individual peaks in the time-of-flight mass spectrum.

In any practical experiment, however, the ions are created in a finite volume rather than at a single point – for example in the intersection between the molecular beam and the ionising laser pulse. The range of initial positions becomes a spread in final kinetic energy and in the flight times, reducing the resolution of the mass spectrum. Wiley and McLaren introduced a second electric field into the mass spectrometer (see Figure 2.4)

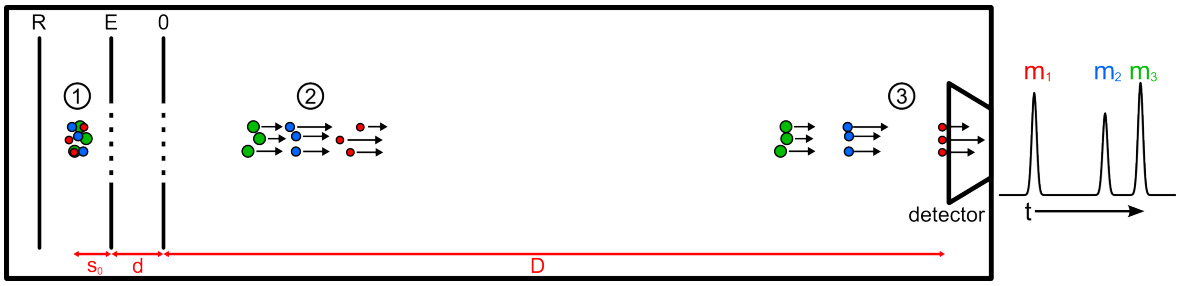


Figure 2.4: First-order focusing of three ions of different mass ($m_1 < m_2 < m_3$) created in a small volume between the repeller (R) and extractor (E) electrodes

to partially compensate for this effect.[41]

In Step 1, the ions are created with varying distances from the detector. When the ions leave the second electric field (Step 2), the ions which initially were furthest from the detector have spent more time in the electric field, and so exit with larger kinetic energies, and hence larger velocities. By the time the ions have reached the focus point where the detector is placed (Step 3), ions of different m/z have separated. For each mass, the ions which initially were furthest from the detector have caught up with those which were closer to the detector, producing a better-resolved peak in the mass spectrum.

Given fixed values for s_0 and d (defined in Figure 2.4), this focus position (distance D from the final electrode) is given by equation 2.1:

$$D = 2s_0 k_0^{\frac{3}{2}} \left(1 - \frac{1}{k_0 + k_0^{\frac{1}{2}}} \frac{d}{s_0} \right) \tag{2.1}$$

where

$$k_0 = \frac{s_0 E_s + d E_d}{s_0 E_s} \tag{2.2}$$

Equations 2.1 and 2.2 are independent of m/z, and so ions of any mass should, in principle, be space-focused at the detector.

If the electrode separations $2s_0$ and d, and flight tube length D are fixed, Equation

2.1 can be solved to find k_0. Equation 2.2 can then be rearranged to:

$$\frac{V_R}{V_E} = \frac{2}{k_0 - 1} + 1 \tag{2.3}$$

Equation 2.3 can then be used to calculate ratio of repeller to extractor voltages at which the ions are focused onto the detector.

2.3.2 Simulations of ion trajectories

Trial designs for the time-of-flight electrodes were tested using the ion optics simulation program SIMION 8.0.[142] The shapes and positions of electrodes can be drawn in SIMION, which then solves the Laplace equation to calculate the electrostatic potential at each point in space between the electrodes. It can then predict the trajectories of ions within these electric fields, given their initial positions and velocities.

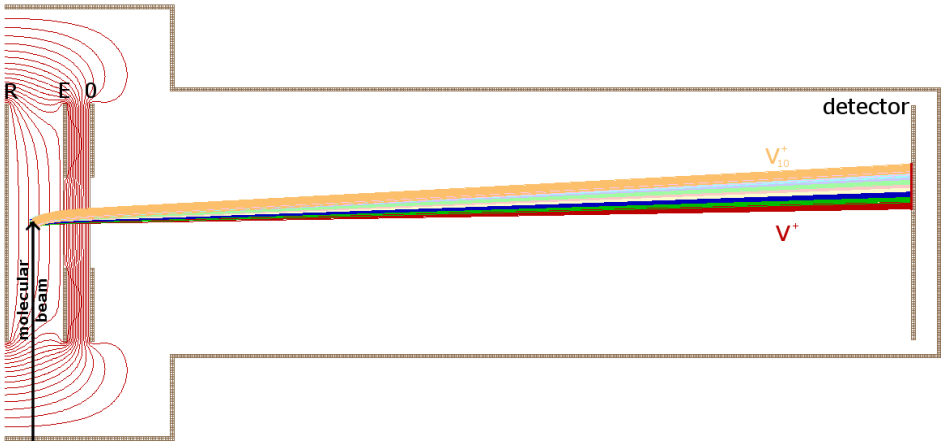


Figure 2.5: Simulated trajectories of vanadium cluster ions V_n^+ ($n = 1$–10) in the ToF spectrometer. Contours, separated by 150 V, mark lines of equal potential. $V_R = 3000$ V, and $V_E = 2208$ V, which meet the criterion for first-order focusing determined by Equation 2.1. Ions accelerated by the ToF electric fields still have an off-axis component to their velocity due to the molecular beam. Heavier ions have a longer time of flight than lighter ions, and so travel further off-axis before they reach the detector. This causes the spread in trajectories between ions of different masses.

The planned experimental time-of-flight spectrometer was modelled in SIMION as shown in Figures 2.5 and 2.6. The three electrodes (R, E and 0) are plates 2 mm thick and 130 mm in diameter. The repeller is a solid plate, but the centre of the extractor

and ground plates are 50 mm-diameter grids. Although some ions will collide with these grids, reducing the number which reach the detector, the grids are necessary to keep the fields between the electrodes as uniform as possible. Since the vacuum chamber is earthed, the walls of the vacuum chambers were included as an electrode fixed at 0 V.

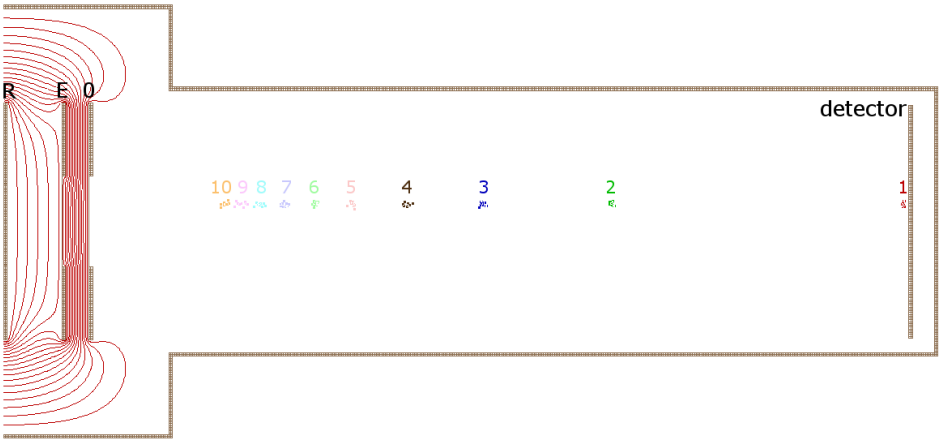


Figure 2.6: The positions of the V_n^+ ions at one instant during the simulation shown in Figure 2.5, with n labelled above each group of ions The temporal separation of the different clusters can be seen, as can the space-focussing of the V^+ ions closest to the detector.

The size of the chambers constrained the length of the flight tube, D. The repeller-extractor separation $2s_0$ and extractor-ground separation d were chosen to be 30 mm and 15 mm respectively. Given these distances, Equation 2.1 was solved to find $k_0 = 6.5803$, and hence from Equation 2.3, $V_R/V_E = 1.3584$.

The vanadium ions in the simulation were created in a spherical gaussian distribution with a standard deviation of 1 mm in space and 4 ns in time, to model the intersection between the molecular beam and ionisation laser pulse. All ions were simulated with an initial velocity of 1750 m s^{-1} perpendicular to the time-of-flight axis, corresponding to the molecular beam velocity.

Figure 2.7 shows a mass spectrum plotted from the results of the SIMION simulation described above. The good separation and resolution of these peaks (shown in more detail in Figure 2.8) indicates that the calculated electrode voltages are successful in space-focusing the ions at the simulated position of the detector.

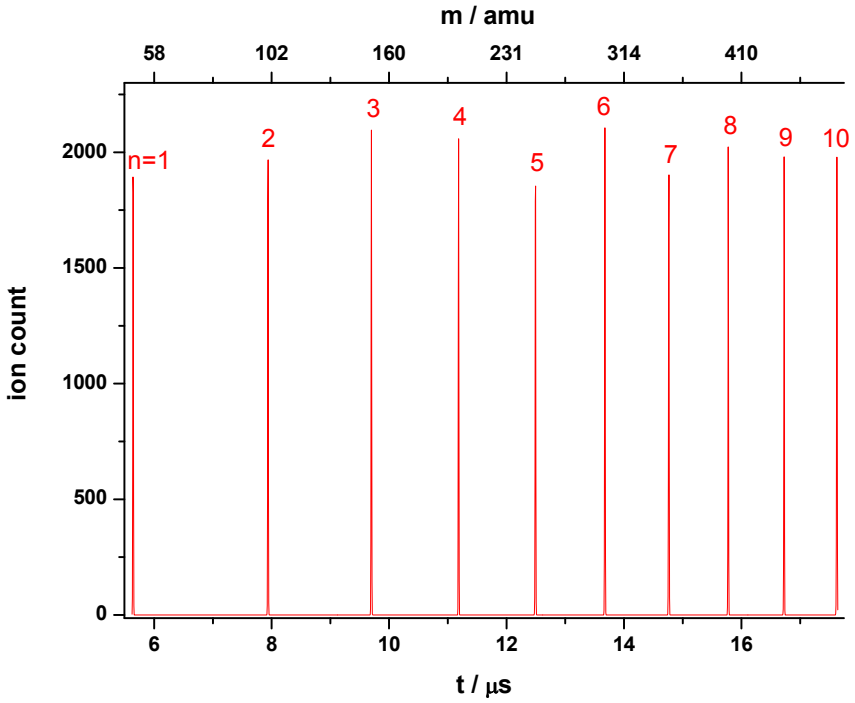


Figure 2.7: Simulated time-of-flight mass spectrum of vanadium cluster ions V_n^+.

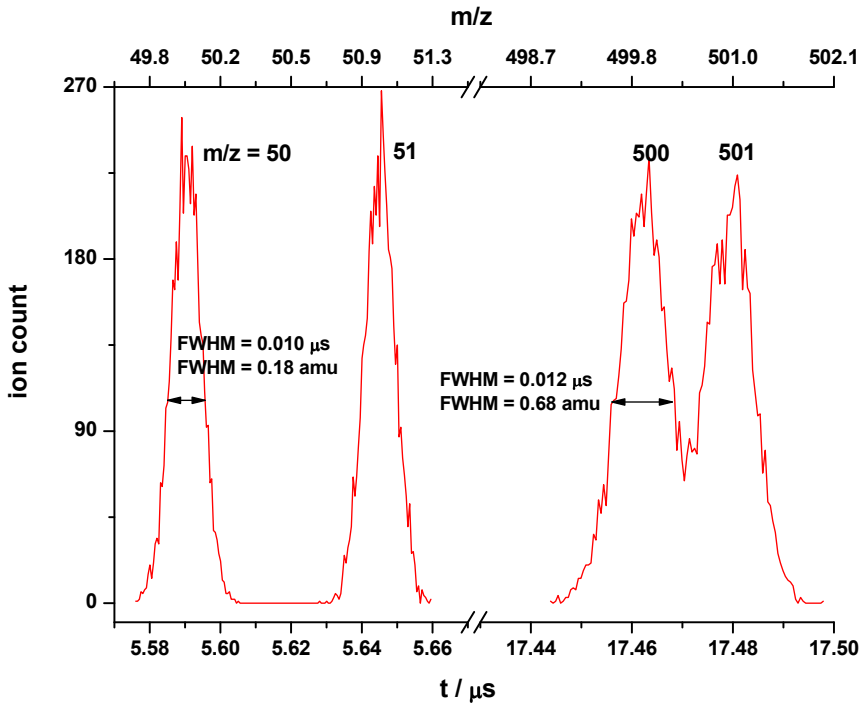


Figure 2.8: Simulated time-of-flight mass spectrum of ions of mass 50, 51, 500 and 501 amu. The largest contribution to the width of these peaks is the temporal distribution, rather than the spatial distribution, of the ions at the start of the simulation.

2.3.3 Electrode design

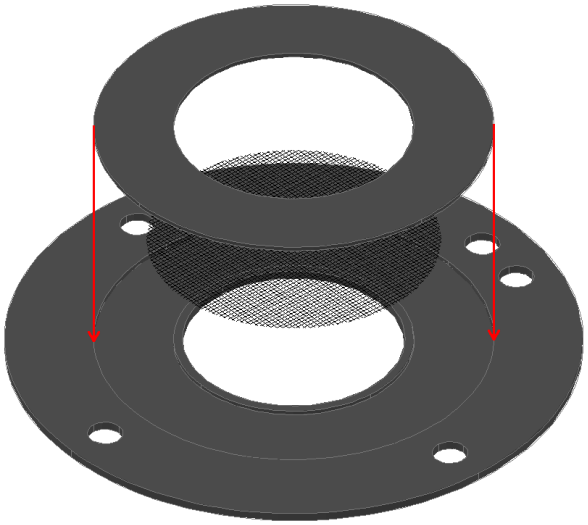


Figure 2.9: CAD drawing of the two parts of the extractor and ground plates. The electrodes were assembled as shown, with the mesh pinched between the two plates.

The electric fields between the time-of-flight electrodes should be as uniform as possible, which can be accomplished by using electrodes of larger diameter than the electrode separation. For this reason, the electrodes were chosen to be 130 mm in diameter. They were also designed to be as thin as possible (2 mm) to give a well-defined boundary between the three different electric fields. The SIMION simulations of the electric fields produced using this arrangement (see the contours in Figure 2.5) show that the fields are uniform in the region between the grids.

The mesh was fixed onto each electrode by pinching it between two stainless steel plates, as shown in Figure 2.9. The upper plate was pushed into the groove in the lower plate, stretching the mesh taut across the central gap, and then the two plates were spot-welded together.

The plates were then mounted onto four rods as shown in Figure 2.10. The electrodes are electrically insulated from each other and from the mounting rods by spacers made of polyetheretherketone (PEEK) which were fitted around the rods.

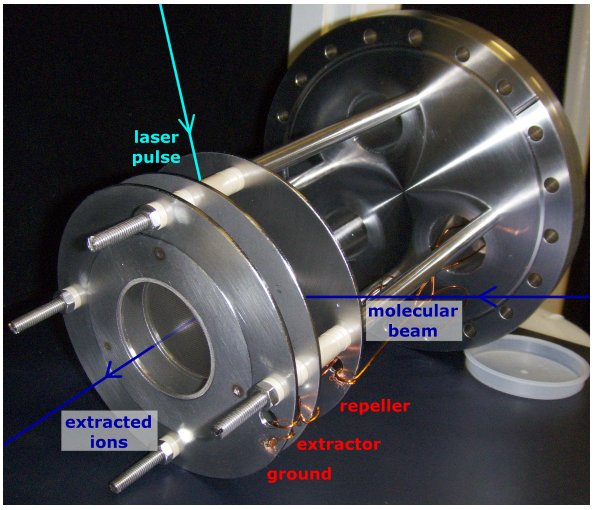


Figure 2.10: Assembled time-of-flight electrodes.

2.4 Instrument characterisation: REMPI spectrum of nitric oxide

2.4.1 Introduction

Nitric oxide, NO, is a well-characterised diatomic molecule with a strong electronic absorption in the ultra-violet region assigned as an $A\,^2\Sigma^+ - X\,^2\Pi$ transition. The rotational structure of this band is well known,[143] which makes NO a useful species to introduce into the new experiment in order to characterise the molecular beam's cooling efficiency, since the observed rotational line intensities are dependent on temperature.

We have studied this transition using Resonance Enhanced Multiphoton Ionisation (REMPI) spectroscopy. In REMPI, one or more photons are absorbed, exciting the molecule to a higher electronic state. A further photon then ionises the molecule, which is detected using time-of-flight mass spectrometry. The ionisation is enormously more efficient when the laser is tuned to a molecular transition than when it is tuned off-resonance, so the variation of ion signal with wavelength gives the spectrum of the ground–excited state transition.[144] In the variant used here, $(1+1)$ REMPI, one photon

excites the NO from the X to A state, and a further photon of the same colour ionises the NO.

The $A - X$ transition is a $^2\Sigma^+ - {}^2\Pi$ transition, and hence the selection rules are:

$$\begin{aligned} \Delta S &= 0 \\ \Delta\Lambda &= 0, \pm 1 \\ \Delta J &= 0, \pm 1 \end{aligned}$$

The spectrum is complicated by spin-orbit coupling in the ground state and spin-rotation coupling in the excited state. The ground $^2\Pi$ state has orbital angular momentum $\Lambda = 1$ and spin $S = 1/2$. Coupling between orbital and spin angular momentum splits each rotational level into two components with total angular momentum $\Omega = 1/2$ (labelled F_1) and 3/2 (labelled F_2),[145] separated by a spin-orbit coupling constant of $119.82\,\mathrm{cm}^{-1}$.[146]

The rotational levels of the excited $^2\Sigma^+$ state are split into two components by coupling with the electronic spin, giving levels with angular momentum $J = N \pm \frac{1}{2}$. The $J = N + \frac{1}{2}$ component is labelled F_1, and the $J = N - \frac{1}{2}$ component is labelled F_2.

P, Q and R - type transitions are allowed between all possible combinations of ground and excited state F_1 and F_2 levels, leading to twelve allowed branches:

$$\begin{array}{cccc} P_{11} & {}^{o}P_{12} & {}^{q}P_{21} & P_{22} \\ Q_{11} & {}^{p}Q_{12} & {}^{r}Q_{21} & Q_{22} \\ R_{11} & {}^{q}R_{12} & {}^{s}R_{21} & R_{22} \end{array}$$

where each branch is labelled as ${}^{\Delta N}\Delta J_{F_A F_X}$.

The spin-rotation splitting of the A state is too small to be resolved in our experi-

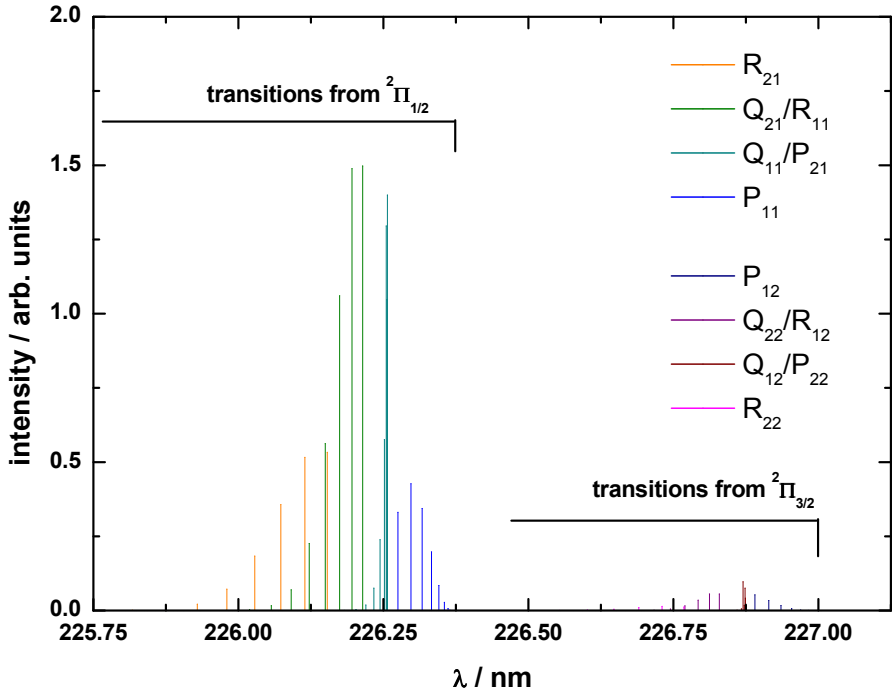


Figure 2.11: (1+1) REMPI spectrum of NO with rotational and electronic (spin-orbit) temperatures of 40 K and 100 K respectively, simulated using the spectral simulation program LIFBASE.[147]

ments, so only eight branches are observed, four of which are the sum of two overlapping branches at low J. A simulated spectrum of these branches is given in Figure 2.11.

The intensity of each transition is the product of a Boltzmann population factor with a branch-specific line strength factor (LSF) of the form:[145]

$$P_{11} \qquad \text{LSF} = \frac{(2J+1)^2 + (2J+1)X^{-1}(4J^2+4J+1-2Y)}{32J} \tag{2.4}$$

where X and Y are based on the spin-orbit coupling constant A_v and the rotational constant B_v for vibrational level v:

$$X = \left[4\left(J-\frac{1}{2}\right)\left(J+\frac{3}{2}\right)+(Y-2)^2\right]^{\frac{1}{2}}$$

$$\text{and} \quad Y = \frac{A_v}{B_v}$$

The equation for the rotational line intensity (Equation 2.5) can be rearranged to the form of a straight line (Equation 2.6).

$$\text{intensity} \propto \text{LSF}\exp\left(\frac{-B_0 J(J+1)}{k_B T_{rot}}\right) \tag{2.5}$$

$$\ln\left(\frac{\text{intensity}}{\text{LSF}}\right) = \frac{-1}{k_B T_{rot}} B_0 J(J+1) + \text{const.} \tag{2.6}$$

In this way, the rotational temperature can be extracted from the gradient of a plot of ln (intensity/LSF) against rotational energy.

2.4.2 Methods

The $(1+1)$ REMPI spectrum was recorded using gas mixtures of 1 to 2.5 % NO in either helium or argon. The gas mix was introduced into the backing line leading to the solenoid valve, which was pulsed at 10 Hz to produce a molecular beam. The molecular beam was crossed with the output of a dye laser (Sirah Cobra Stretch). The dye laser was pumped by the 355 nm output of a Nd:YAG laser operating at 10 Hz, and used Coumarin 450 dye. The output of this was then frequency-doubled in beta barium oxide (BBO) to produce near-UV light from 224 to 227 nm. When tuned to the position of an absorption line of the NO, one photon excites the NO to some rotational level in the $^2\Sigma^+$ state, and a second photon of the same wavelength excites the NO above its ionisation potential.

The resulting NO^+ is then accelerated towards the detector as described in Section 2.1.

The signal detected by the MCP was digitised by an oscilloscope (LeCroy Waverunner) and then sent to a computer. The mass spectrum peak due to NO^+ was integrated by a custom-built LabVIEW program as the dye laser wavelength was scanned. The REMPI spectra reported below show this integrated signal with respect to wavelength.

2.4.3 Results

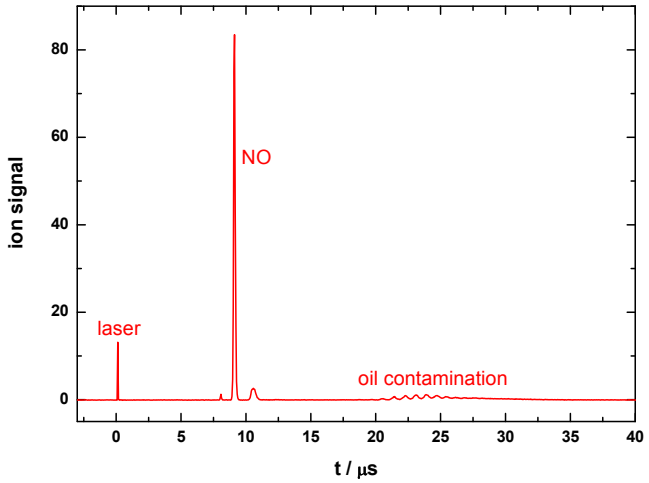


Figure 2.12: Time-of-flight mass spectrum of nitric oxide, with electrode voltages $V_R = 1000\,\text{V}$ and $V_E = 730\,\text{V}$, averaged over 200 shots. The peak at $t = 0$ is caused by scattered laser light reaching the MCP detector. The peaks between 20 and 27 μs are due to traces of oil. These peaks are separated by 14 mass units, consistent with the presence of a mixture of hydrocarbons of different chain lengths.

The peak due to singly ionised nitric oxide is clearly visible in the ToF mass spectrum trace recorded by the oscilloscope (Figure 2.12). Also present in the spectrum are a peak at $t = 0$ due to scattered light from the ionisation laser, and a series of higher mass peaks. The masses of these peaks were estimated from the time of flight of the NO^+ peak, based on the assumption that the ToF is proportional to $m^{1/2}$. The peaks are separated by 14 amu, the mass of a CH_2 unit, due to contamination from oil from a rotary pump whose oil was pulled back into the vacuum chambers during a power failure. The ability to identify these peaks indicates that the ToF mass spectrometer is working as intended.

The $(1 + 1)$ REMPI spectrum of NO was recorded in both helium and argon, in several

Table 2.1: Summary of molecular beam temperatures determined by Boltzmann plots of $(1+1)$ REMPI spectra of NO in various source configurations and backing gases

Source Configuration	Carrier Gas	T_{rot} / K
mounting plate only	He	49 ± 3
	Ar	20 ± 3
mounting plate, ablation block and end-plate	He	73 ± 3
	Ar	15 ± 2
as above, with cluster channel	He	300 ± 40

different source configurations. In each case, the temperature was extracted from a Boltzmann plot, summarised in Table 2.1.

The lowest temperatures recorded were those for a free expansion from the valve attached only to the mounting plate, with the other components of the source channel removed. Figure 2.13 shows the spectrum recorded using this configuration using helium as the carrier gas. Using the intensities of the R_{11} branch, the temperature of the NO can be calculated from the corresponding Boltzmann plot.

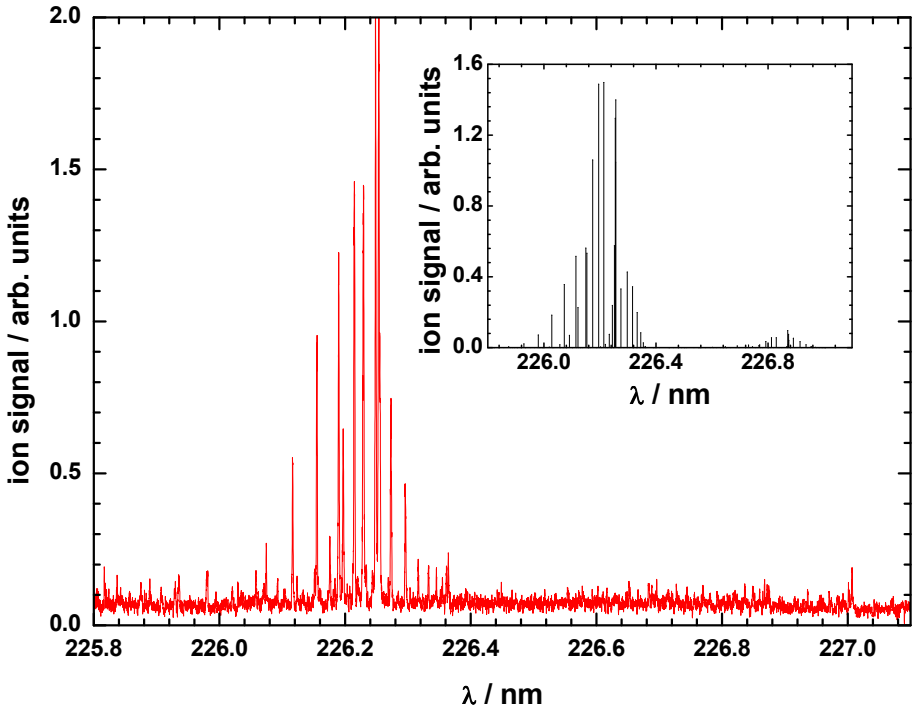


Figure 2.13: $(1+1)$ REMPI spectrum of NO in Ar, with ablation block and cluster channel removed. The inset shows a simulation of the spectrum with a rotational and electronic (spin-orbit) temperature of 20 K and 70 K, respectively.

The Boltzmann plot in Figure 2.14 is fitted to the eight identifiable R_{11} lines of NO in a pure helium carrier gas, identifying a temperature of 49 ± 3 K. The linear fit is not ideal, however, suggesting that the NO has not been uniformly cooled to this temperature. Separate linear fits to the lower J and higher J data points give temperatures of 43 K and 64 K respectively. The higher J levels have a higher apparent temperature because the energy spacing of the rotational levels increases with J, and collisions with He atoms are less efficient at transferring larger amounts of energy from the NO to the He.

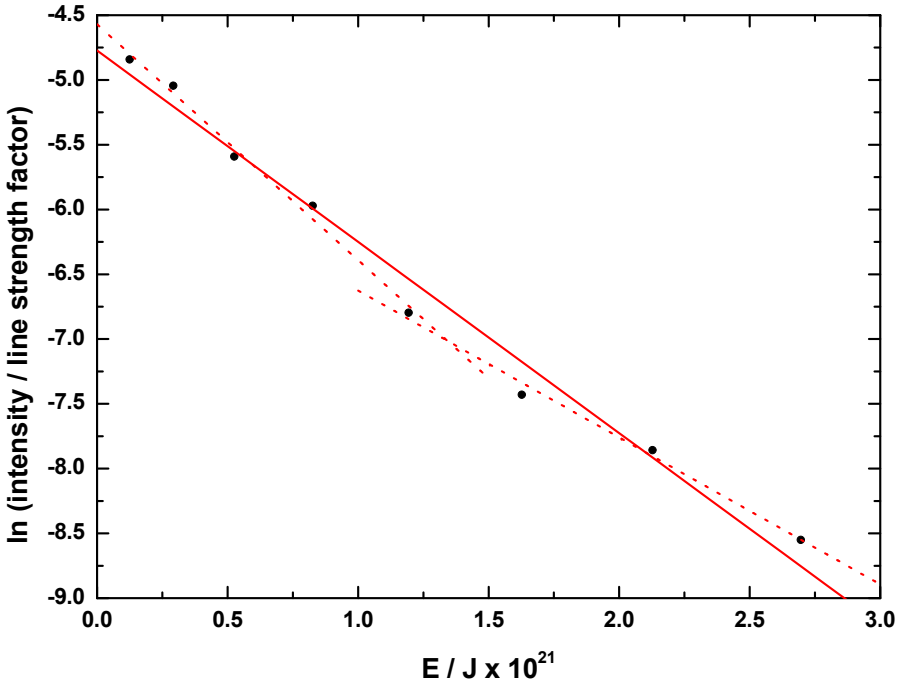


Figure 2.14: A typical Boltzmann plot: the R_{11} branch of the NO REMPI spectrum recorded in helium, from which a rotational temperature of 49 ± 3 K can be extracted (solid line). The dashed lines indicate fits to the lower and higher J lines, indicating that the latter are less efficiently cooled.

When the laser ablation block and end-plate were attached to the mounting plate, the temperature of the NO in the helium beam rose to 73 K because the expansion efficiency is reduced: when the valve is opened the pressure inside the clustering channel rises, but cannot rise to the pressure of the gas in the backing line since the other end of the channel is open to vacuum. A lower pressure in the source channel leads to a lower pressure within the molecular beam, so there are fewer collisions between NO molecules and

the carrier gas and hence the NO enters the detection chamber with a higher rotational temperature.

When the clustering channel was added, the volume between the valve and end-plate was increased further, leading to a hotter expansion. The NO REMPI spectra recorded with this source configuration showed no cooling from room temperature.

2.5 Neutral and cationic vanadium oxide clusters

In the first experiments employing the new metal cluster source, the surface of a rotating vanadium target was vapourised by the 2nd harmonic of a Nd:YAG laser (Litron Nano operating at 10 Hz, 8 ns pulse, 5 to 10 mJ). A 500 μs pulse of helium from the solenoid valve (backing pressure 3 bar) carried the resulting vanadium atoms and ions along the channel of the laser ablation block, where the vanadium aggregated into clusters. The delay between the solenoid valve opening and the ablation laser pulse could be adjusted to produce the strongest ion signal. Vanadium oxide clusters were also formed because of the trace of oxygen in the helium and the ablation of surface oxide from the vanadium disc. The helium then expanded into vacuum, entraining the vanadium oxide clusters, and the beam was skimmed before reaching the TOF mass spectrometer.

2.5.1 Cationic $V_nO_m^+$ clusters

To detect the cationic $V_nO_m^+$ clusters, the time of flight electrodes were initially held at zero potential. The repeller and extractor were pulsed to the correct voltages for first-order-focussing (see Section 2.3.1) to accelerate the ions out of the beam, and then returned to zero again before the arrival of the next gas pulse.

A typical TOF mass spectrum of these clusters is given in Figure 2.15. The time of flight of the nitric oxide as measured in Section 2.4 was used as a rough calibration for

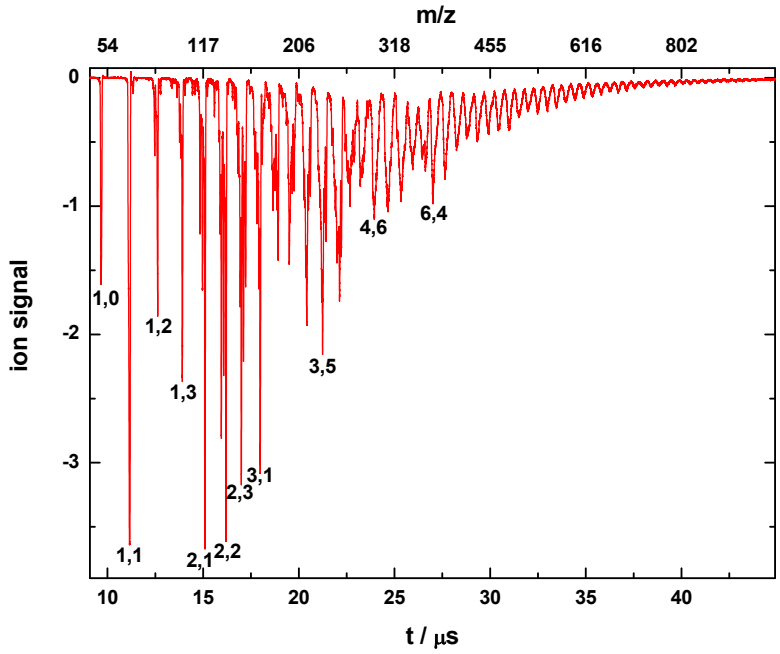


Figure 2.15: Typical time-of-flight mass spectrum of the cationic $V_nO_m^+$ ions; peaks are labelled as (n,m).

this mass spectrum, and allowed the identification of the intense V^+ and VO^+ peaks. These were then used for a more accurate calibration and the assignment of the larger clusters. Clusters with m/z of up to around 1000 were detected.

Although weak signals due to bare V_n^+ clusters could be identified, these mass spectra are dominated by the oxide clusters with some H_2O complexes also present. The helium used as a carrier gas was very high purity (99.9999 %) so the most likely sources of oxygen are not from the helium cylinder but rather the oxide outer coating of the vanadium metal target or impurities on the walls of the steel tubing connected to the solenoid valve. This oxygen and water was later cleaned from the helium by heating the backing line, but we have taken advantage of it to perform spectroscopic studies of vanadium oxides.

2.5.2 Neutral V_nO_m clusters

The neutral vanadium oxide clusters were ionised at 225 nm by the second harmonic of a dye laser with frequency doubling (details given in Section 2.4.2). The ionisation potential of vanadium is 6.7462 eV, so this mass spectrum must be due to multi-photon ionisation. Constant potentials on TOF electrodes accelerated the cluster ions towards the detector, and also repelled cations already present in the molecular beam.

The oxide peaks still dominate the mass spectrum of the neutral clusters (Figure 2.16), but more bare vanadium clusters can be identified than in the mass spectrum of the cations. This may be a reflection of the ionisation energies: some small vanadium clusters can be ionised with a single photon at 255 nm,[148] whereas higher photon energies are required to ionise the oxides.[149]

The TOFs of the ionised neutral V_nO_m clusters are shorter than those measured for the cations because higher DC potentials could be applied to the TOF electrodes than

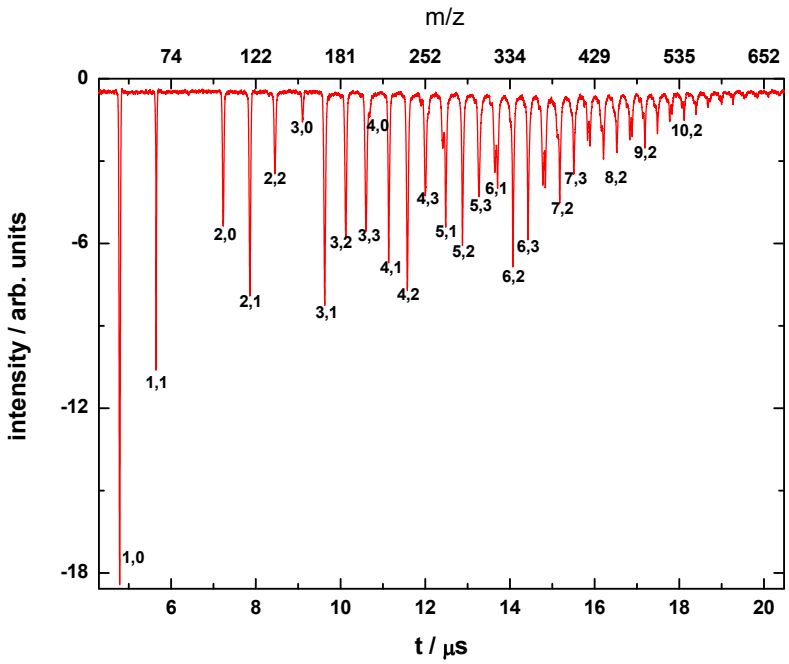


Figure 2.16: Typical time-of-flight mass spectrum of the neutral V_nO_m clusters ionised non-resonantly by a 200 μJ laser pulse at 225 nm; peaks are labelled as (n,m).

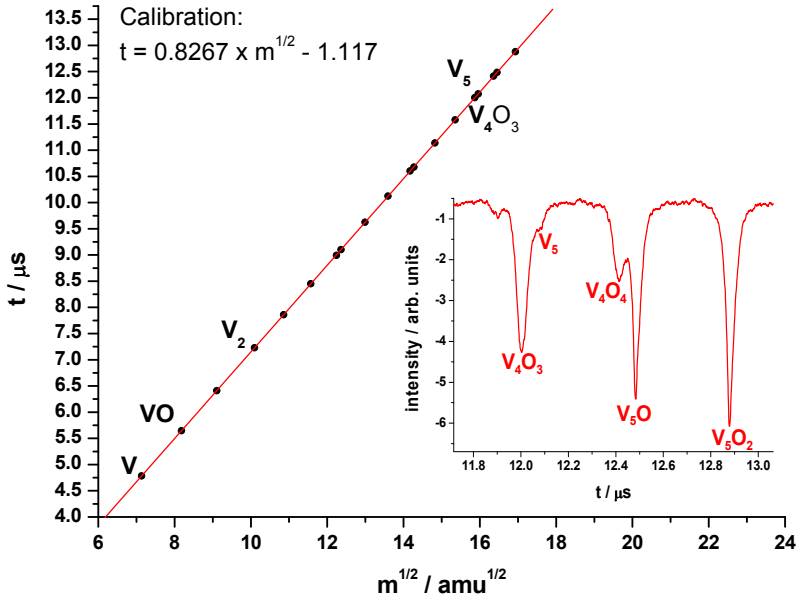


Figure 2.17: Calibration of time-of-flight axis based on the assumption that the time of flight is directly proportional to the square root of *m/z*. The linear fit has an R^2 value of 1.

when pulsed as in cation detection. Figure 2.17 illustrates the accuracy of calibrating the mass of the clusters with their times of flight.

2.5.3 Cluster formation and mass slippage

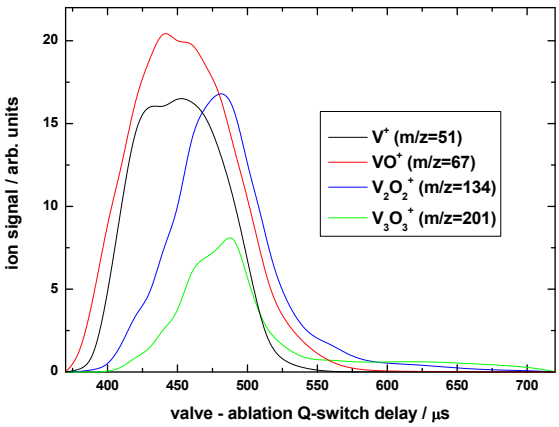


Figure 2.18: The fraction of the gas pulse comprised of larger clusters increases as the ablation laser is delayed with respect to the valve firing.

The distribution of clusters produced and detected could be tuned by adjusting the relative timing of events. By delaying the ablation pulse with respect to the gas pulse from the solenoid valve, more of the heavier clusters were produced (Figure 2.18). After

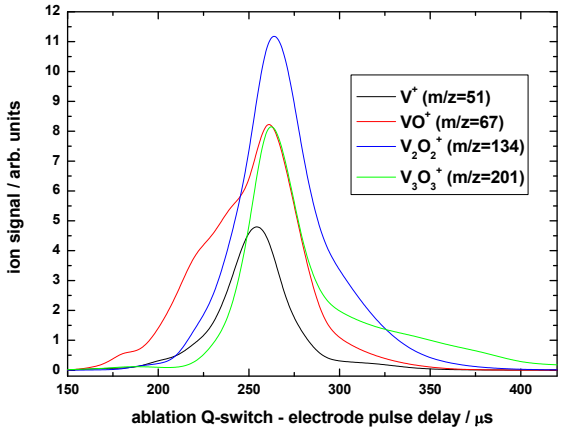


Figure 2.19: The fraction of the gas pulse comprised of larger clusters increases as the electrode pulse is delayed with respect to the ablation laser, due to mass slippage in the molecular beam.

the valve has opened, allowing helium into the source channel, the pressure builds up from the base pressure. If the target is ablated early in the gas pulse, the vanadium monomer and low-mass clusters are formed. If the ablation laser is delayed until the pressure is higher, there will be more collisions between metal clusters and the helium which will cool them and allow larger clusters to form.

Collisions between the clusters and the helium carrier gas cool the clusters during the expansion into vacuum. Heavier clusters may not undergo enough collisions to accelerate them to the velocity of the helium beam, and so they would be expected to arrive at the TOF electrodes after the lighter clusters. This effect can be seen in Figure 2.19, in which the ion signal is measured at several different delays between ablation pulse and electrode voltage pulse.

2.6 Calibration: REMPI spectrum of atomic V

There are many excited states of atomic V accessible by one-photon transitions in the near-UV,[150] within the range of the frequency-doubled output of the dye laser. The (1+1) REMPI spectrum of these levels was recorded to confirm the correct identification of the V monomer peak in the mass spectrum, and to calibrate the dye laser.

Atomic vanadium has a ^4F ground state, which is split by spin-orbit coupling into four

components with $J = 3/2$ to $9/2$. The selection rules for one-photon absorption in atoms are:[151]

$$\begin{aligned} \Delta S &= 0 \\ \Delta L &= 0, \pm 1 \\ \Delta J &= 0, \pm 1 \end{aligned}$$

The $(1 + 1)$ REMPI spectrum of V was recorded between 220 and 232 nm using the method described for NO in Section 2.4.2. Each data point is an average of ten laser shots. Almost all of the lines were assignable by reference to the NIST atomic database[150] to transitions allowed by the selection rules above, and some of these assignments are given together with the full recorded spectrum in Figure 2.20.

2.7 Conclusions

A time-of-flight mass spectrometry instrument has been designed, built and characterised. A laser vapourisation cluster source was constructed, and a home-built linear time-of-flight mass spectrometer was built, based on computer simulations of its space-focusing properties.

The known REMPI spectroscopy of nitric oxide was used as a test system for the new instrument. The rotationally-resolved spectrum of the $A\,^2\Sigma - X\,^2\Pi$ transition were used to characterise the molecular beam temperature with several different cluster source configurations. The cluster source was tested by producing neutral and cationic vanadium oxide clusters $V_nO_m^{0/+}$ of sizes up to around $n = 10$.

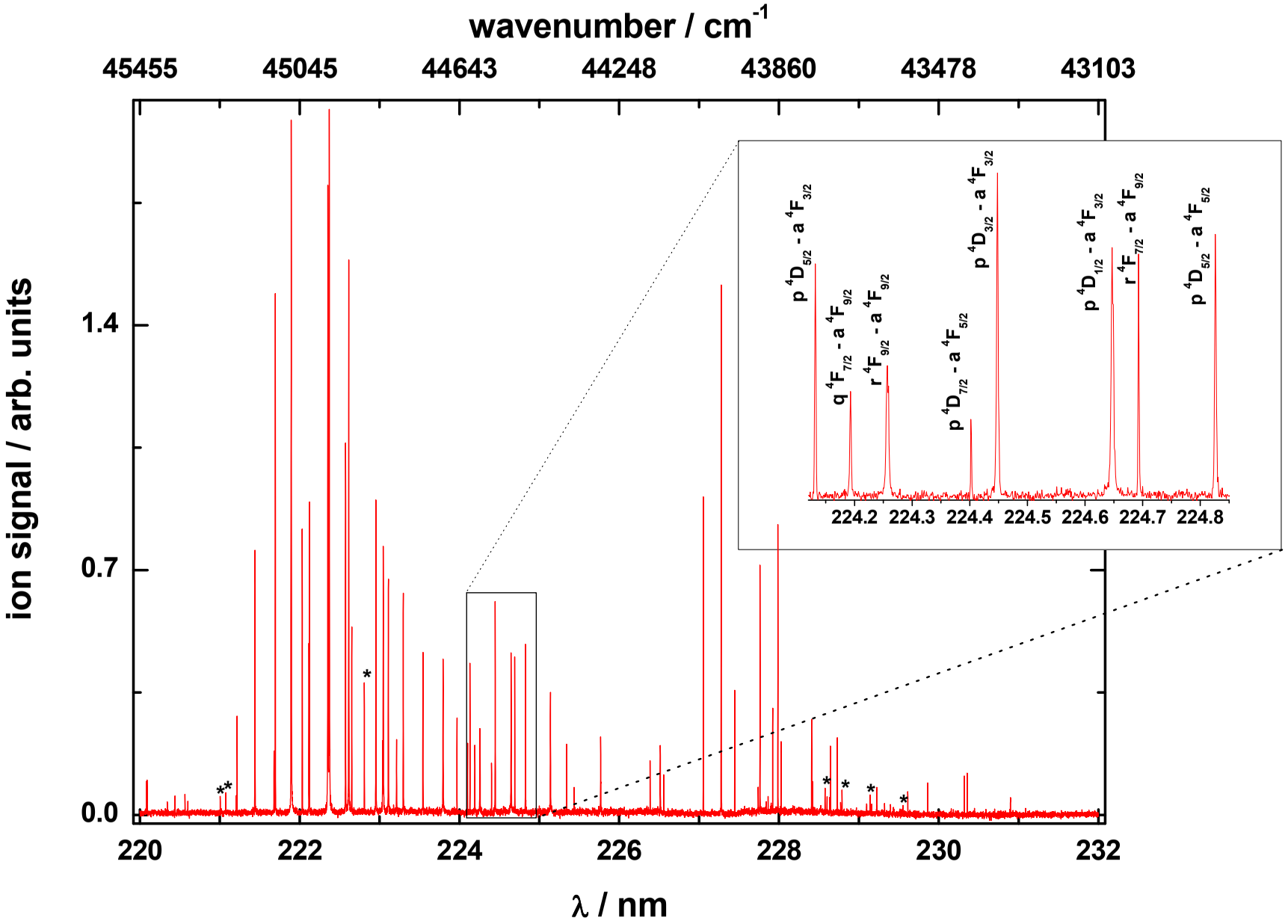


Figure 2.20: (1 + 1) Resonance-Enhanced Multiphoton Ionisation Spectrum of the vanadium atoms produced by the cluster source, and used for wavelength calibration. The inset shows the assignment of some of these lines. Asterisks mark lines for which no assignment could be made.

The VO spectroscopy experiments described in Chapter 3 were performed using this instrument, and the cluster source was used in the VMI of Au_2 (Chapter 4).

Chapter 3

REMPI Spectrum of Vanadium Monoxide (VO) †

3.1 Introduction

In the distribution of vanadium oxide clusters used to characterise the new Time of Flight instrument (Section 2.5), one of the most abundant species was the vanadium oxide diatomic, VO. The excited states of this molecule have been extensively studied, with much of the research motivated by its astrophysical relevance: VO is present in the atmosphere of M-type stars, and its absorption and emission lines are used to characterise their temperatures.[153]

A summary of the known electronic states of VO is given in Figure 3.1. Although the ground state of VO was first identified as $^4\Sigma^-$ by ESR,[154] much of the subsequent work has employed emission spectroscopy to investigate the excited states. Merer *et al.* identified five further quartet states: $A\,^4\Pi$,[155] $B\,^4\Pi$,[156] $C\,^4\Sigma^-$,[157] $D\,^4\Delta$,[158] and $A'\,^4\Phi$.[158] The A, B and C states, which are all accessible from the ground state by single-photon

† Some of the results in this chapter have been published as Hopkins *et al.*, *The electronic spectrum of VO across the visible: New bands and new insight*.[152]

excitation, have also been studied using REMPI, to determine their lifetimes,[159] and by pulsed field ionisation.[160]

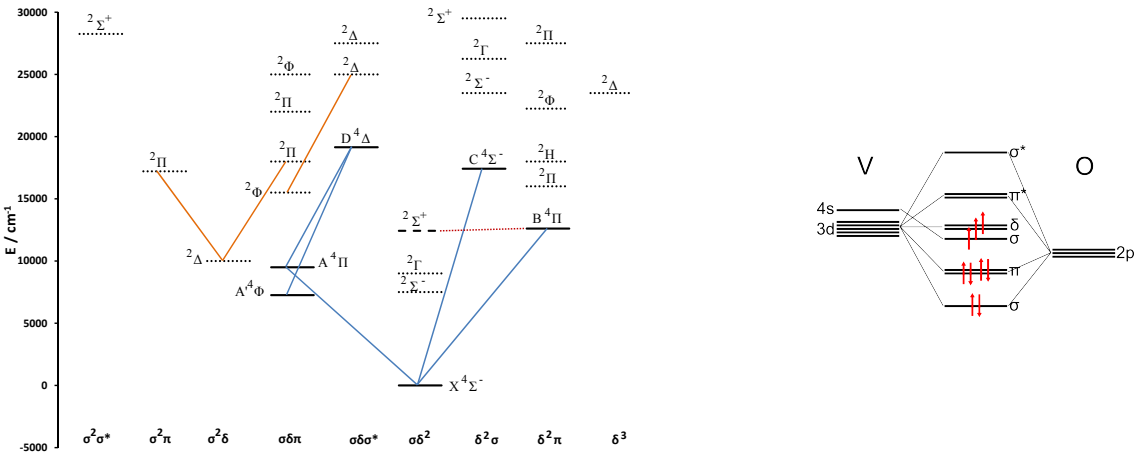


Figure 3.1: Left: Known electronic states of vanadium monoxide, from work by Merer *et al.*[158] Solid lines indicate states whose energies are known, relative to the ground state; dashed lines indicate states which are known through rotational analysis of perturbations; dotted lines indicate states which have been calculated but not observed experimentally, and those whose energies are not known relative the to the ground state. Lines connecting states indicate experimentally observed transitions. Right: molecular orbital scheme for the ground state $\sigma\delta^2$ configuration of the $X\,^4\Sigma^-$ state, adapted from work by Kasai.[154]

Several doublet states have also been reported, including two $^2\Pi$ states.[161,162] Because transitions between the doublet and quartet states are spin-forbidden, the energies of these states relative to the ground state could not be determined by emission spectroscopy. The relative energies were approximately determined by photoelectron spectroscopy, in which one peak was assigned as the previously reported $^2\Phi$ state, on the basis of its predicted position.[163] The uncertainty in this measurement, however, was large, around 100 cm^{-1}. The relative energy has been determined more accurately for only one doublet state, the $^2\Sigma^+$, as it was observed as a perturbation of the $B\,^4\Pi$ state. Without any reported transitions between this $^2\Sigma^+$ and any other doublet states, the relative energies of the doublet and quartet manifolds remained uncertain.

Despite having zero orbital angular momentum, the $^4\Sigma^-$ ground state has a complicated energy level structure because of spin-rotation and spin-spin splittings and hyper-

fine coupling between the electronic and nuclear spins ($I = 7/2$ for ^{51}V). Perturbations between energetically close states and even between spin-rotation levels complicate the spectra yet further.[157]

The spectra reported here allowed the determination of rotational constants of several $C\,^4\Sigma^-$ vibrational levels and the $v = 4$ level of the $B\,^4\Pi$ state. Two $^2\Pi - X\,^4\Sigma^-$ vibrational progressions were also identified, connecting the VO doublet and quartet manifolds for the first time. These results have previously been published,[152] but some of the $^2\Pi$ rotational parameters have been improved upon in this work because of an update to the spectral simulation software PGOPHER which made it possible to simulate the spin-forbidden transitions.

3.2 Methods

Preliminary REMPI experiments employed an optical parametric oscillator for photoionisation (Panther Ex OPO, pumped by a Nd:YAG 2nd harmonic, 8 ns pulse, 5 cm^{-1} resolution). A full scan of the spectrum between 430 and 650 nm was recorded.

These one-colour REMPI experiments were subsequently repeated at higher resolution using the fundamental output of a dye laser (Sirah Cobra Stretch, pumped by the second harmonic of a Continuum Surelite II Nd:YAG, 8 ns pulse, 0.15 cm^{-1} resolution).

Since the ionisation potential is 58383 cm^{-1},[160] the number of photons required to ionise VO is three or four, depending on which region of the visible spectrum the laser is tuned to. To improve the ionisation efficiency, two-colour, two-photon ($1 + 1'$) REMPI scans were also recorded. For these scans, the OPO and dye laser beams were spatially and temporally overlapped with the molecular beam. Medium resolution scans were obtained by photo-exciting with the OPO between 430 to 650 nm, and ionising the VO with a second photon from the dye laser, whose output was frequency-doubled and fixed at 230 nm. Higher resolution scans were recorded using the reverse process: scanning

the fundamental of the dye laser and using the second harmonic of the OPO output, also at 230 nm, for ionisation.

The REMPI spectrum of the V atom was used to calibrate the VO spectra, as shown in Section 2.6. The atomic spectrum was recorded simultaneously and assigned using the NIST atomic database.[150] Rotational structure of the high-resolution spectra was simulated using the program PGOPHER.[164]

3.3 Results and discussion

3.3.1 Broadband spectra

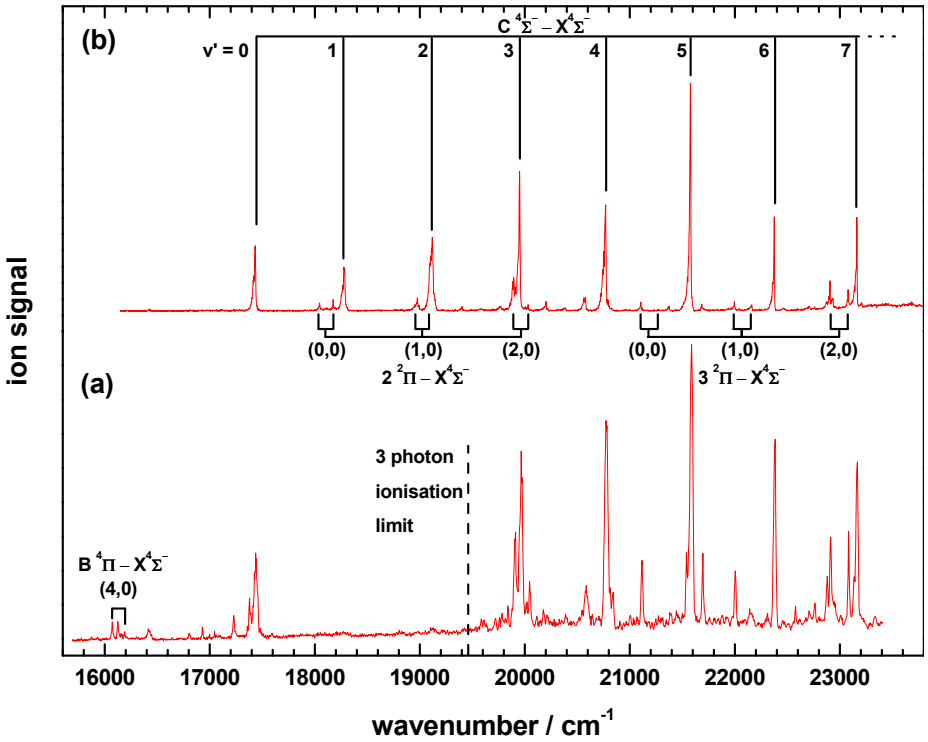


Figure 3.2: REMPI spectrum of the vanadium monoxide diatomic, detected using multiphoton ionisation, with the proposed assignment of the vibrational bands (see text). (a) One colour ($1 + n$) experiment using only the OPO. (b) Two colour ($1 + 1'$) experiment: photoexcitation by OPO, followed by photoionisation by dye laser tuned to 230 nm.

The low-resolution one-colour spectrum recorded using the OPO (Figure 3.2(a)) re-

veals six strong bands separated by approximately 800 cm^{-1}. These are assigned as the (0,0) and (3,0) to (7,0) of the known vibrational progression of the $C\,^4\Sigma^- - X\,^4\Sigma^-$ transition.[165] The limit for three photon ionisation lies between the (2,0) and (3,0) bands, and so the two lowest-energy overtone bands, the (1,0) and (2,0), are missing because of the inefficiency of the four photon process required to ionise the VO at these wavenumbers. These two bands are observed upon introducing a second laser at 230 nm for photoionisation (Figure 3.2(b)). The $C - X$ assignment is supported by the rotational analysis of these bands (Section 3.3.2).

Further evidence that the strong bands in the one colour spectrum are $(1 + n)$ REMPI transitions (where $n = 2$, 3) comes from the dependence of the ion signal on laser power. The simultaneous absorption of n photons should increase in probability as a function of laser power raised to the power n. For example, the intensity of a (2+1) REMPI transition is quadratic in laser power. In this case, the intensity of the spectral peak centred at 21578 cm^{-1} is linear with laser pulse energy (Figure 3.3), supporting our assignment of $(1 + 2)$ REMPI.

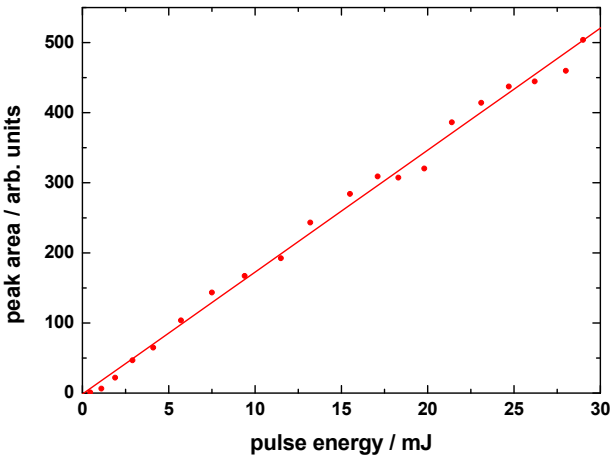


Figure 3.3: The area under the spectral peak centred at 21578 cm^{-1} increases linearly with the pulse energy of the ionisation beam from the OPO, supporting the assignment of this as a $(1 + n)$ REMPI peak.

Several of the lower-wavenumber peaks are also assignable to previously reported vibronic bands in the quartet manifold: the four spin-orbit components of $B\,^4\Pi - X\,^4\Sigma^-$ (4,0)

are observed between 16000 and 16300 cm^{-1}. All four components, $\Omega = 5/2, 3/2, 1/2, -1/2$, were also recorded with rotational resolution.

Two additional progressions were observed which could not be assigned to any of the previously reported transitions. Each band has two spin-orbit components and this, together with rotational analysis, allows us to assign them as $^2\Pi - {}^4\Sigma^-$ bands.

3.3.2 $C\,^4\Sigma^- - X\,^4\Sigma^-$ transition

By far the most intense progression in the broadband spectra is that assignable to the $C - X$ absorption band. Many of these bands have been observed previously in low-resolution, providing vibrational constants for both states[165] that are very close to those measured here. Only the origin band has been recorded in high-resolution by emission spectroscopy,[157,166] but this is also in agreement with the REMPI spectra discussed below. The ground state rotational and hyperfine constants are extremely well-characterised by these emission studies, and also by the more recent microwave absorption study by Flory and Ziurys.[167]

Hund's case (b) is a good approximation to both of these $^4\Sigma^-$ states. As there is no orbital angular momentum, the electronic spin $\boldsymbol{S}$ couples to the molecular rotation $\boldsymbol{N}$. This lifts the degeneracy of each rotational level, splitting it into four components with total angular momentum quantum number J given by:

$$J = \left(N + \frac{3}{2}\right), \left(N + \frac{1}{2}\right), \left(N - \frac{1}{2}\right), \left(N - \frac{3}{2}\right) \tag{3.1}$$

In both cases, spin-spin coupling splits these levels further. This is especially significant in the X state, as shown in Figure 3.4.

Selection rules for the $C\,^4\Sigma^- - X\,^4\Sigma^-$ transition are given in Table 3.1. These result in 24 different branches between the different components of the upper and lower states, of N-, P-, R- and T-character with $\Delta N = -3, -1, +1, +3$, respectively. These transitions

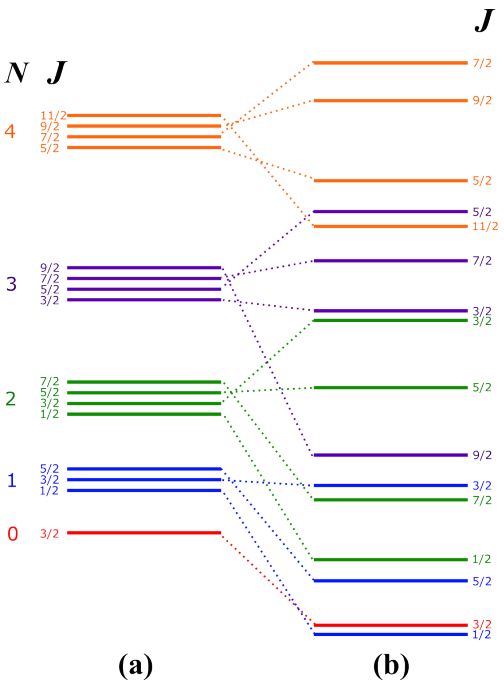


Figure 3.4: Rotational levels of the $X\,^4\Sigma^-$ VO ground state. (a) Spin-rotation coupling lifts the degeneracy of the N levels. (b) These are then split further by strong spin-spin coupling.

Table 3.1: Selection rules for the $C\,^4\Sigma^- - X\,^4\Sigma^-$ transition. A rotational level J is labelled e if its parity (symmetry upon geometric inversion of $\psi_{\text{elec}}\psi_{\text{nuc}}$) is equal to $+(-1)^{J-\frac{1}{2}}$, or labelled f if the parity is equal to $-(-1)^{J-\frac{1}{2}}$.

$$\Delta S = 0$$
$$\Delta J = 0, \pm 1$$
$$e \leftrightarrow e, f \leftrightarrow f \quad \text{if } \Delta J = \pm 1$$
$$e \leftrightarrow e \quad \text{if } \Delta J = 0$$

were simulated in PGOPHER.[164] Ground state parameters were fixed to those previously determined by microwave spectroscopy, as these resolved even the hyperfine structure. Two parameters of the excited C state were fixed to those determined in emission spectroscopy of the $(0, 0)$ band: D and γ_D, the centrifugal distortion of the rotational constant and spin-rotation coupling constant, respectively.[157] Four other parameters were varied: the band origin T_0, rotational constant B, spin-spin coupling parameter λ and spin-rotation constant γ.

Figures 3.5 and 3.6 show the $C - X\,(1 + 1')$ REMPI spectra recorded with rotational resolution. Below each band is the Gaussian-broadened simulation. In each case, the spectrum is dominated by the overlapped band heads of the nine R-form branches. These extend to lower wavenumber, overlapping with the P- and N-form branches. A weaker group of peaks to higher wavenumber are due to the three T-form branches, whose intensities fall below the noise level before reaching the band heads. The (4,0) band is complicated by the overlap of another band, assigned as the $2\,^2\Pi_{1/2} - X\,^4\Sigma^-(3, 0)$, discussed later in Section 3.3.4.

The fitted rotational parameters for the upper state are given in Table 3.2. No formal fit was performed, but these parameters were adjusted sequentially until the simulation reproduced the rotational line positions. Vibrational parameters were determined by fitting the band origins against Equation 3.2, and the equilibrium rotational constants were found by fitting B_v to Equation 3.3. All are in good agreement with the literature values. The vibrational constants (Table 3.3) differ slightly from those reported by Harrington,[165] but those were based on estimated band origins using the band head positions and so are less accurate than these updated values.

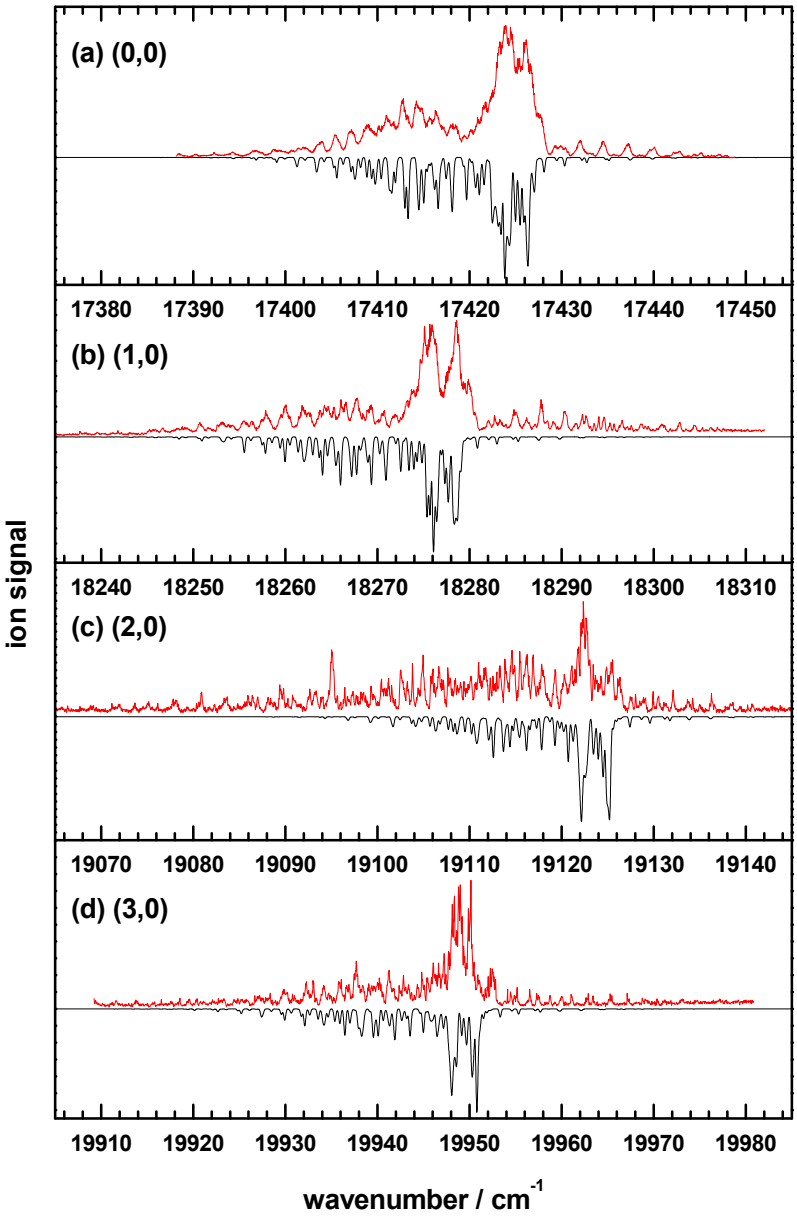


Figure 3.5: $C - X$ $(1 + 1')$ spectra, $(0, 0)$ to $(3, 0)$. Simulations were carried out at 30 K, with a Gaussian FWHM of $0.25\,\mathrm{cm}^{-1}$.

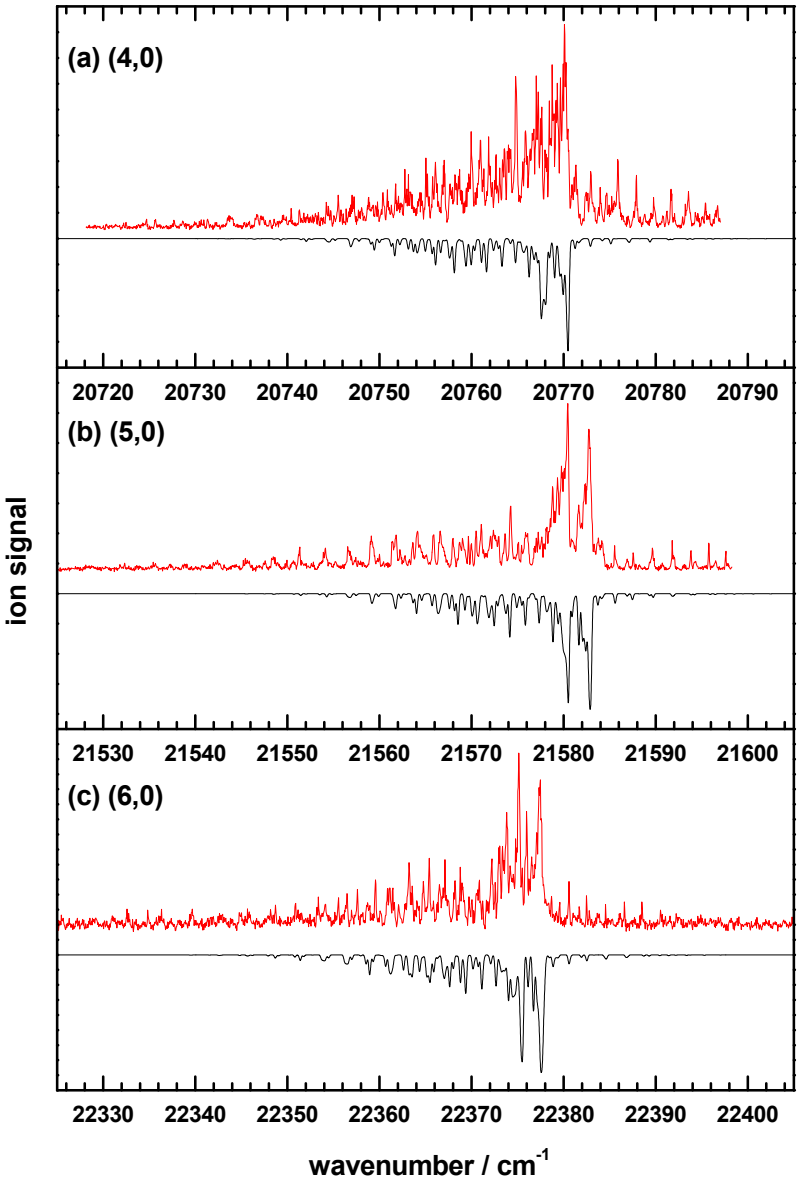


Figure 3.6: $C - X$ $(1 + 1')$ spectra, $(4, 0)$ to $(6, 0)$. Simulations were carried out at 30 K, with a Gaussian FWHM of $0.25\,\mathrm{cm}^{-1}$.

Table 3.2: Fitted $C^4\Sigma^-$ parameters. The estimated uncertainty in the least significant digit is given in parenthesis.

	$C\,^4\Sigma^-$ v′						
Molecular parameters	**0**	**1**	**2**	**3**	**4**	**5**	**6**
T_0 / cm^{-1}	17420.1(2)	18272.9(2)	19119.7(2)	19945.5(2)	20765.2(2)	21577.8(2)	22373.0(2)
B / cm^{-1}	0.496(2)	0.489(2)	0.484(2)	0.484(2)	0.48(2)	0.477(2)	0.471(2)
D / cm^{-1}	Fixed at 6.44×10^{-7}, from D' value given by Cheung *et al.*[157]						
λ / cm^{-1}	0.70(20)	0.66(20)	0.55(20)	0.60(20)	0.60(20)	0.60(20)	0.60(20)
γ / cm^{-1}	-0.020(10)	-0.020(10)	-0.015(10)	-0.025(10)	-0.020(10)	-0.020(10)	-0.020(10)
γ_D / cm^{-1}	Fixed at 5.43×10^{-7}, from γ'_D value given by Cheung *et al.*[157]						

Table 3.3: Calculated equilibrium parameters of the $C^4\Sigma^-$ state. The estimated uncertainty in the least significant digit is given in parenthesis. Literature values are given in square brackets.

T_e / cm^{-1}	17490.2(2) [17494.3]
ω_e / cm^{-1}	864.77(20) [863.4]
$\omega_e x_e$ / cm^{-1}	5.61(20) [5.35]
B_e / cm^{-1}	0.4959(20) [0.4953]
α_e / cm^{-1}	0.0037(20) [0.0035]

$$T_v = \left(v + \frac{1}{2}\right)\omega_e - \left(v + \frac{1}{2}\right)^2 \omega_e x_e \tag{3.2}$$

$$B_v = B_e - \left(v + \frac{1}{2}\right)\alpha_e \tag{3.3}$$

The intensities of these transitions are, however, surprising. The equilibrium bond lengths in the $v = 0$ vibrational level are 1.5921 Å and 1.6747 Å for the X and C states respectively. Thus, one would expect small Franck-Condon factors and hence small transition probabilities for transitions with large values of Δv. Figure 3.7 gives the calculated Franck-Condon factors based on vibrational wavefunctions calculated from these bond lengths and the VO vibrational constants. These predict a very different intensity profile to that observed in experiment.

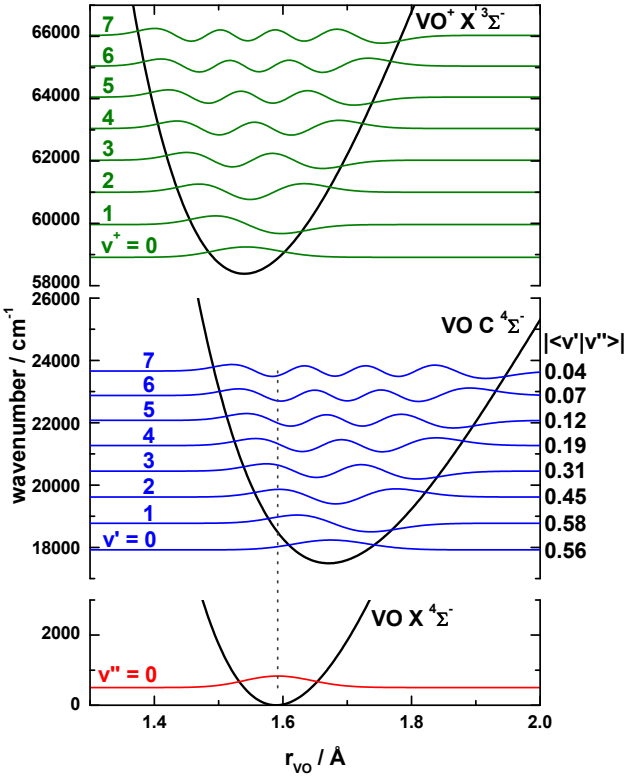


Figure 3.7: Simulation of Morse potential and vibrational wavefunctions of the VO $X\,^4\Sigma^-$ and $C\,^4\Sigma^-$ states, and $VO^+\,X\,^3\Sigma^-$ for the observed REMPI transitions. The vertical dotted line marks the position of the average V-O bond length in the $v'' = 0$ level. Franck-Condon factors $|\langle v'|v''\rangle|$ are given for the overlap of the X ground vibrational level with the vibrational levels of the C state. This predicts a maximum peak intensity at the (1, 0) band, an order of magnitude larger than that of the weakest bands.

Figure 3.7 shows the simulated vibrational wavefunctions, assuming a Morse potential. Rotational and vibrational parameters of the X and C states were taken from Flory and Ziurys[167] and this study, respectively. The similarity of the bond lengths favours transitions with small values of Δv, with the most intense transition being the (1, 0). The Franck-Condon factor of the (7, 0) band is around 10 % of that of the (1, 0). In the experimental spectrum, however, the (5, 0) band has the highest intensity in both $(1 + n)$ and $(1 + 1')$ REMPI.

Instead, the observed intensities of the progression are better explained by the Franck-Condon overlap of the excited VO $C\,^4\Sigma^-$ state with ground state of the molecular cation, $VO^+\ X\,^3\Sigma^-$. This ion was found to have an equilibrium bond length of 1.54 ± 0.01 Å by photoelectron spectroscopy.[168] Several vibrational levels of the ion are accessible in the ionisation step, and as the tunable laser is scanned towards higher wavenumbers, the number of accessible levels increases, many of which have appreciable overlap with the

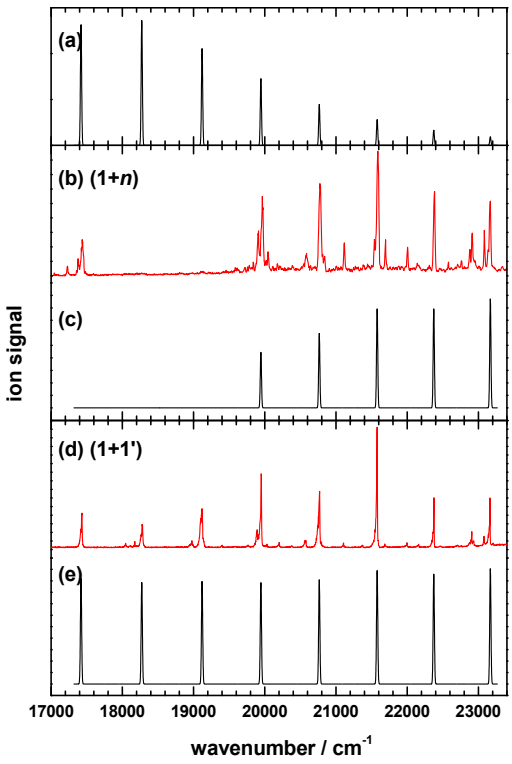


Figure 3.8: VO $X\,^4\Sigma^- - C\,^4\Sigma^-$ REMPI spectra simulated based on Franck-Condon intensities. (a) Simulation of the VO $C\,^4\Sigma^- - X\,^4\Sigma^-$ transition only. (b) Broadband $(1+n)$ REMPI spectrum. (c) Simulation of the VO^+ $X\,^3\Sigma^-$ – VO $C\,^4\Sigma^-$ transition, based on cation vibrational levels accessible with three photons of the tunable visible beam. (d) Broadband $(1+1')$ REMPI spectrum. (e) Simulation of the VO^+ $X\,^3\Sigma^-$ – VO $C\,^4\Sigma^-$ transition, based on cation vibrational levels accessible with one photon of the tunable visible beam plus one photon from the ionisation laser at 230 nm.

C state v' level. If this Franck-Condon overlap is taken as an approximation to the ionisation probability, the predicted intensities is a much better match to experiment (Figure 3.8).

3.3.3 $B\,^4\Pi - X\,^4\Sigma^-$ transition

A much weaker band than the $C - X$ is present at the red end of the spectrum. It consists of four components with a separation very similar to that of the $(0,0)$ and $(1,0)$ bands of the $B\,^4\Pi - X\,^4\Sigma^-$ previously observed by Merer *et al.* using fluorescence spectroscopy.[156,169,170] The $(2,0)$ band and a number of hot bands have also been recorded without rotational resolution, allowing the determination of the vibrational constants.[165] The band origins of the weak peaks observed here are within $8\,cm^{-1}$ of the four components of the $B\,^4\Pi - X\,^4\Sigma^-(4,0)$ transition, as predicted by these vibrational constants, allowing us to assign these peaks.

The rotational levels of the B state are best described by Hund's case (a), since the

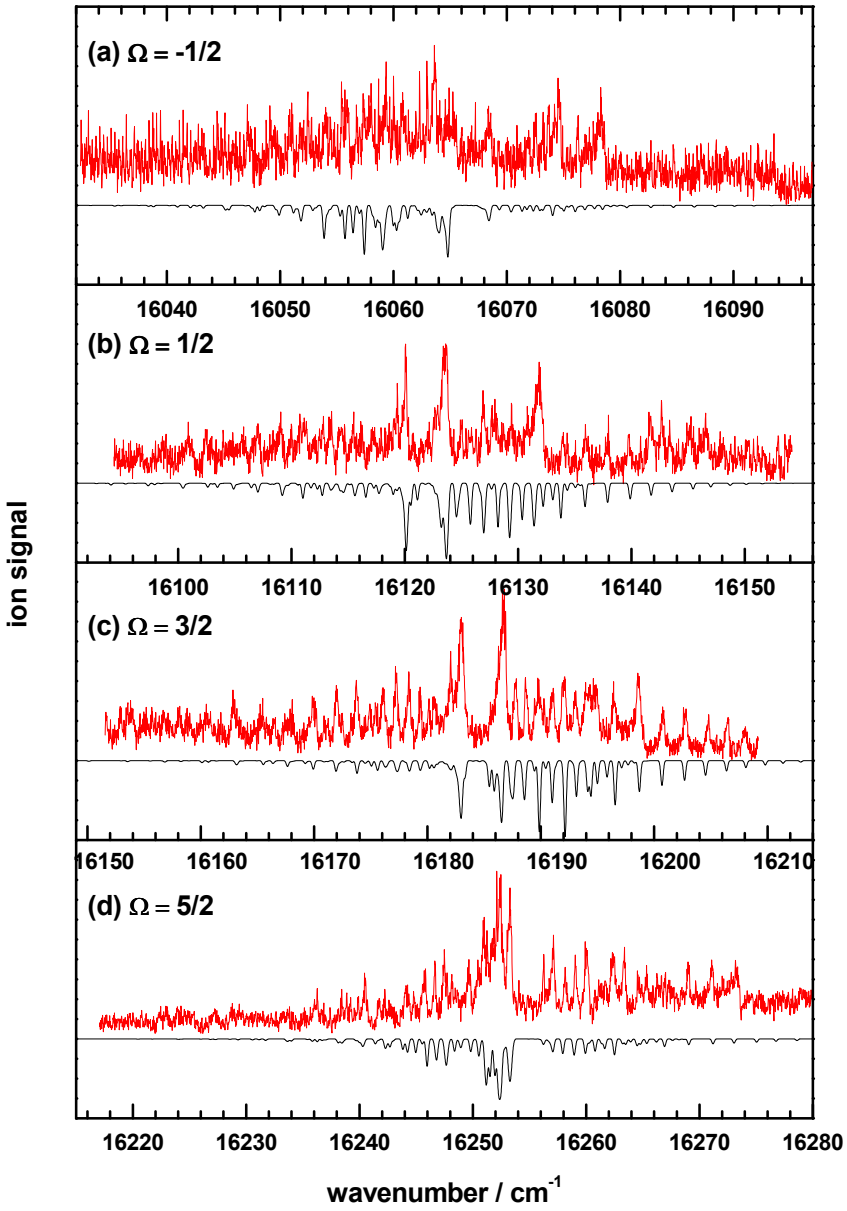


Figure 3.9: $B\,^4\Pi - X\,^4\Sigma^-$ spectrum. Simulations were carried out at 30 K, with a Gaussian FWHM of 0.25 cm^{-1}.

spin-orbit components of this state are separated by *ca.* 60 cm^{-1}. The orbital angular momentum is $\Lambda = 1$ because the configuration of the state is $\delta^2\pi$. The projection of the $S = \frac{3}{2}$ spin onto the internuclear axis couples with Λ to give four spin-orbit components with $\Omega = \frac{5}{2}, \frac{3}{2}, \frac{1}{2}$ and $-\frac{1}{2}$. Each rotational level with quantum number J has an e and f parity component which are close in energy, split by Lambda-doubling.

The lower state is the X state, discussed previously in Section 3.3.2. Transitions between this and the B state follow the selection rules already given in Table 3.1, leading to 12 P, Q and R branches for each $B\,^4\Pi_\Omega$ term. The transitions were simulated as before (Figure 3.9). Since this is a fairly weak band, the signal-to-noise ratio is not high enough to fit many of the rotational constants of the excited state, and so the previously determined $(1, 0)$ constants were used for the spin rotation coupling constant, spin-spin coupling constant, and centrifugal distortion constants.[170] As before, the ground state parameters were fixed to those determined by Flory and Ziurys.[167] The rotational constant B and band origin T_0 were varied until a good match to the experimental spectrum was found. The rotational constant was found to be $B_4 = 0.506 \pm 0.002\,cm^{-1}$, in agreement with that predicted by the equilibrium constants of Harrington *et al.*, which give this value as $0.05066\,cm^{-1}$.[165] Band origins for the four components are given in Table 3.4.

Table 3.4: Calculated band origins of the $B\,^4\Pi$ state. The estimated uncertainty is given in parenthesis.

Ω	**Origin / cm^{-1}**
$-\frac{1}{2}$	16058.3 (0.2)
$\frac{1}{2}$	16122.6 (0.2)
$\frac{3}{2}$	16186.9 (0.1)
$\frac{5}{2}$	16249.7 (0.1)

3.3.4 $2\,^2\Pi - X\,^4\Sigma^-$ transition

In addition to the readily identifiable quartet transitions, several new vibrational progressions were observed in the broadband REMPI spectra. The rotational structure is that of a $\Sigma - \Pi$ transition, very different to that of the $C - X$ bands which dominate the spectrum. Although $B\,^4\Pi - X\,^4\Sigma^-$ bands have been observed (Section 3.3.3), the $B - X$ vibrational spacing is nearly $100\,\mathrm{cm}^{-1}$ smaller than in the bands observed here. Likewise, $A\,^4\Pi - X\,^4\Sigma^-$ transitions can be ruled out on the basis of vibrational spacing.

Both of the new progressions comprise pairs of peaks, suggesting that one of the states involved is a $^2\Pi$ state and that the pairs of peaks are the two spin-orbit components $^2\Pi_{3/2}$ and $^2\Pi_{1/2}$. As can be seen from Figure 3.1, from the ground state there are four energetically accessible $^2\Pi$ states in the 17000 to $24000\,\mathrm{cm}^{-1}$ region.

The first progression, starting at $18044\,\mathrm{cm}^{-1}$, was simulated as a $^2\Pi - X^4\Sigma^-$ transition. The ground state constants were fixed at the values determined by Flory and Ziurys,[167] and the upper state parameters were varied to best fit the spectra. The varied parameters were: band origin $T_{v,\Omega}$, rotational constant $B_{v,\Omega}$, centrifugal distortion constant $D_{v,\Omega}$, and Ω-doubling constant p_v. These simulations are shown next to the experimental spectra in Figure 3.10. Upper state parameters determined by these simulations are given in Table 3.5.

Table 3.5: Fitted $2\,^2\Pi$ parameters. The estimated uncertainty in the least significant digit is given in parenthesis.

Molecular parameter	$\mathbf{2\,^2\Pi_{1/2}, v = 0}$	$\mathbf{2\,^2\Pi_{3/2}, v = 0}$	$\mathbf{2\,^2\Pi_{1/2}, v = 1}$	$\mathbf{2\,^2\Pi_{1/2}, v = 4}$
T_v / cm^{-1}	18044.3(2)	18164.9(2)	18976.9(2)	21682.8(2)
B / cm^{-1}	0.524(2)	0.526(2)	0.516(2)	0.516(2)
p_v / cm^{-1}	-0.02(2)	0	-0.03(1)	0.10(4)
D / cm^{-1}	$5(4) \times 10^{-6}$	$5(4) \times 10^{-6}$	$5(4) \times 10^{-6}$	$5(4) \times 10^{-6}$

Of the previously observed $^2\Pi$ states, the rotational constant of this $(0, 0)$ band is closest to the $2\,^2\Pi_{3/2}$ arising from a $\sigma\delta\pi$ configuration, with $B_0 = 0.52646\,\mathrm{cm}^{-1}$.[158] The

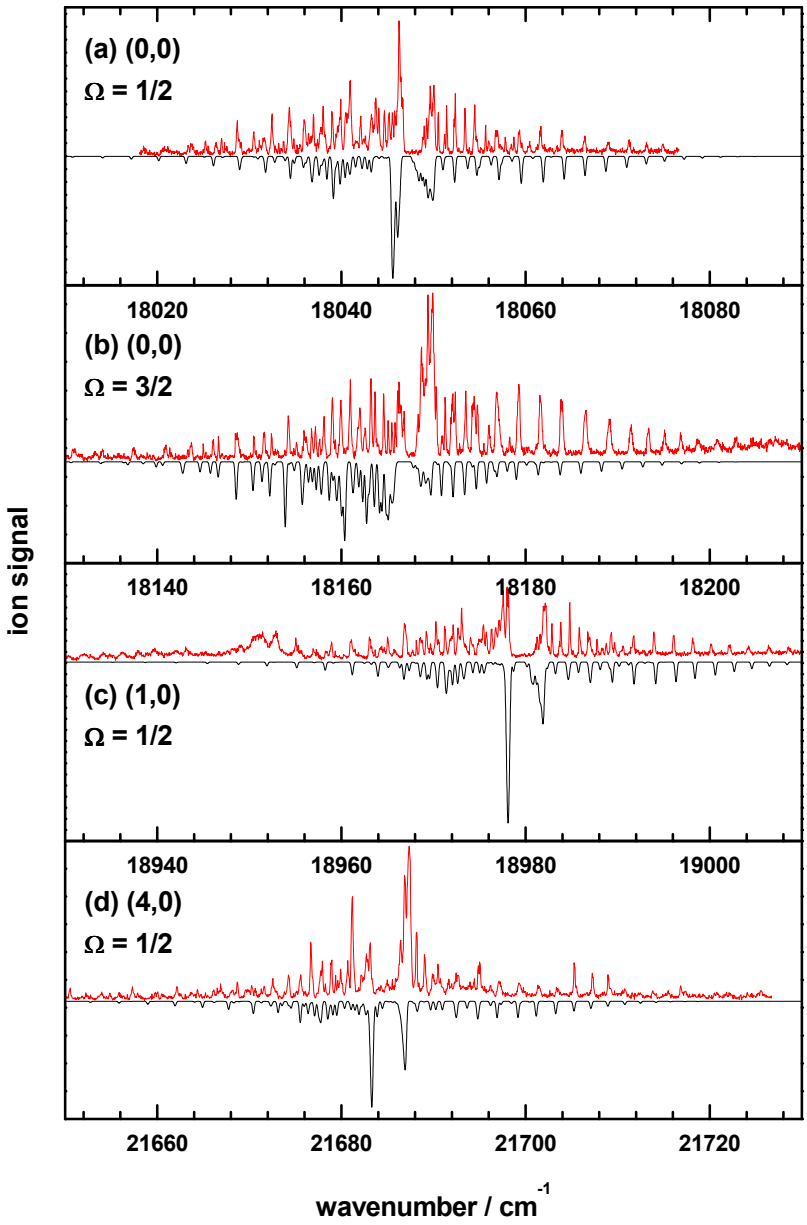


Figure 3.10: $2\,^2\Pi - X\,^4\Sigma^-$ spectra. Simulations were carried out at 30 K, with a Gaussian FWHM of $0.25\,\mathrm{cm}^{-1}$.

only other recorded $^2\Pi$ state, the $1\,^2\Pi$ state, has a slightly smaller rotational constant: 0.521151 and 0.518588 cm^{-1} for the $\Omega = \frac{1}{2}$ and $\Omega = \frac{3}{2}$ components, respectively.[162] In the absence of significant configuration mixing, the $1\,^2\Pi$ state is, however, inaccessible from the ground state in a single electron transition because its configuration is $\sigma^2\pi$.

A third $^2\Pi$ state should arise from the $\delta^2\pi$ configuration. This would be accessible through a $\pi \leftarrow \sigma$ promotion, and may also lie in approximately this region of the spectrum. As it has not been observed in any previous studies, its rotational structure cannot be compared to the state reported here. The spin-orbit separation of this state can, however, be estimated using the separation of the components of the $B^4\Pi$ state, which arises from the same $\delta^2\pi$ configuration. The approximate separation can be found in terms of the atom-like spin-orbit couplings by applying the $\mathbf{AL_zS_z}$ operator to the configuration.

$$\begin{aligned} T\left(^4\Pi_{\frac{5}{2}}\right) - T\left(^4\Pi_{-\frac{1}{2}}\right) &= \langle \delta^+\alpha\, \delta^-\alpha\, \pi^+\alpha | \mathbf{AL_zS_z} | \delta^+\alpha\, \delta^-\alpha\, \pi^+\alpha\rangle \\ &\quad - \langle \delta^+\beta\, \delta^-\beta\, \pi^+\beta | \mathbf{AL_zS_z} | \delta^+\beta\, \delta^-\beta\, \pi^+\beta\rangle \\ &= (a_\delta(2)(1/2) + a_\delta(-2)(1/2) + a_\pi(1)(1/2)) \\ &\quad - (a_\delta(2)(-1/2) + a_\delta(-2)(-1/2) + a_\pi(1)(-1/2)) \\ &= -a_\pi \end{aligned} \tag{3.4}$$

$$\begin{aligned} T\left(^2\Pi_{\frac{3}{2}}\right) - T\left(^2\Pi_{\frac{1}{2}}\right) &= \langle \delta^+\alpha\, \delta^-\alpha\, \pi^+\beta | \mathbf{AL_zS_z} | \delta^+\alpha\, \delta^-\alpha\, \pi^+\beta\rangle \\ &\quad - \langle \delta^+\beta\, \delta^-\beta\, \pi^+\alpha | \mathbf{AL_zS_z} | \delta^+\beta\, \delta^-\beta\, \pi^+\alpha\rangle \\ &= (a_\delta(2)(1/2) + a_\delta(-2)(1/2) + a_\pi(1)(-1/2)) \\ &\quad - (a_\delta(2)(-1/2) + a_\delta(-2)(-1/2) + a_\pi(1)(1/2)) \\ &= -a_\pi \end{aligned} \tag{3.5}$$

Equations 3.4 and 3.5 show that the difference between the highest and lowest spin-orbit components should be equal in the case of the $\delta^2\pi$ $^4\Pi$ and $^2\Pi$ states. In the B state this difference is 193.52 cm^{-1},[156] 60 % larger than the 120.6 cm^{-1} separation of the two components of the new $^2\Pi$ state. Given this large difference, the new $^2\Pi$ is unlikely to have a $\delta^2\pi$ configuration.

The spin-orbit splitting in the new $^2\Pi$ state does, however, compare favourably to that expected from the $\sigma\delta\pi$ configuration. Using the same method as above, the difference between the highest and lowest components of the $A^4\Pi$ state is $2a_\delta - a_\pi$, which should be the same as for one of the $^2\Pi$ states generated in this configuration. The two measured values are 105.79 cm^{-1} and 120.6 cm^{-1} respectively,[155] supporting the conclusion from the rotational constant that the new state has $\sigma\delta\pi$ configuration and is the 2 $^2\Pi$ state found by Merer *et al.*[158]

Because the energy of the 2 $^2\Pi$ state is known with respect to most of the other doublet states of VO, this observation of the 2 $^2\Pi - C\,^4\Sigma^-$ transition allows the relative energies of the doublet and quartet manifolds to be determined for the first time.

3.3.5 3 $^2\Pi - X\,^4\Sigma^-$ transition

Another new vibrational progression was observed above around 21000 cm^{-1}, with a very similar rotational structure to the 2 $^2\Pi - X\,^4\Sigma^-$ state, but a substantially larger spin-orbit separation. As the transitions are at higher wavenumber than the 2 $^2\Pi$, the 1 $^2\Pi$ state can be ruled out as the upper state. This is assigned as a new state, the 3 $^2\Pi$, on the basis of the rotational structure and the appearance of two components in each vibrational level.

Due to a poor signal-to-noise ratio, high-resolution REMPI spectra could only be obtained for the lower energy component in each case. These are shown in Figure 3.11 along with the simulated spectra, whose fitted parameters are given in Table 3.6. The

ground state parameters were fixed at the known constants of $X\,^4\Sigma^-$.[167] The spin-orbit coupling constant can be taken from the broadband spectra, and is $167 \pm 5\,\mathrm{cm}^{-1}$.

The identity of this new $3\,^2\Pi$ state has two possibilities. Since the first $^2\Pi\,(\sigma\delta\pi)$ was observed, this may be the second one arising from the $\sigma\delta\pi$ configuration. This explanation is supported by the similar rotational constants and vibrational constants.

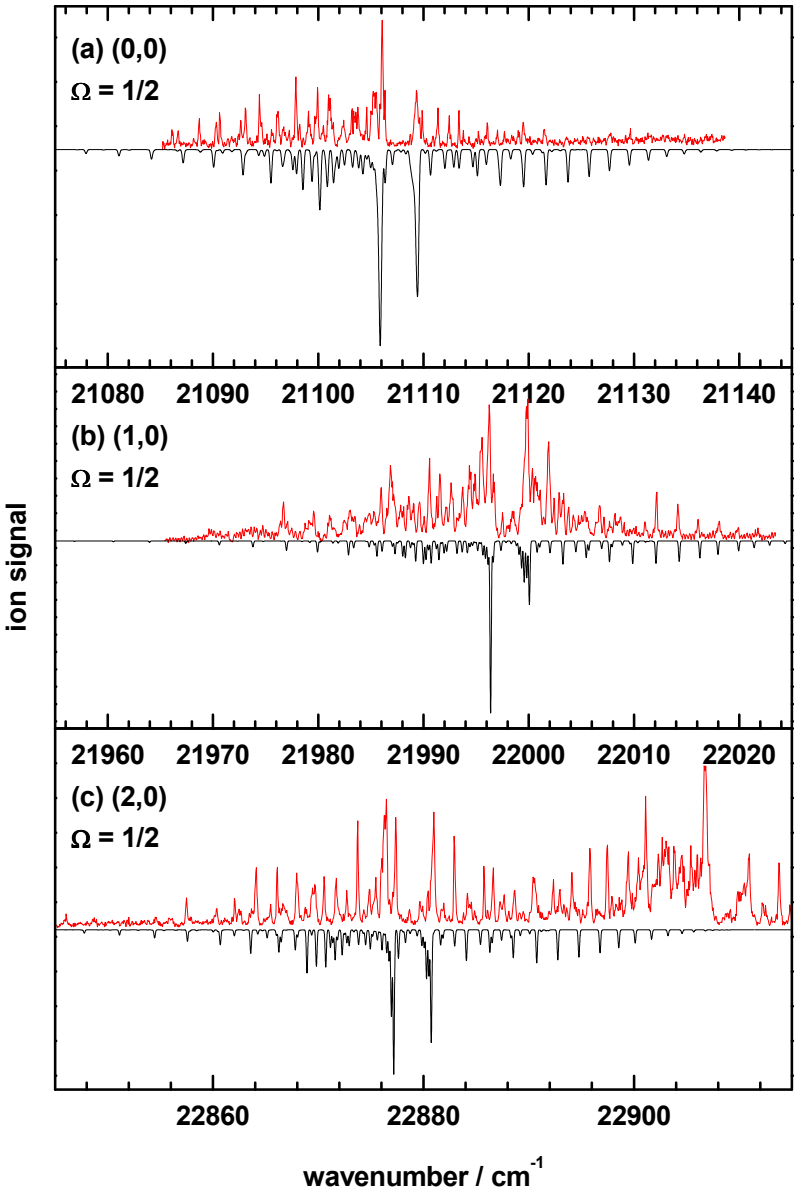


Figure 3.11: $3\,^2\Pi - X\,^4\Sigma^-$ $(1+n)$ REMPI spectrum. Simulations were carried out at 30 K, with a Gaussian FWHM of $0.15\,\mathrm{cm}^{-1}$.

Table 3.6: Fitted $3\,^2\Pi$ parameters. The estimated uncertainty in the least significant digit is given in parenthesis.

Molecular parameter	$\mathbf{3\,^2\Pi_{1/2}, v = 0}$	$\mathbf{3\,^2\Pi_{1/2}, v = 1}$	$\mathbf{3\,^2\Pi_{1/2}, v = 2}$
T_0 / cm^{-1}	21105.2(2)	21995.4(2)	22876.3(2)
B / cm^{-1}	0.513(2)	0.513(2)	0.507(2)
p_v / cm^{-1}	0.15(5)	0.020(10)	0.015(5)
D / cm^{-1}	$5(4) \times 10^{-6}$	$4(2) \times 10^{-5}$	$3(2) \times 10^{-5}$

The alternative is that the $3\,^2\Pi$ state could arise from the same $\delta^2\sigma$ configuration as the $B\,^4\Pi$ state. In this case, the spin-orbit separations of highest and lowest components are comparable: 167 and 193.52 cm^{-1}, respectively, as would be expected if the two states arose from the same configuration (see discussion in Section 3.3.4). The new $^2\Pi$ and the B state also have very similar rotational constants and vibrational spacings.

Although the assignment of this state is inconclusive, the $\delta^2\sigma$ configuration is more likely on the basis of the magnitude of the spin-orbit coupling constant. It would also explain why the $3\,^2\Pi$ state has not yet been observed in emission studies, since fluorescence has so far only been observed from states with $\sigma^2\delta$, $\sigma\delta\pi$ and $\sigma\delta\sigma^*$. Transitions between these states and the $3\,^2\Pi$ would break orbital angular momentum selection rules, whereas some transitions would be allowed if the $3\,^2\Pi$ had a $\sigma\delta\pi$ configuration.

3.3.6 Conclusions and outlook

The REMPI spectrum of VO has been recorded throughout the visible spectral region, in both medium and high resolution. The spectroscopic constants of several excited states have been determined: $C\,^4\Sigma^-(0,0)-(6,0)$, $B\,^4\Pi(4,0)$ and $2\,^2\Pi(0,0)-(4,0)$. The observation of the latter state reveals the relative energies of the doublet and quartet states of VO for the first time. A new state, the $3\,^2\Pi$, has also been observed in a REMPI transition from the ground state, and its spectroscopic constants determined.

Higher resolution spectra of VO, such as with a ring dye laser, are needed to confirm

the identity of the new states, since the overlapping lines here complicates the analysis and prevents complete identification of rotational lines. Higher-resolution spectra may also be able to identify the weaker bands observed in broadband ($1 + 1'$) spectra.

Chapter 4

Velocity Map Imaging Studies of Au_2 †

4.1 Introduction

The spectroscopic experiments described in Chapters 2 and 3 employ mass spectrometry to determine the products of photon absorption, and the time-of-flight instrument can also detect the products of photodissociation. In these experiments, however, the final states of the fragments cannot easily be determined. More information on the energetics of the dissociation could be gained if the kinetic energy of the products could be measured, because the photon energy is partitioned between the fragments' internal and kinetic energies. This can be measured using a time-of-flight mass spectrometer, but only a small fraction of the ion signal can be captured, and measuring the angular dependence is problematic because either the detector or the laser polarisation must be rotated.[172,173] Spectroscopic techniques for determining product quantum states such as laser-induced fluorescence (LIF) and REMPI are also generally inapplicable to

†Some of the results in this chapter have been published as *VUV photodissociation dynamics of diatomic gold, Au_2: A velocity map imaging study at 157 nm*.[171]

metal clusters because they rely on the products having well-characterised spectra. Ion imaging optics have since been developed which project the products onto a position-sensitive detector, allowing the kinetic energy distribution to be determined in order to decipher the photodissociation dynamics.

Developed by Eppink and Parker in 1997, Velocity Map Imaging (VMI) is a powerful technique for investigating the dynamics of photodissociation processes and cross-beam reaction studies. VMI has been applied to a large range of organic and small non-metal inorganic systems, summarised in a recent review by Ashfold *et al.*,[174] because they are easily introduced into a molecular beam and the photodissociation or reaction products are light, usually monatomic species, which are ideal for imaging because they can be ionised with convenient and efficient REMPI schemes, resulting in well-resolved images.

Although several groups have applied photoelectron imaging to metal clusters,[85–87,175] few studies have imaged the metal atoms themselves.[176,177] In this chapter, the application of VMI to the gold diatomic molecule, Au_2, is discussed. Two related experiments were performed: photodissociation in the vacuum-UV at 157 nm, and imaging across a REMPI spectrum in the near-UV.

4.2 Photodissociation

When a molecule is photodissociated, the fragments recoil from each other with a total kinetic energy release (TKER) equal to the difference between the photon energy and the energy of the products plus the dissociation energy, as shown in Figure 4.1. Assuming that the molecule is initially in its ground vibrational level, the energy balance is given by Equation 4.1.

$$nh\nu = D_0(\mathrm{AB}) + E_{\mathrm{int}}(\mathrm{A}) + E_{\mathrm{int}}(\mathrm{B}) + \mathrm{TKER} \tag{4.1}$$

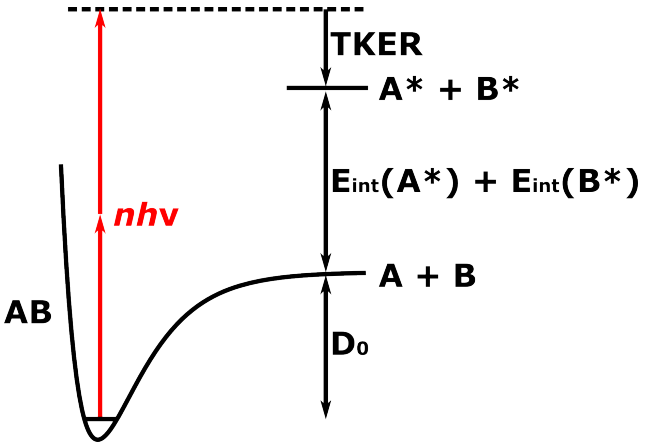


Figure 4.1: Schematic photodissociation of a bond between atoms or molecules A and B, from the ground state of AB. The molecule is excited above a dissociation threshold, and fragments into A* and B*. The excess energy is released in the form of total kinetic energy of the two fragments (TKER).

where these parameters are defined in Figure 4.1.

The conservation of momentum ($m_A v_A + m_B v_B = 0$ in the centre of mass frame) determines how the TKER is partitioned between the two fragments according to their relative masses:

$$\begin{aligned} \mathrm{KER_A} &= \mathrm{TKER}\frac{m_B}{m_{AB}} \\ \mathrm{KER_B} &= \mathrm{TKER}\frac{m_A}{m_{AB}} \end{aligned} \tag{4.2}$$

This implies that for a given pair of products A and B, the magnitude of their velocities are determined only by the photon energy and final states of the of the products. If the photodissociation occurs in a small volume, such as the intersection of a molecular beam and a laser, the products are distributed on the surface of two expanding spheres (known as Newton spheres), or on a series of concentric spheres if either product has more than one accessible final state.

The distribution of the products over the Newton sphere is governed by the angular momentum change and subsequent dynamics of the photodissociation transition. Single-photon absorption is most probable when the electric vector of the photon $\boldsymbol{\epsilon}$ is aligned with the transition moment $\boldsymbol{\mu}$, and has zero probability when the two vectors

are perpendicular. When a parallel transition is excited ($\Delta\Omega = 0$), in which $\boldsymbol{\mu}$ is parallel to the internuclear axis, molecules aligned with the polarisation of the light will be preferentially photolysed. Conversely, perpendicular transitions ($\Delta\Omega = \pm 1$) preferentially photolyse molecules in the plane perpendicular to the polarisation vector. These limiting distributions are only observed, however, if the photodissociation process occurs on a timescale much shorter than the rotational period of the molecule; if this is not the case, the molecule can rotate and change its alignment before fragmenting, leading to a more isotropic distribution.

For one-photon dissociation, the distribution is described by Equation 4.3 as a function of θ, the angle between $\boldsymbol{\epsilon}$ and the fragment velocity vector.[174] β_2 is the anisotropy parameter, and takes the values of 2 for pure parallel transitions, -1 for pure perpendicular transitions, and 0 when the distribution is isotropic.

$$I(\theta) = \frac{1 + \beta_2 \left(3\cos^2\theta - 1\right)/2}{4\pi} \tag{4.3}$$

Multiphoton excitation further complicates the distribution, which becomes the sum of the first $2N$ Legendre polynomials for an N-photon process:

$$I(\theta) = \frac{1 + \sum_{n\geq 2}^{2N} \beta_n P_n(\cos\theta)}{4\pi} \tag{4.4}$$

where P_n is the nth Legendre polynomial. The limiting values of β_n now depend on the angular momentum of the initial, final and intermediate molecular states in the multiphoton excitation.[178]

In all cases described by these equations, the distribution of ions is cylindrically symmetric about the polarisation vector $\boldsymbol{\epsilon}$, and so the two-dimensional image of the crushed spheres can be used to work back to the original three-dimensional distribution. There are several different approaches to performing this deconvolution, which will be dis-

cussed in Section 4.2.2.

It is possible to infer the velocity and anisotropy of expanding spheres state-selectively using Doppler spectroscopy: the absorption frequencies of the fragments depend linearly on their velocity along the axis of a probe beam, and this shift can be measured using a technique like LIF or REMPI.[179,180] The probe beam is tuned around a known absorption of the fragment, making this technique state-selective. The measured spectrum is that of a one-dimensional projection of the three-dimensional velocity distribution, so this must be recorded as a function of pump-probe angle in order to deconvolute the spectrum and determine the original velocity distribution.

Doppler spectroscopy is most successful when the probed fragment is very light; the lighter fragment recoils with the greater velocity (Equation 4.2), increasing the Doppler shift and hence the sensitivity of the technique. For this reason, Doppler spectroscopy has been applied mainly to photodissociation and scattering experiments with relatively light products, hydrogen in particular,[180–182] but also other light atoms[183,184] and small polyatomic species.[185,186]

4.2.1 Imaging techniques

The development of position-sensitive detectors has led to Doppler spectroscopy being largely superseded by ion imaging, in which the 3D velocity distribution is projected onto a 2D screen, allowing the simultaneous measurement of the particles' internal energies and the angular dependence of their velocities. A major advantage of ion imaging is that whereas Doppler spectroscopy requires a well-resolved absorption or emission spectrum, imaging can be applied to any fragment species that is either ionic or that can be ionised. The ionisation process forms a cation and an electron which also recoil from one another and, for ensembles, form two Newton spheres. Except in the case of very light fragments such as hydrogen atoms, this does not measurably blur the ion

image because the electron takes away the vast majority of the excess kinetic energy arising from photoionisation, due to the conservation of momentum (Equation 4.2).

Ion imaging was first introduced by Chandler and Houston, who imaged the CH_3 fragments produced in CH_3I photolysis.[187] Photodissociation at 266 nm forms CH_3 and I atom, which may be in the ground $^2P_{3/2}$ or excited $^2P_{1/2}$ state. More kinetic energy is available when I is formed in the ground state, so two concentric spheres of methyl radicals are created, the larger corresponding to dissociation into the I $^2P_{3/2}$ channel. The CH_3 products were ionised by $(2+1)$ REMPI in an electric field created between an electrode plate held at a high potential and a grounded grid, accelerating the ions towards the detector. The detector consisted of a phosphor screen to collect the amplified ion signal from a microchannel plate, and polaroid film to record the image from the phosphor screen. The projection of the two spheres onto the screen produces two rings corresponding to the two dissociation channels, and their velocities were determined from the ring radius and the ion time of flight.

Including a second grid at an intermediate potential, as in a Wiley-McLaren type time-of-flight mass spectrometer[41] (see Section 2.3.1), improves the temporal resolution of the ions: the two electric fields can be tuned to cause ions which originate further from the detector to enter the drift tube with higher velocities so that all ions of the same m/z arrive at the detector together. The ions of interest arrive at the detector simultaneously, and the detector is gated to only image those ions.[188] Although the grids are necessary to create a uniform electric field between the electrodes, they also distort the ion trajectories, blurring the final image.[189,190] Blurring is reduced when just one grid is used (sacrificing some time-of-flight resolution), but it is not eliminated completely. The image resolution is further reduced by the variation of ion birth positions: ions are formed in the intersection of the molecular beam and the laser beam(s), and so the image is blurred by the width of this intersection volume. Focusing the beams can compensate

for this by reducing the intersection volume, but can introduce unwanted multiphoton absorptions and space-charge effects from high ion number densities.

Eppink and Parker found an elegant solution to both of these problems by removing the grids completely from the time-of-flight electrode arrangement.[191] Clearly, this avoids the blurring caused by the grids, but it also curves the electric field between the electrodes. The curvature has the useful effect of focussing ions with the same initial velocity to the same point on a 2D detector, regardless of their initial position. This solution, named Velocity Map Imaging (VMI), significantly improves the resolution of ion images while preserving the time-of-flight focussing and the linear relationship between ring radius and fragment velocity. The Newton sphere expansion is increased slightly by the electric field curvature, so that the radius is given by Equation 4.5:

$$R = Nvt \tag{4.5}$$

where v is the off-axis velocity, t is the time of flight and N is a mass-independent magnification factor which is greater than 1. N must be calibrated using a known photodissociation process because it is exquisitely dependent on certain dimensions of the VMI instrument such as the diameter of the electrode holes or the relative positions of the electrodes and photodissociation beam.

Due to these improvements, VMI has superseded ion imaging with grids and has been applied to a large range of systems. Most of these involved light di- and triatomic precursor species, for example the oxides of nitrogen[192–194] and the hydrogen halides,[195,196] because their product state distributions can be well-resolved using VMI. Larger organic molecules have also been investigated,[197,198] as well as more exotic species like weakly-bound complexes,[199,200] molecular cations[201,202] and rare gas clusters.[203] The reviews by Ashfold *et al.*[174] and more recently by Chichinin *et al.*[204] provide a comprehensive summary of photodissociation applications of VMI.

Metal clusters have been investigated with anion photodetachment imaging, in which VMI is applied to the photoelectron. For example, the jellium model of electrons in alkali clusters has been tested on medium-sized sodium clusters ($19 \leq n \leq 147$),[85] and the size-dependent electronic band structure of mercury clusters has also been probed.[86] Small gold hydrides have yielded vibrationally-resolved photoelectron images, which allow their ground state structures to be determined.[87] Structures of anionic lead clusters have also been studied using the anisotropy of the photoelectron images.[175] Imaging the metal atoms themselves is possible, but has been used in very few studies and only for very small systems such as transition metal oxide diatomics.[176,177]

4.2.2 Image reconstruction

A group of experimental techniques called slicing can be used to extract only a narrow portion of Newton spheres, so that the ion kinetic energies can be measured directly without the need for interpreting the 3D distribution after it has been crushed onto the detector. This can be done by ionising a thin slice of the expanding spheres (optical slicing) or by adjusting the ion optic voltages to elongate the photofragment product distribution along the time-of-flight axis so that there is a larger spread in arrival times, and then gating the detector to capture only the central portion of the spheres (DC and pulsed field slicing).[174]

The use of slicing, however, introduces extra experimental complications, and involves deliberately neglecting a significant fraction of the photofragments produced. Given the low number densities of metal clusters typically generated by laser ablation, it was decided early on in the design of the VMI apparatus that this was too high a price to pay. An alternative approach is to interpret the 2D projection of the projected Newton spheres in the recorded image to determine the original 3D distribution. A number of approaches to this have been developed since the first ion imaging experiments, each

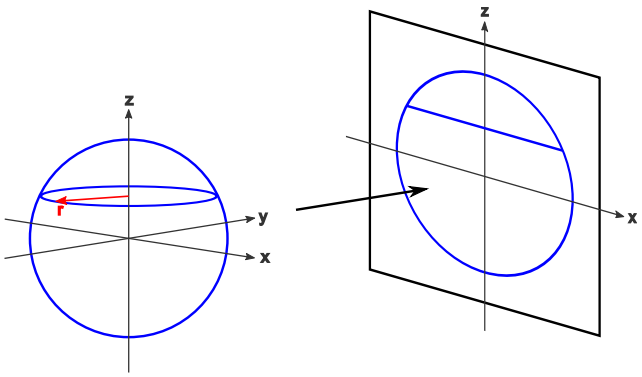


Figure 4.2: Projection of a circular slice of a Newton sphere onto the screen.

attempting to efficiently reverse the projection of the spheres onto the detector.

In most photodissociation processes, the product recoil distribution is cylindrically symmetric about the photon polarisation vector, which is aligned parallel to the detector. A thin slice perpendicular to this symmetry axis comprises a circularly symmetric distribution of particles $f(r)$, which are projected onto a line on the detector (Figure 4.2). The projection of the circle onto this line is given by:

$$\begin{aligned} P(x) &= \int_{-\infty}^{\infty} f(r)\,\mathrm{d}y \\ &= 2\int_{0}^{\infty} f(r)\,\mathrm{d}y \end{aligned} \tag{4.6}$$

Since $r^2 = x^2 + y^2$, Equation 4.6 can be rearranged in terms of r and x:

$$P(x) = 2\int_{x}^{\infty} \frac{r f(r)\,\mathrm{d}r}{\sqrt{r^2 - x^2}} \tag{4.7}$$

Equation 4.7 is the Abel Transform. In order to interpret an experimental image, the most direct approach is to perform the *inverse* Abel Transform, given by Equation 4.8.[205]

$$P(r) = -\frac{1}{\pi}\int_{r}^{\infty} \frac{\mathrm{d}r/\mathrm{d}x}{x\sqrt{x^2 - r^2}} \tag{4.8}$$

An experimental image is, however, not a continuous function but is formed of dis-

crete pixels recorded on a CCD camera or other position-sensitive detector, so numerical differentiation and integration must be performed, usually by a Fourier-Hankel transform method.[206] This procedure is efficient but tends to enhance any noise present in the data, especially towards the singularity at $x^2 = r^2$, producing characteristic centre-line noise down the z-axis of the image.

Alternative approaches can reduce the noise in the reconstructed image by exploiting prior knowledge about the form of projected Newton spheres, rather than applying the inverse Abel transform to each individual line of the image. This was used in the regularisation method of Winterhalter *et al.*, who fitted the image angular distribution to Legendre polynomials.[207] This approach was found to be particularly powerful when the kinetic energy release was large relative to the kinetic energy imparted by the VMI electric fields, but is time-consuming to use because specific input parameters are required for each system.

Iterative methods have also been developed which fit the raw data to a forward convolution of simulated Newton spheres.[208,209] The fitting procedure is relatively slow, but eliminates the centre-line artifacts and performs well on images which are noisy, contain sharp features or have large dynamic ranges.

One of the most widely-used reconstruction methods is BASEX, developed by Reisler *et al.*.[210] They generated a basis set of two-dimensional images based on the projection of simulated Newton spheres, and used it to fit raw images by using matrix methods to calculate the coefficients of the basis functions. The fit is performed in Cartesian coordinates, leading to some centre-line noise, but markedly less than in the Fourier-Hankel method. This noise can be removed by performing the fit in polar coordinates, as in the pBasex method, which is of a similar accuracy to BASEX but over an order of magnitude more efficient.[211]

Another popular method is the onion-peeling method.[195,212] An ion sphere is imaged

on the detector as a ring with a radius determined by the kinetic energy of the particles. The highest intensities occur at the outer edge of the sphere, and only the area of the detector within this radius will detect ions. The onion-peeling algorithm iterates over the detector pixels, starting from those furthest from the centre. When the outer edge of a ring is encountered, its intensity is used to calculate the form of the rest of the flattened sphere within this radius. This function is subtracted from the whole image, and the process is repeated towards the image centre. The algorithm is intuitive and efficient, although error propagates towards the centre-line of the image as more simulated rings are subtracted.

The centre-line noise can be alleviated by performing the same process in polar co-ordinates. The method is known as polar onion-peeling (POP),[213] and has been further optimised for ion imaging by Roberts *et al.*.[214] In polar coordinates, onion-peeling is extremely computationally cheap, with performance comparable to that of pBasex.

Once the Newton spheres have been extracted from the raw data, their intensities can be integrated around each sphere to give a plot of intensity versus sphere radius. Using Equation 4.5 and the conservation of momentum, this can be converted to ion intensity versus total kinetic energy of the fragments.

4.3 Gold clusters and Au_2

There has been intense interest in the properties of gold clusters due to their geometry and reactivity, which are unusual even for metal clusters: in contrast to the inert bulk metal,[215] gold nanoparticles are reactive towards a large number of species,[97,216,217] and the clusters exhibit size-dependent reactivity.[218,219] It has been suggested that the uncoordinated edge sites, which are more concentrated in smaller particles than the bulk, may be the origin of this enhanced reactivity.[220,221] These properties suggest that the cluster geometry strongly influences the reactivity of the gold particles.[222]

Although most transition metal clusters favour three-dimensional structures, the lowest-lying geometries of gold clusters have been found to be low-coordination planar structures. The transition between two- and three-dimensional structures is dependent on the charge of the cluster: ion mobility measurements place the 2D-3D transition between 7 to 8 atoms in the case of cationic clusters,[223] but at around 12 atoms for the anions,[224] results later confirmed by gas phase electron diffraction.[225,226] The neutral Au_7 cluster has also been identified as planar by infrared photodissociation.[227] Larger clusters form a variety of structures, including cages[228] and tetrahedra,[227,229] and some even exist as different chiral enantiomers.[37]

Photoionisation studies have sought to explain the electronic structure of gold clusters, and hence understand their surprising properties. Like the other noble metals, the gold atom's ground configuration is $d^{10}s$, but the chemistry is often very different because of the extreme relativistic contraction of the 6s orbital. Photoionisation of small gold clusters shows a pronounced odd-even oscillation in ionisation potentials, since the electron in a cluster with an odd or even number of atoms is being removed from either an open or full shell.[230,231] This effect extends to clusters of up to around 40 atoms,[82] and is also observed in the cluster fragmentation pathways in photoexcitation experiments.[232] Photoelectron spectra combined with structure-specific argon-tagging has also helped to distinguish between different isomeric forms of small clusters.[84]

There is a vast literature of theoretical studies of gold clusters, investigating their size-dependent electronic effects and their reactivity. The planar structures of the smaller clusters have been investigated by many DFT calculations, which suggest that the relativistic contraction is responsible for these geometries.[233] Two reviews by Pyykkö comprehensively list the calculations performed on small gold clusters and complexes.[234,235]

4.3.1 Au_2

One step in understanding the electronic structure of gold clusters is to investigate the properties of the smallest cluster, Au_2, which, as a diatomic molecule, is expected to be the most straightforward to interpret spectroscopically. The ground state is $X\,0_g^+$, and five excited states have been identified: the $A\,0_u^+$ and $A'\,1_u$ states *via* LIF,[236,237] and the $a\,^3\Sigma_{1u}^+$, $B\,0_u^+$ and $B'\,1_u$ by REMPI.[67] The first dissociation threshold was also estimated to be between $2.301 - 2.311$ eV, from perturbations in the LIF spectrum.[237] Some of the earlier spectroscopic work is summarised in Morse's review of transition metal clusters.[238] A higher energy state has been observed at $T_e = 44672.6\,\mathrm{cm}^{-1}$,[239] and matrix isolation spectra revealed others up to around $50000\,\mathrm{cm}^{-1}$.[240,241]

Although strong relativistic effects and spin-orbit coupling complicate the calculation of gold compounds,[234] several computational studies have calculated the properties of the Au_2 ground state and some of the lower-lying excited states with time-dependent density functional theory[242] and multireference many-body perturbation theory.[243]

The experiments in this chapter probe the photodissociation dynamics of Au_2, which are investigated using VMI for the first time. Au_2 photodissociation is challenging to study spectroscopically because the photodissociation products, Au atoms, are already abundant in the molecular beam. In contrast, VMI can easily distinguish between the atomic gold in the molecular beam and the Au_2 photofragments by measuring the off-axis momentum of the latter, allowing the product state distributions to be analysed. In particular, excited states can be selectively ionised to discriminate against the (mostly) ground state Au atoms in the molecular beam.

4.4 Methods

4.4.1 VMI instrument

The experiments were performed on a custom-built VMI instrument (Figure 4.3). Clusters are produced in the laser cluster source described in Section 2.2, equipped with a gold target disc. Pure helium, at a pressure of 8 bar, is used as the carrier gas. This produces a molecular beam containing small neutral Au_n clusters in the size range $n \leq 10$; the distribution can be tuned to optimise Au_2 production. The beam is doubly skimmed before entering the laser excitation region in the electric field between the VMI ion optics, where the molecular beam is crossed perpendicularly by the photodissociation and photoionisation beams (Section 4.4.2), creating the Newton spheres of ions to be extracted by the electric field.

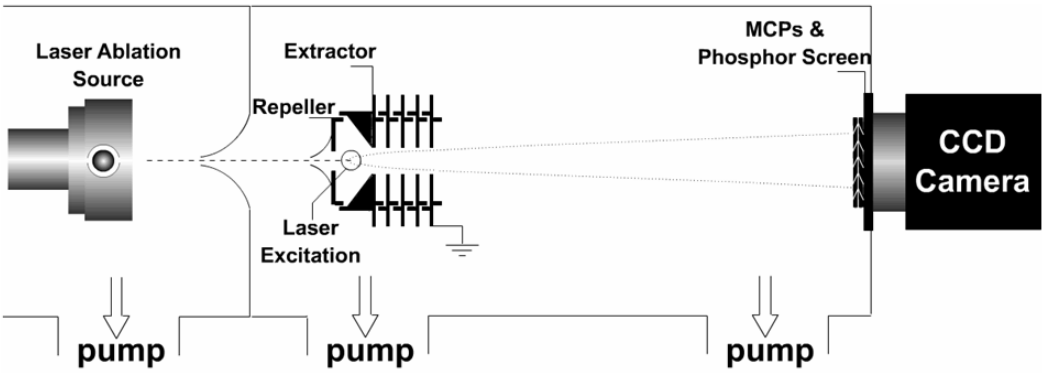


Figure 4.3: Velocity map imaging instrument used in the Au_2 studies.

The VMI electrodes are based on the repeller/extractor/ground arrangement used in the time-of-flight instrument, as described in Section 2.3, with some important differences. The repeller and extractor grids are omitted in favour of Eppink and Parker's open electrode design,[191] which allows the mapping of ions of the same velocity to the same point on the detector. The extractor is not a flat plate, but conical, based on the design of Wrede *et al,*[244] which yields a more homogeneous, parallel field in the source region. After the extractor are four plate electrodes separated by 6 mm, whose poten-

tials are stepped down from the extractor voltage to ground by a series of resistors. This produces a more homogeneous field than a single plate held at 0 V, and reduces the field penetration into the drift region in front of the detector. Fins on the electrodes shield the electric field from distortions by the mounting rods, which are covered by an electrical insulator. The electrode voltage ratio is optimised for velocity mapping, with typical electrode voltages being 3000 V and 2245 V on the repeller and extractor, respectively.

Ions are extracted collinearly with the molecular beam axis, along the 424 mm drift tube to the detector, a commercial ion imaging system built by Photek. It comprises a pair of 40 mm-diameter microchannel plates which amplify the ion signal onto a P46 phosphor screen. The voltage on the rear of the MCP is gated around the arrival time of the ion of interest so that all other species are excluded. The signal from the phosphor is recorded on 776 × 586 pixel CCD camera. Images are accumulated over 30 mins to 2 hours, and subsequently analysed using the polar onion peeling program developed by Roberts *et al.*[214] To convert the image radius to TKER, a VMI magnification factor of 1.05 was used (Equation 4.5). This value was previously determined by the known photodissociation energies of NO_2 into O atom and NO fragments.

Since the VMI instrument separates ions by m/z, the mass spectrum of the clusters can be monitored by connecting the phosphor screen to an oscilloscope directly and measuring the current produced by the ion signal. This is necessary for optimising the cluster source for Au_2 production and for measuring the time-of-flight of the fragment ions so that the MCP can be correctly gated during imaging.

4.4.2 Photodissociation imaging experiments

Two Au_2 photodissociation experiments were performed. In the first, the unpolarised output of an F_2 excimer laser was used for both photolysis and subsequent ionisation. The wavelength of an F_2 laser is composed of two emission lines: one at 157.6311 nm

(90 % of the total intensity) and one at 157.5248 nm (10 %), and the total pulse energy is ~ 1 mJ. In some experiments, state-selective photofragment ionisation was performed by introducing a second laser counter-propagated with the excimer. The second harmonic of a tunable pulsed dye laser (pulse energies $\sim 50\,\mu$J) was used to ionise some of the $^2D_{5/2}$ excited state Au atomic fragments in a (1 + 1) REMPI scheme, *via* the $(5/2, 1)^\circ_{3/2} \leftarrow {}^2D_{5/2}$ transition. The wavelength of the dye laser was tuned around the atomic transition, centred at 264.277 nm. This was necessary to cover the whole Doppler profile of the fragments, since the wavelength of the REMPI transition is dependent on the component of the atom's velocity in the direction of the laser beam.

In the second experiment, the same dye laser second harmonic was used to photodissociate and photoionise the Au_2. The beam was focused at the centre of the molecular beam, with the electric vector of the beam parallel to the plane of the detector. Ionisation spectra of the Au_2 were recorded by operating in time-of-flight mode and scanning the dye laser between $35400 - 37200\,\text{cm}^{-1}$. Velocity map images were recorded across this region. Pulse energies of up to $480\,\mu$J were used, though this was reduced to *ca.* $20\,\mu$J at $35500\,\text{cm}^{-1}$ at the edge of the laser dye curve.

4.5 VUV photodissociation of Au_2

4.5.1 One-colour images

When the Au atoms are imaged in the single-colour experiment, in which the molecular beam is crossed only by the 157 nm excimer beam, six distinct rings are observed in addition to the central bright spot due to atomic gold produced by the cluster source (Figure 4.4). The right half of the Figure 4.4 is the image reconstructed by polar onion peeling, from which the kinetic energy of the fragments were calculated using the fragment ion time-of-flight and distance from the centre of the image.

The integrated intensity of the rings is given in the TKER spectrum, Figure 4.5. An energy balance calculation (Equation 4.1) was performed using the excimer photon energy, $h\nu$, the ground state dissociation energy of Au_2, $D_0^0 = 2.306(5)\,eV$[245] and the energies of the atomic states of gold taken from the NIST atomic levels database.[246] This gives the internal energies of the detected fragment and cofragment, allowing the peaks to be assigned to the six highest-energy channels accessible by single-photon dissociation of Au_2 $X\,0_g^+$ at 157 nm, identified as channels A–F in Table 4.1.

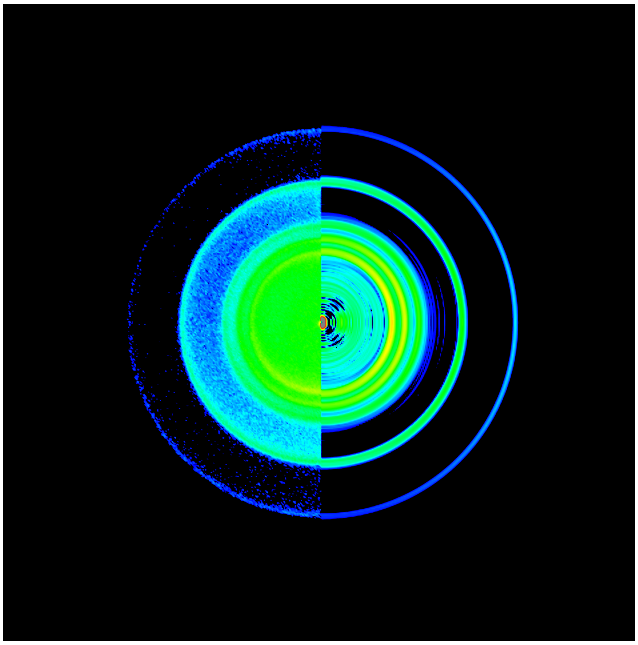


Figure 4.4: Velocity map image of Au_2 dissociation at 157 nm, clearly showing five dissociation channels. A sixth (channel F) is too faint to be visible on this scale. The raw image is shown on the left, and the reconstructed image on the right.

Table 4.1: Energetically accessible Au atom product channels following 157 nm photolysis of Au_2.

Product Channel	**TKER / cm^{-1}**	**Au fragment quantum states**
A	1991	$^2D_{3/2}\left[5d^9 6s^2\right] + {}^2D_{3/2}\left[5d^9 6s^2\right]$
B	2698	$^2S_{1/2}\left[5d^{10}6s\right] + (5/2,0)^\circ_{3/2}\left[5d^9\left(^2D_{5/2}\right)6s6p\left(^3P^\circ_0\right)\right]$
C	3687	$^2S_{1/2}\left[5d^{10}6s\right] + {}^2P^\circ_{3/2}\left[5d^{10}6p\right]$
D	7502	$^2S_{1/2}\left[5d^{10}6s\right] + {}^2P^\circ_{1/2}\left[5d^{10}6p\right]$
E	14264	$^2D_{5/2}\left[5d^9 6s^2\right] + {}^2D_{3/2}\left[5d^9 6s^2\right]$
F	23426	$^2S_{1/2}\left[5d^{10}6s\right] + {}^2D_{3/2}\left[5d^9 6s^2\right]$
G	26538	$^2D_{5/2}\left[5d^9 6s^2\right] + {}^2D_{5/2}\left[5d^9 6s^2\right]$
H	35700	$^2S_{1/2}\left[5d^{10}6s\right] + {}^2D_{5/2}\left[5d^9 6s^2\right]$
I	44861	$^2S_{1/2}\left[5d^{10}6s\right] + {}^2S_{1/2}\left[5d^{10}6s\right]$

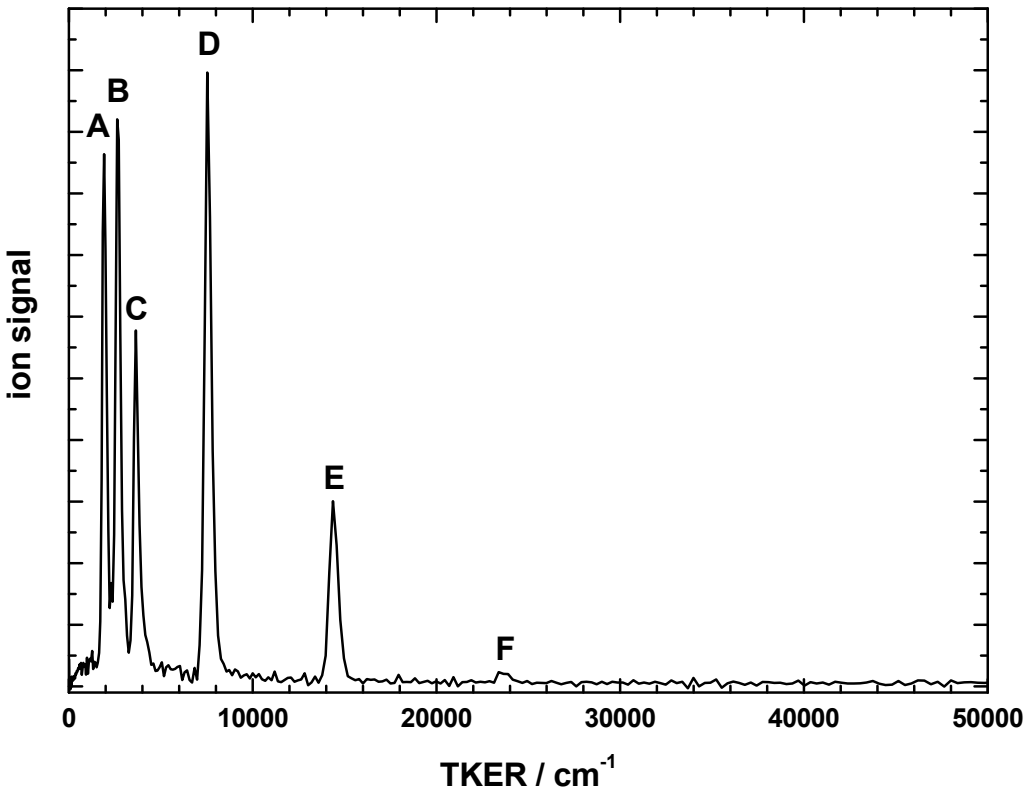


Figure 4.5: Total kinetic energy release (TKER) spectrum of the gold atom fragments after Au_2 dissociation at 157 nm.

The three dissociation channels not observed, G–I, involve combinations of the ground and first excited states of the gold atom. These are the only two Au states which cannot be ionised by a single 157 nm photon. There is evidence of channel G in the two-colour experiments to be discussed in Section 4.5.2, implying that its absence in the one-colour images is simply due to the lower ionisation efficiency at 157 nm.

Of the six channels which can be single-photon ionised, only B-D have an allowed transition to one of the accessible states of Au^+, which has a $^1S(5d^{10})$ ground state and two low-lying (5/2, 1/2) states with configuration $5d^9(^2D_{5/2})6s$. A, E and F involve combinations of the Au $^2S_{1/2}(5d^{10}6s)$ state, which is too low in energy to be ionised by a single photon, and the $^2D(5d^96s)$ states, which can only be ionised to the ground state of the ion through a formally two-electron process. This may reduce the apparent intensity

of these channels relative to B-D, since the ionisation process is formally forbidden.

4.5.2 Two-colour images

To confirm the assignments listed in Table 4.1, a second ionisation laser was introduced, tuned to the Au $(5/2,1)^{\circ}_{3/2} \leftarrow {}^2D_{5/2}$ transition. This should photoionise Au $^2D_{5/2}$ in a $(1+1)$ REMPI scheme, enhancing the ring labelled E above the other channels. The image presented in Figure 4.6, recorded by scanning the ionisation laser over the $^2D_{5/2}$ Doppler profile, shows that this is indeed the case: the same six rings are observed but E is now the brightest ring in the image. The central spot, due to atoms with no off-axis kinetic energy, is also enhanced, suggesting that some metastable Au $^2D_{5/2}$ atoms are present in the molecular beam.

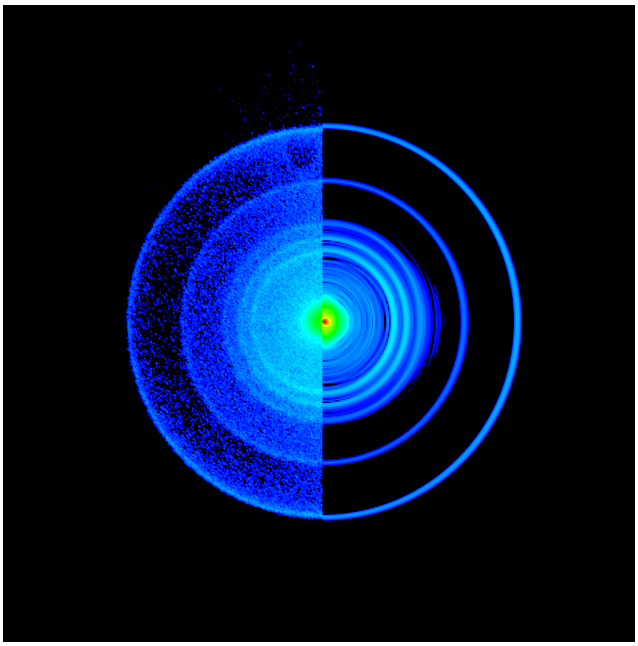


Figure 4.6: Velocity map image of Au_2 dissociation at 157 nm. The introduction of a tunable dye laser tuned to the Au $(5/2,1)^{\circ}_{3/2} \leftarrow {}^2D_{5/2}$ transition enhances the signal from the centre (due to the molecular beam) and channel E.

The TKER spectrum, Figure 4.7, demonstrates the enhancement of channel E and the central spot. In addition to the original rings, a seventh is present with a TKER of $26800 \pm 300\,\mathrm{cm}^{-1}$, corresponding to the channel G: $^2D_{5/2} + {}^2D_{5/2}$, but this is weak even though both of this channel's products can be ionised on-resonance. There is no

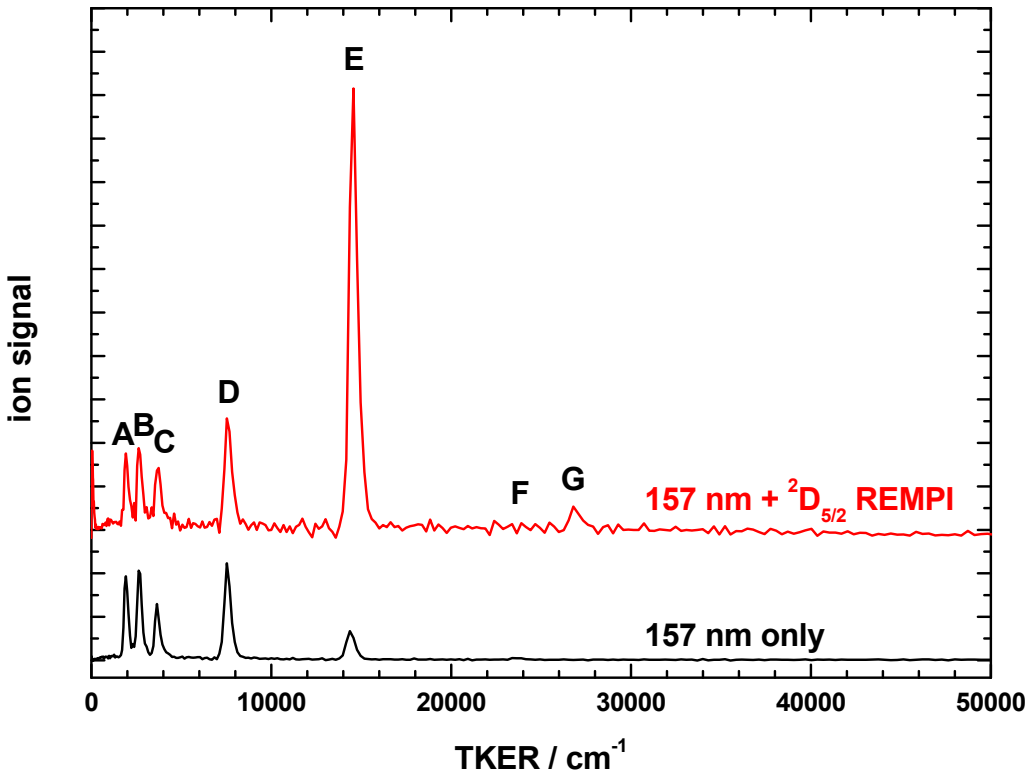


Figure 4.7: Total kinetic energy release (TKER) spectrum of the gold atom fragments after Au_2 dissociation at 157 nm. The lower trace is the TKER spectrum recorded using 157 nm for both photolysis and photoionisation (shown in more detail in Figure 4.5). In the upper trace, upon the introduction of a tunable dye laser tuned to the Au $(5/2, 1)^\circ_{3/2} \leftarrow {}^2D_{5/2}$ transition, channel E is enhanced and a further channel G is observed.

evidence of channel H, which also includes a $^2D_{5/2}$ product.

The spectroscopy of Au_2 in this region has not been previously studied, so the upper state (or states) involved in the dissociation is unknown. Balasubramanian's CASSCF calculations of excited Au_2 states only considered those up to $\sim 50000\,\mathrm{cm}^{-1}$ arising from the Au $^2S_{1/2}$ and ^2D states,[247] but even this predicts a wealth of molecular states with significant configuration mixing. The electronic structure in the VUV region, in which there are many separated atom limits which could give rise to multiple molecular states, may be more complex still.

4.5.3 Conclusions

Au_2 has been studied by photodissociation at 157 nm and imaging of the subsequent fragments by VMI. Dissociation has been observed into seven of the nine energetically accessible channels. Selectively ionising the $^2D_{5/2}$ state of the Au atom confirms the assignment of these channels as combinations of excited states of Au. Photodissociation favours the production of the higher energy channels, closer to the excitation energy. The Au_2 excited state accessed by the 157 nm excitation lies over 20000 cm^{-1} higher than the molecular states which have been characterised experimentally (Figure 4.8),

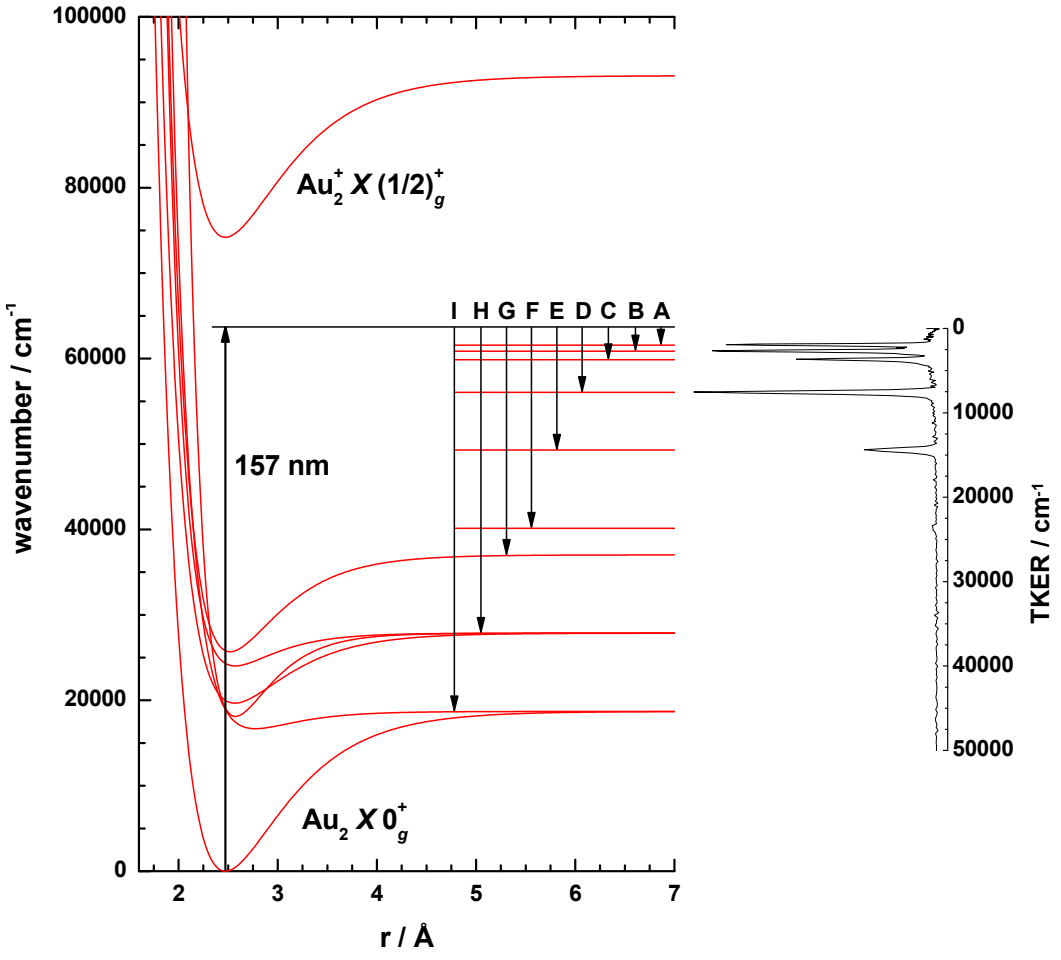


Figure 4.8: Low-lying molecular states and dissociation limits of Au_2, with the one-colour TKER spectrum to show the photodissociation fragments observed in this VMI experiment. The potential energy curves are plotted using constants from work by Bishea and Morse.[67] The dissociation channels are labelled A-I following the definitions given in Table 4.1.

and where no calculations have been performed. The gold atomic products formed by the predissociation of this state provide some information on the nature of the curve crossings in this region with which to compare future excited state calculations.

4.6 Near-UV photodissociation of Au_2

The five Au_2 excited states observed in the visible spectral region by LIF and REMPI show clear vibrational progressions.[67] Figure 4.9 shows three of these progressions, recorded by $(1+1')$ REMPI using excitation by an optical parametric oscillator (OPO) followed by ionisation by the F_2 excimer laser at 157 nm. The $a\,^3\Sigma_{1u}^+ - X\,0_g^+$, $A'\,1_u - X\,0_g^+$ and $A\,0_u - X\,0_g^+$ progressions from $v'' = 0$ and several hot bands can be easily identified in the spectrum. This spectrum is also observed in the Au^+ channel, but images of this photodissociation product show only broad, unresolved TKER peaks which are masked by the TKER peaks present due to 157 nm photodissociation.

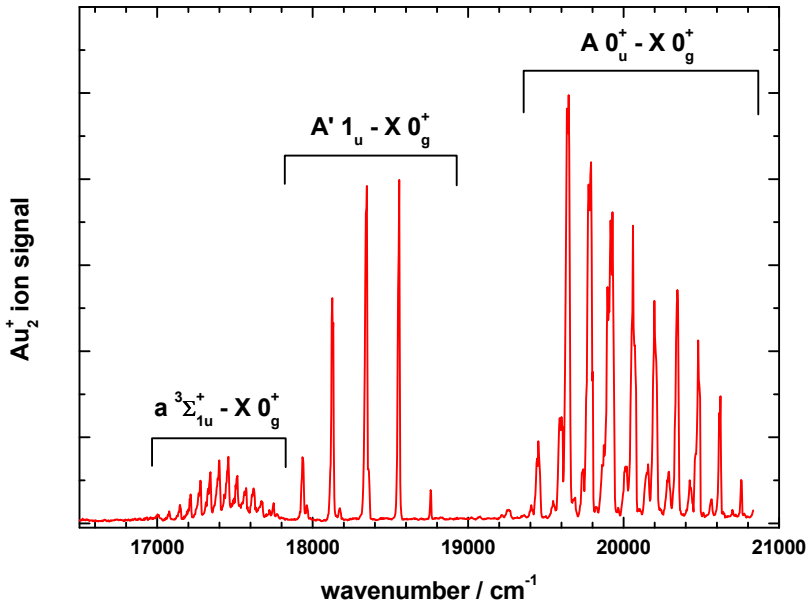


Figure 4.9: $(1+1')$ REMPI spectrum of Au_2, showing three vibrational progressions previously assigned by Bishea and Morse.[67]

Au_2 photodissociation is also observed in the near-UV spectral region, within the range of the tunable dye laser which can be used to study the evolution of the Au fragment images with changing wavelength. Between 35400 and 37200 cm^{-1}, ground state Au_2 can only be ionised in a three-photon process, and the two-photon ionisation threshold of the Au atom occurs at the high-wavelength end of this region, at 37204.44 cm^{-1}.[246] Nonetheless, Au_2 exhibits a dense spectrum in this region which correlates with large enhancements in the Au atom channel, suggesting that the Au enhancement is due to Au_2 photodissociation. This observation is confirmed by photofragment imaging, which also provides a wealth of information on the photodissociation process occurring at the two-photon level. This process is determined to be neutral Au_2 photodissociation followed by ionisation of the atomic products.

4.6.1 Au_2 spectroscopy

The full mass spectrum was recorded at every wavelength, so that the spectra for all species were measured simultaneously. Two (1+1) REMPI transitions in the Au atom were used to calibrate the spectra: $^2P^\circ_{1/2} \leftarrow {}^2S_{1/2}$ at 37358.991 cm^{-1} and $(5/2, 1)^\circ_{3/2} \leftarrow {}^2D_{5/2}$ at 37846.256 cm^{-1}.

The signal observed in the Au channel changes dramatically with cluster source conditions. When the conditions are optimised for Au atoms only, with almost no cluster production, the only peaks in the Au spectrum arise from atomic photoionisation (Figure 4.10). These lines converge towards the two-photon ionisation energy of Au, identifying them as $(2+1)$ REMPI transitions *via* atomic Rydberg states: states in which an electron has been excited to an orbital with high principle quantum number n. Rydberg orbitals are hydrogenic, approximating an electron interacting with the singly charged ion core, and so their energies follow the Rydberg formula (Equation 4.9).

$$E_n = E_I - \frac{R_y}{(n-\delta)^2} \tag{4.9}$$

where E_I is the ionisation energy and R_y is the Rydberg constant of the species concerned. Originally conceived as an empirical fitting factor, δ is now interpreted as the phase shift ($\pi\delta$ radians) of the Rydberg electron wavefunction at the boundary between the outer region of the atom and the ion core, due to the deviation from a pure Coulomb potential.[248] The value of δ is larger for orbitals with lower angular momentum because of the larger probability density nearer the core.

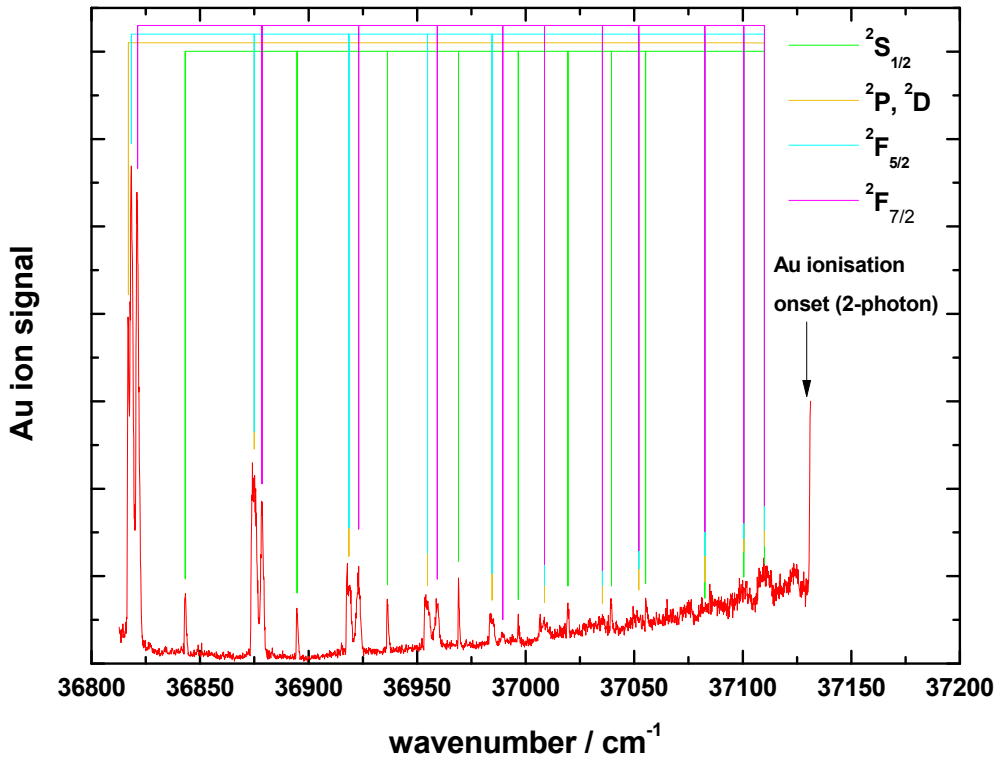


Figure 4.10: Rydberg series observed in the near-UV spectrum of the Au atom under non-clustering conditions. All lines are $(2+1)$ REMPI transitions originating from the ground $^2S_{1/2}$ state. Assignment combs mark the excited atomic states.

The lines in this spectrum are assigned as (2+1) REMPI transitions from the Au ground $^2S_{1/2}$ state through Rydberg levels approaching the first ionisation limit of the Au atom, based on the energies and quantum defects previously assigned to the *S*, *P*, *D* and *F*

Rydberg series.[249–253] The onset of ionisation is observed at 37130.4 cm^{-1}, which is below the literature value due to field ionisation in the VMI electric fields.

When the cluster source conditions are modified to produce proportionally more of the larger clusters, the Rydberg lines are still identifiable, but there are many more new features in the spectrum which appear to show broad vibrational structure (Figure 4.11). The same structure, albeit much weaker, is also seen in the Au_2 channel but not in any of the larger clusters. This implies that the Au_2 is being resonantly ionised through an excited state which can also dissociate into Au atoms, or that the Au_2^+ dissociates to give Au^+.

The density of vibrational bands is much higher than that of the spectrum in the visible region (Figure 4.9), but some interpretation is possible even without the aid of the VMI images to be discussed later in Section 4.6.2. Although the spectrum is not rotationally resolved (due to the small rotational constant of Au_2), many of the peaks below 36000 cm^{-1} have a broadened structure which rises to higher wavenumber before an abrupt fall in intensity. Such a peak shape is expected from a band with $B''_v > B'_v$, which would produce rotational bands with band-heads in the higher wavenumber branches.

These bands converge as the wavelength increases, suggesting that they arise from a vibrational progression of an excited state close to its dissociation limit. In this region there is one dissociation limit at the one-photon level, and four at the two-photon level. Their positions, summarised in Table 4.2 and Figure 4.12, can be calculated from the energies of the atomic states[246] and the dissociation energy of ground state Au_2 (18599 ± 40 cm^{-1}).[237]

The vibrational lines appear to be converging towards one of these limits: the $^2S_{1/2}\left[5d^{10}6s\right]+$ $^2S_{1/2}\left[5d^{10}7s\right]$ limit, which is present in the spectrum as a broad unresolved feature. There is a similar feature, ca. 100 cm^{-1} lower in wavenumber (corresponding to a 200 cm^{-1} spacing at the 2-photon level), which may also be due this dissociation limit,

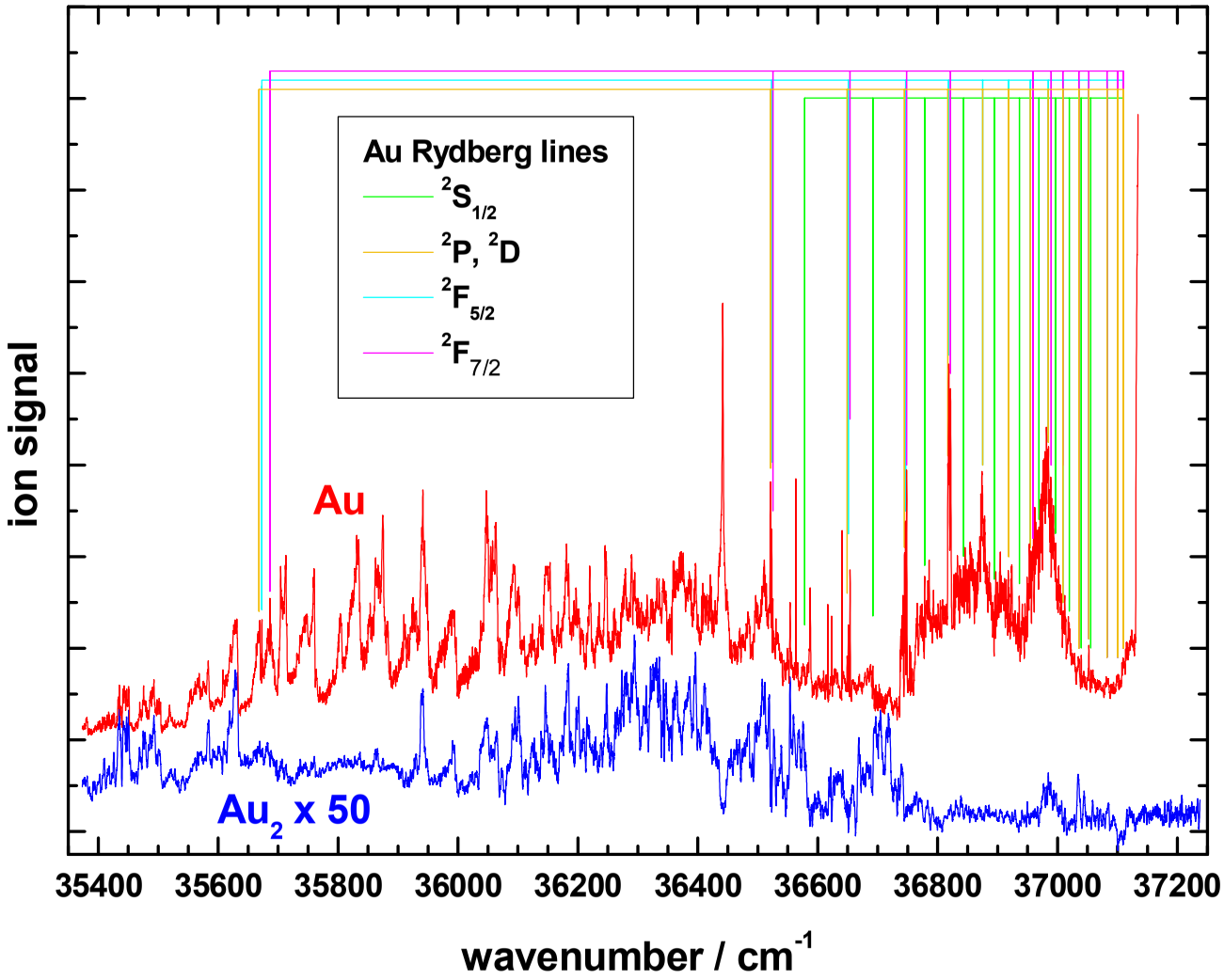


Figure 4.11: Near-UV spectrum of Au and Au_2, leading up to the two-photon ionisation threshold of the Au atom. Most of the narrowest features can be assigned as resonant ionisation of Au through a Rydberg level in a $(2+1)$ REMPI scheme.

Table 4.2: Dissociation limits of Au_2 within the region of the near-UV spectrum. The uncertainty in the dissociation limit wavenumber arises from the value of D_0^0 used in the calculation.

Correlated atomic states	**no. of photons**	**wavenumber / cm^{-1}**
$^2D_{5/2}\left[5d^9 6s^2\right] + {}^2D_{3/2}\left[5d^9 6s^2\right]$	1	36921 ± 40
$^2S_{1/2}\left[5d^{10}6s\right] + (5/2,2)^\circ_{3/2}\left[5d^9 6s6p\right]$	2	35898 ± 20
$^2S_{1/2}\left[5d^{10}6s\right] + {}^2S_{1/2}\left[5d^{10}7s\right]$	2	36542 ± 20
$^2D_{5/2}\left[5d^9 6s^2\right] + (5/2,1)^\circ_{7/2}\left[5d^9 6s6p\right]$	2	36649 ± 20
$^2D_{5/2}\left[5d^9 6s^2\right] + (5/2,1)^\circ_{5/2}\left[5d^9 6s6p\right]$	2	36968 ± 20

arising from Au_2 in the $v'' = 1$ level. We know from the 157 nm photodissociation that vibrationally excited Au_2 *is* present in the molecular beam, so it is unsurprising to observe transitions out of this level.

The positions of the band heads in the Au spectrum can be fitted to two vibrational progressions, assuming a Morse potential for the upper state. Figure 4.12 identifies the lines included in these fits. Since the origin band is not observed, v' is unknown for these bands, but the fits return values for the convergence as 36416 ± 45 and $36535 \pm 48\,\text{cm}^{-1}$. Both of these are consistent with bands converging to the $^2S_{1/2}\left[5d^{10}6s\right] + {}^2S_{1/2}\left[5d^{10}7s\right]$ limit from the $v'' = 1$ and $v'' = 0$ levels of ground state Au_2.

The interaction between the Au $6s$ and $7s$ atomic orbitals should produce a bound 0_g^+ state, which is accessible from the ground 0_g^+ state following the two-photon selection rules. To our knowledge, the properties of this state have not been calculated, but the equilibrium bond length of this state is expected to be significantly longer than that of the ground state, which is formed from the $6s + 6s$ interaction. The difference in r_e would explain why the Franck-Condon factors favour these transitions to very high-lying vibrational levels of the excited state.

There is no evidence of either the one-photon convergence limit, or the two-photon limits at $36921\,\text{cm}^{-1}$ and $36649\,\text{cm}^{-1}$. There are, however, broad features corresponding to the $^2D_{5/2}\left[5d^9 6s^2\right] + (5/2,1)^\circ_{5/2}\left[5d^9 6s6p\right]$ threshold, both from $v'' = 0$ and $v'' = 1$. Unfortunately, these cannot be vibrationally resolved, but they provide the

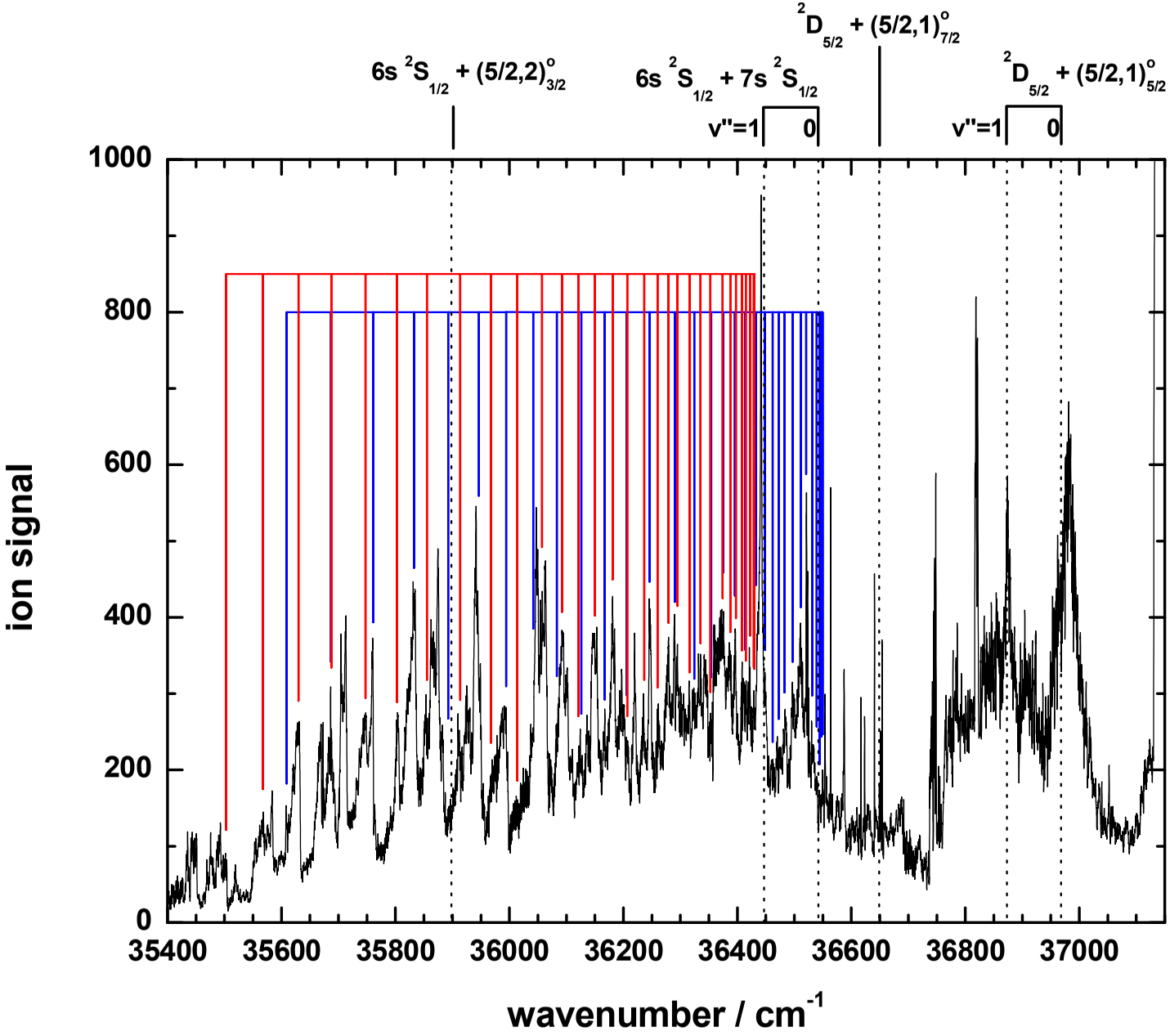


Figure 4.12: Lines in the Au spectrum converge towards the two-photon dissociation limit of Au_2 at 36542 cm^{-1}, of a state correlated with the atomic states $6s^2S_{1/2} + 7s^2S_{1/2}$. A convergence at 36447 cm^{-1} arises from vibrationally excited Au_2. Dissociation limits are also observed for the Au $^2D_{5/2} + (5/2,1)_{5/2}$ states, but cannot be vibrationally resolved.

best explanation for the broad peaks at these wavenumbers.

4.6.2 Au_2 near-UV VMI

The UV spectra suggest that Au_2 photodissociation occurs at the two-photon level. Part of the excess energy will be partitioned into the internal energy of the Au atomic fragments, but any remaining kinetic energy of the fragments should be detectable using velocity map imaging. Recording these images as a function of wavelength should also yield information on the nature of the photodissociation process.

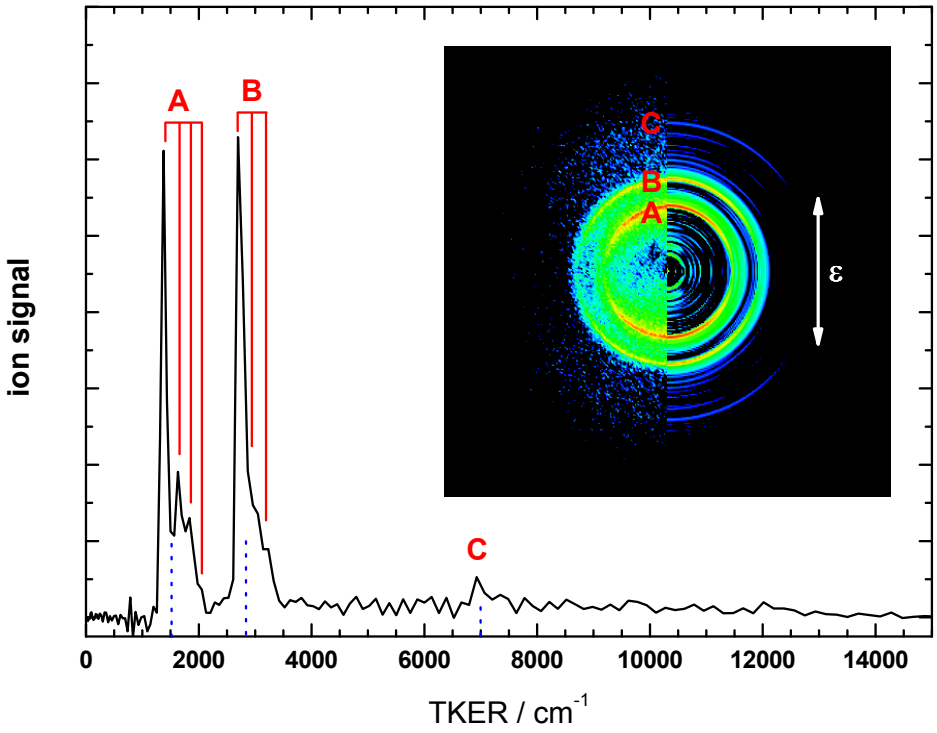


Figure 4.13: TKER spectrum arising from Au_2 photodissociation at 35885.7 cm^{-1}. Peaks A-C can be assigned to three of the energetically available photodissociation channels at the two photon level. A and B show additional structure ~ 200 cm^{-1} to higher TKER, arising from vibrationally hot Au_2. Dashed lines mark the predicted TKER of Au atoms arising from predissociated Au_2. Inset: VMI image used to extract the TKER spectrum, with rings A-C marked. The electric vector polarisation of the laser, $\boldsymbol{\epsilon}$, is marked as an arrow on the image.

The Au images recorded across the spectrum reveal clear rings corresponding to the Au_2 dissociation. Each was inverted using the polar onion peeling method previously

discussed, and the ring radius converted to the total kinetic energy of the co-fragments using the known Au_2 dissociation energy. A typical image is given in Figure 4.13, showing both the raw data and the reconstructed image. Three rings can be clearly identified, all with marked anisotropy. This image was recorded at 35885.7 cm^{-1}, on one of the band-heads leading up to the $6s\,^2S_{1/2} + 7s\,^2S_{1/2}$ dissociation limit. The TKER spectrum extracted from the peeled image is also given. The three rings have a TKER of 1369, 2682 and 6894 cm^{-1}, with the two more intense features showing additional vibrational structure.

The Au^+ in these images could potentially be produced by any of four processes. The first is that observed in 157 nm dissociation: excitation to an excited Au_2 state, followed by predissociation to neutral gold atoms which are then ionised. Alternatively, excited Au_2 could predissociate through an ion pair state, producing a gold cation and anion directly. Two more possibilities exist for dissociation of the Au_2^+ ion: either predissociation of Au_2^+ in an excited state, or photodissociation of Au_2^+. The resulting TKER in each of these processes can be calculated using the known states of Au and Au^+,[246] the electron affinity of Au (2.30863 eV),[254] $D_0^0(Au_2)$,[237] and $D_0^0(Au_2^+)$.[67]

Each of these pathways could produce Au cations with TKER lying within the range of the detector, but only the neutral predissociation path can account for the observed TKER peaks. These calculated kinetic energies are marked on Figure 4.13. The other images recorded across the spectrum can be interpreted in the same way, as two-photon excitation of Au_2 followed by predissociation into neutral Au atoms which are then photoionised. This supports the conclusion of the Au_2 spectroscopy, which is that the Au_2 excitation is a coherent two-photon process.

The additional structure in peaks A and B in Figure 4.13 consists of less intense peaks to higher TKER than the main peak, separated by intervals of ca. 200 cm^{-1}. They cannot be assigned to any of the atom limits following predissociation, but the 200 cm^{-1} spacing

suggests that they arise from a similar excitation from vibrationally excited Au_2, which has a ground state vibrational constant of $190.9\,cm^{-1}$.[238] The hot bands present in the Au_2 spectra are also evidence of vibrationally hot Au_2, and support this assignment of the TKER peaks. By fitting the peaks to a series of Gaussians to find the intensities of each component, and assuming a Boltzmann distribution, the Au_2 temperature is calculated to be $340 \pm 45\,cm^{-1}$. This implies that the gold dimers are being thermalised inside the room-temperature ablation block, and are not substantially cooled by the molecular beam expansion.

Au fragment angular distribution

Further characteristics of the excited state come from the anisotropy of the images. Beta-parameters can be extracted from the images by taking the intensity as a function of angle, and fitting it to the Legendre polynomial expansion. At the two-photon level, Equation 4.4 gives the distribution:

$$\begin{aligned} I(\theta) &= \frac{1+\beta_2 P_2(\cos\theta)+\beta_4 P_4(\cos\theta)}{4\pi} \\ &= \frac{1+\beta_2\left(3\cos^2\theta-1\right)/2+\beta_4\left(35\cos^4\theta-30\cos^2\theta+3\right)/8}{4\pi} \end{aligned} \tag{4.10}$$

Figure 4.14 shows the angular distributions of the three most intense rings in 4.13 together with the fits to Equation 4.10 from which β_2 and β_4 have been determined (Table 4.3). All three values of β_2 are positive and are approximately equal to one, while β_4 varies between -0.1 and -0.2. The limiting values of β calculated by Dixon ($\beta_2 = \frac{20}{7}, \beta_4 = \frac{8}{7}$ in the case of a $0 \rightarrow 0 \rightarrow 0$ transition) are not strictly applicable if the individual rotational lines cannot be resolved, as is the case here due to the small rotational constant of Au_2. Instead, both β values vary across each band.[178] In the case of a $0 \rightarrow 0 \rightarrow 0$ transition, β_2 should always be positive, which is what is observed in this

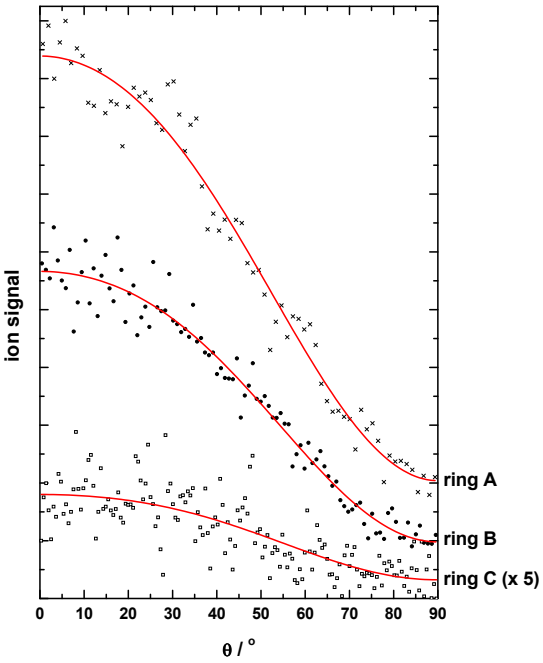


Figure 4.14: Angular distribution of the rings shown in Figure 4.13: all are due to parallel transitions in Au_2, as the fit to the anisotropy (Equation 4.10) gives values of $\beta_2 > 0$ (summarised in Table 4.3). The angle θ is the angle between the laser's electric vector $\boldsymbol{\epsilon}$ and the velocity vector of the Au atom fragment.

image, implying a parallel transition.

The images recorded across the spectrum have widely varying β parameters. While there is no clear trend, the values of β_2 typically fall in the range 0.2 to 1.5. This implies that all of the Au_2 transitions across the spectrum are parallel. Since the ground state is of symmetry 0_g^+, a parallel two-photon transition must be to another 0_g^+ state.

Table 4.3: Anisotropy parameters fitted to the fragment distribution shown in Figure 4.14.

ring	β_2	β_4
A	1.07 ± 0.03	-0.10 ± 0.03
B	1.18 ± 0.03	-0.15 ± 0.03
C	1.2 ± 0.1	-0.17 ± 0.09

In Section 4.6.1, Au_2 transitions were identified as transitions to a state correlated to the Au $^2S_{1/2}\left[5d^{10}6s\right] + {}^2S_{1/2}\left[5d^{10}7s\right]$ separated atom limit. These atomic states can combine to generate six molecular states (following the Hund's case (c) formalism): $0_g^+, 0_u^+, 0_g^-, 0_u^-, 1_g$ and 1_u. Similarly, the other dissociation limit observed, $^2D_{5/2}\left[5d^9 6s^2\right]+$

$(5/2,1)^{\circ}_{5/2}\left[5d^9 6s6p\right]$, produces numerous molecular states, including several 0^+_g states. Parallel transitions to these 0^+_g states can account for the observed Au_2 spectra and the positive β_2 parameters of the Au fragments.

For predissociation to occur, these states must be crossed by others of the correct symmetry to perturb the 0^+_g states. The selection rules for this predissociation are:[255]

$$\begin{gathered} \Delta J = 0 \\ + \nleftrightarrow - \\ s \nleftrightarrow a \\ \Delta\Omega = 0, \pm 1 \end{gathered} \tag{4.11}$$

Following these selection rules, predissociation from a 0^+_g state can occur to another 0^+_g state or a 1_g state. All of the separated atom limits in this region can combine to form these states, so there will be many such crossings which could cause the observed predissociation.

4.6.3 VMI images across the UV spectrum

Images have been recorded at 54 features in the spectral region 35550 to 36910 cm^{-1}. Each has been analysed in the same way as shown in Section 4.6.2, and the results are shown in Figure 4.15. Each circle represents a TKER peak, with intensity proportional to the circle's area.

There are 22 energetically accessible Au atom fragments, of which 16 are within the detectable range of the VMI instrument. These are marked on the figure as dashed lines with a gradient of 2, because this is a two-photon process. Most of the energetically accessible dissociation products are observed in the Au fragment images: 13 of the 16 detectable pathways. Clearly, these predicted TKER values are an excellent match to

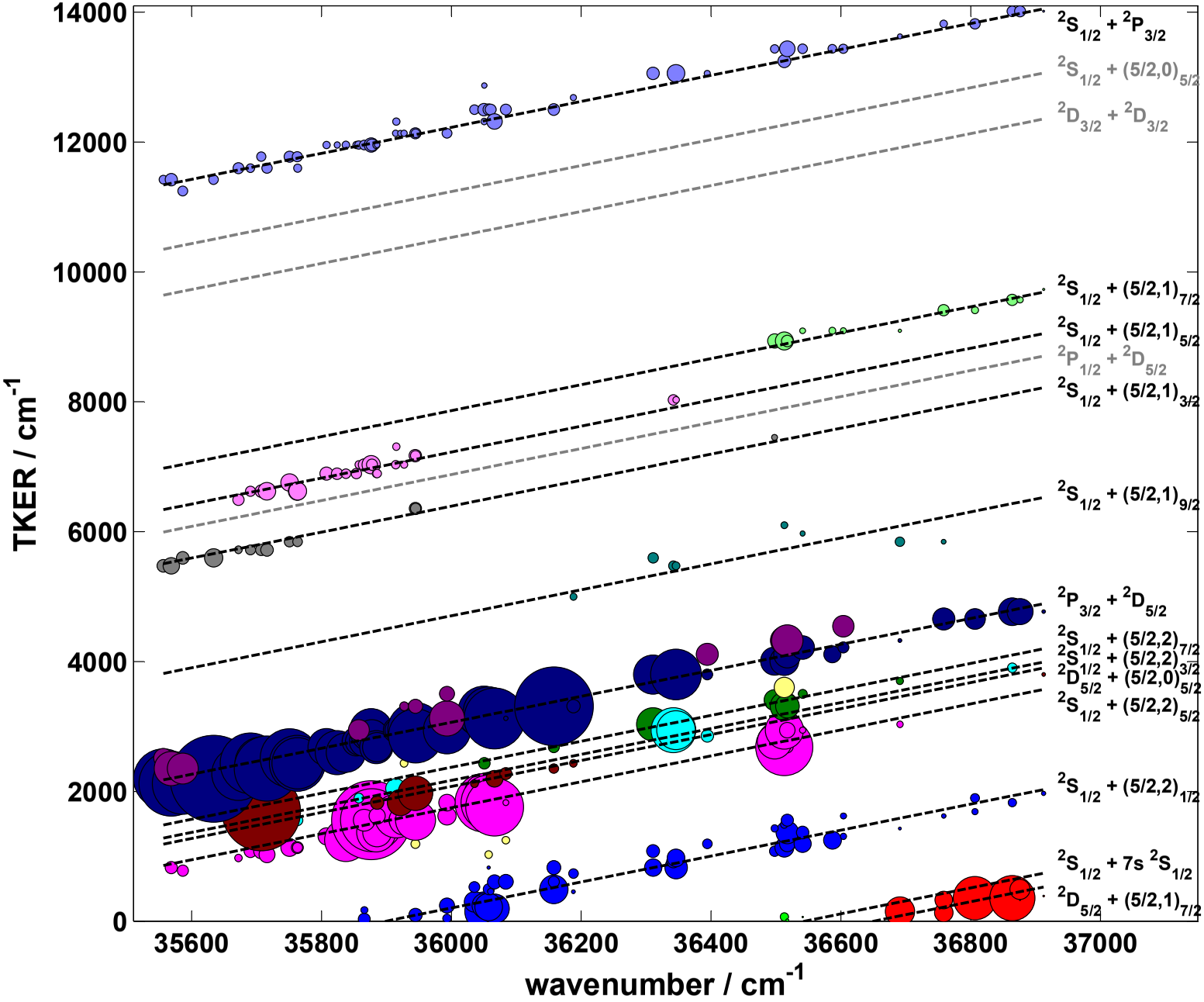


Figure 4.15: Summary of TKER spectra extracted from the Au_2 photodissociation images. Each TKER peak is marked by a circle whose area is proportional to the TKER peak intensity. Most peaks lie close to the predicted TKER for two-photon dissociation of Au_2, marked by solid lines. Grey dashed lines indicate atomic fragments which are energetically accessible but not observed experimentally.

the observed TKER peaks, confirming the earlier assignment of a two-photon excitation followed by predissociation.

Just as observed in the 157 nm photodissociation (see Section 4.5), higher-energy product channels are apparently favoured, since the low-TKER peaks are generally the most intense. The $^2D_{1/2} + {}^2P_{3/2}$ product pair, in particular, appears as an intense peak in almost every recorded image. The $^2S_{1/2} + {}^2P_{3/2}$ peak is similarly consistent across the spectrum, though with much less intensity.

The three highest-energy product channels appear only when the total photon energy exceeds the energetic threshold to their production. Other channels are only present for part of the spectrum, such as the $^2S_{1/2} + (5/2, 1)_{7/2}$, which is only present above around 36500 cm^{-1}. The wavenumber at which these channels open must be related to the opening of new predissociation channels, but the enormous density of molecular states precludes a definitive assignment of the curve crossings involved at this time.

4.7 Conclusions and future work

Diatomic gold has been photodissociated by UV in a single-photon dissociation at 157 nm, and in a two-photon process in the near-UV between 35500 and 37200 cm^{-1}. In both cases, the photofragments are neutral Au atoms, and their kinetic energies can be determined by VMI and used to definitively assign the quantum states of the initial Au_2 and the Au atomic fragments. The VMI image wavelength-dependence and the product anisotropy aided the interpretation of the Au_2 spectrum in the UV: Au_2 is resonantly ionised in a $(2 + 1)$ REMPI scheme through several excited states of 0_g^+ symmetry close to their dissociation limits. These states can also predissociate, forming the Au atomic products observed both spectroscopically and using VMI. Furthermore, these studies demonstrate the feasibility of performing VMI experiments on small metal clusters, and complements the spectroscopy by providing information on the dynamics and products

of the photodissociation process.

Understanding the openings of the Au photofragment channels requires detailed excited state calculations of Au_2. Such calculations are difficult because of the large number of electrons in gold atoms, which must be treated relativistically. Studies like this are, however, essential in testing calculations on the nature of excited states and their curve crossings.

Chapter 5

Infrared spectroscopy and reactivity of N_2O on rhodium clusters [†]

5.1 Introduction

Infrared multiple photon dissociation spectroscopy (IR-MPD) has been applied to small rhodium clusters with nitrous oxide molecules adsorbed on their surfaces. Their mid- and far-infrared spectra were recorded using action spectroscopy, aided by argon tagging, and the results compared to the spectra predicted by density functional calculations in order to determine their structures. Heating the cluster *via* infrared absorption is observed to induce reactions of the N_2O on the surface of the cluster.

These experiments were all performed at the FELIX (Free Electron Laser for Infrared eXperiments) facility in the Netherlands,[257] as part of a larger study of bare rhodium

[†]Some of the results in this chapter have been published as *Infrared Induced Reactivity on the Surface of Isolated Size-Selected Clusters: Dissociation of N_2O on Rhodium Clusters*.[256]

clusters and their oxides. The infrared spectra of the bare clusters have been published in the Journal of Chemical Physics.[258,259] The work was performed in collaboration with the Fielicke and Meijer group from the Fritz-Haber-Institut der Max-Planck-Gesellschaft in Berlin, whose experimental apparatus was used. I was involved in running the spectroscopy experiments, and I have analysed all of the $Rh_nN_2O^+$ data presented here.

5.2 Cluster structure determination by IR-MPD

Infrared spectroscopy is a powerful tool in structure determination, because the normal mode frequencies of a molecule are a signature of its underlying structure. Recording vibrational spectra of metal clusters is, however, extremely challenging for a number of reasons that have been discussed earlier: laser ablation cluster sources typically produce $\sim 10^6$ clusters, and generate a wide distribution of different sizes. An additional problem is the very low infrared cross-section of metal clusters, due to their small dipole moments. Direct absorption techniques are not sensitive enough to detect infrared absorption by these species, and so action spectroscopy techniques which take advantage of the high sensitivity of mass spectroscopic detection must be employed instead. Since mass spectroscopy is extremely sensitive, it can be used to detect an absorption which causes molecular fragmentation, and hence alters the mass spectrum, as shown schematically in Figure 5.1.

Several photons may be required to overcome the binding energy of the photodissociation fragments. In these cases, infrared photon absorption is usually sequential, with intramolecular vibrational redistribution (IVR) transferring the energy to one of the many other normal modes of the cluster between successive photon absorption by the resonant mode. For this reason, the technique is usually referred to as infrared *multiple* photon dissociation (IR-MPD), to distinguish it from a coherent multiphoton process. IR-MPD is very efficient because of the IVR step: each photon is absorbed by the vibra-

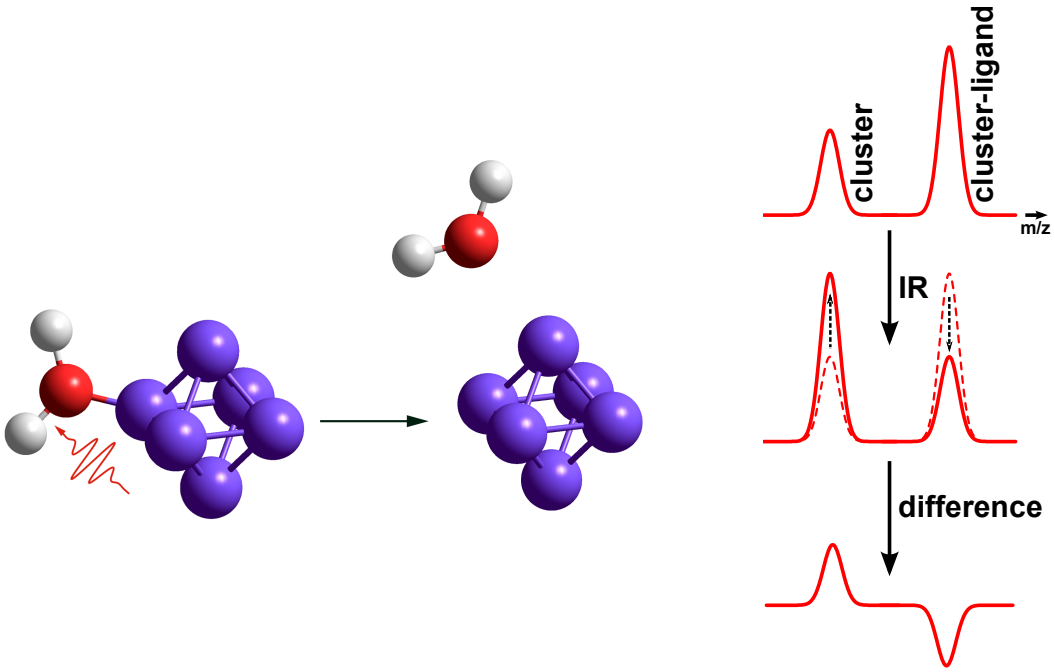


Figure 5.1: Left: infrared photodissociation. Absorption is measured by indirectly monitoring the changing relative abundance of each species mass-spectroscopically when the infrared source is introduced. Right: schematic of the mass spectrum for this process. When the cluster fragments, the intensity of its mass spectrum peak is reduced, and there is a corresponding increase in signal for the fragment peak.

tional fundamental, so the IR is always on-resonance, which would not be the case in a multiphoton process because of anharmonicity.

5.2.1 Rare gas tagging

The bare metal clusters themselves have very low-frequency infrared modes, typically below $500\,\mathrm{cm}^{-1}$ ($\lambda > 20\,\mu\mathrm{m}$) in the far-infrared. The energy required to fragment the clusters is usually considerably higher than this. For example the dissociation energy of cationic clusters is on the order of $20000\,\mathrm{cm}^{-1}$ for gold,[260] and $25000\,\mathrm{cm}^{-1}$ for silver.[261] To make infrared photodissociation feasible for these species, a weak bond must be introduced which does not significantly perturb the structure or the spectrum of the cluster.

Based on the inert messenger technique developed for metal cluster vibrational spec-

troscopy by Duncan and co-workers,[262] IR dissociation was applied to the far-infrared modes of metal clusters by the Fielicke and Meijer group in 2004 by clustering vanadium in the presence of argon, generating some clusters with weakly-bound argon atoms.[18] When the infrared source is resonant with a cluster vibrational mode, infrared is absorbed, heating the cluster. Intramolecular vibrational redistribution (IVR) will eventually transfer the absorbed energy into the cluster-argon bond, dissociating it to produce a bare cluster and an argon atom. The infrared absorption event can then be inferred from the change in the mass spectrum upon IR irradiation.

Since each metal cluster has many plausible isomers, interpretation of the results requires comparison with predicted spectra from quantum chemical calculations. Multi-reference calculations are computationally expensive and are feasible only for the very smallest clusters.[108] Instead, density functional theory (DFT) is often chosen to efficiently treat the large number of electrons in transition metals.[111] Several isomers of each cluster are optimised using DFT, which also provides the vibrational normal modes with which to compare the experimental infrared spectrum.

The Fielicke and Meijer group have successfully applied this technique to many transition metal systems. Different charge states can be studied by using pulsed extraction voltages to collect charged clusters, or photoionising neutral clusters.[55] The argon atom is generally found to have a very small effect on the absorption frequencies – less than $10\,\mathrm{cm}^{-1}$ in the case of small silver clusters.[53] In some cases, additional argon atoms break the cluster symmetry, introducing new IR-active modes and affecting the relative intensity of far-IR bands, but this typically only occurs for small clusters with $n \leq 5$.[54]

5.2.2 IR-MPD of decorated clusters

IR-MPD can also be applied to small molecules adsorbed on the surface of metal clusters. The binding energies of these molecules is often sufficiently small, and their normal

modes are sufficiently high in energy, that they can be used as their own absorption messenger: when they absorb a photon, IVR transfers the energy into the metal-ligand bond, which then dissociates. The infrared spectrum of the adsorbed species can then be compared with its gas-phase spectrum to deduce the nature of the bonding to the cluster.

The infrared spectrum of adsorbed CO has been recorded on many clusters in several charge states, because the CO stretching frequency is strongly dependent on the nature of its binding to the metal surface.[263] The nitric oxide stretching frequency is similarly sensitive, and shows odd-even oscillations on gold clusters, due to their electronic shell structure.[264] The same technique has been applied to small organic adsorbates,[265,266] and adsorbed water.[49] Absorption frequencies can distinguish molecularly chemisorbed H_2 from dissociated H_2 on cluster surfaces.[267] In this case, the desorbing species is H_2 even when it is fully dissociated on the surface, suggesting that the hydrogen atoms to recombine on the surface when the cluster is heated by infrared excitation.

5.2.3 Free electron lasers

The range of cluster systems that can easily be studied using IR-MPD is limited by the lack of lab-based infrared sources which are tunable and sufficiently intense for multiple-photon dissociation. Optical parametric oscillators are available from the near-UV down to the mid-infrared, but they cannot yet operate in the region of the metal-metal cluster modes. Instead, the infrared source used in most of the studies referenced in Sections 5.2.1 and 5.2.2 is a free electron laser, whose lasing medium is a beam of electrons oscillating in a magnetic field, rather than being bound within a molecule or crystal as in a conventional laser.[268]

Figure 5.2 shows a schematic of a free electron laser. An electron beam is accelerated to a relativistic velocity in a linear accelerator and then guided into a series of permanent

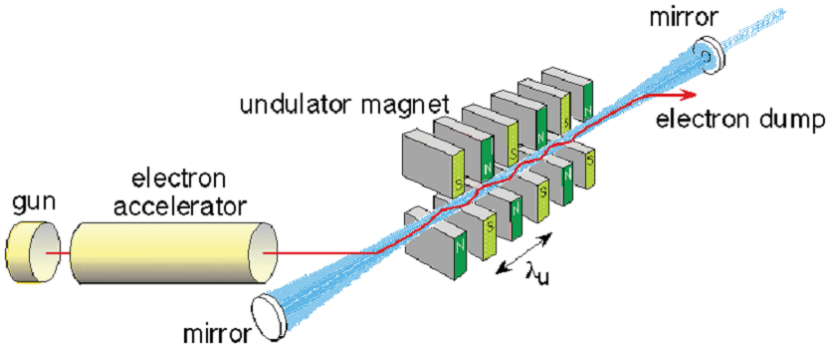


Figure 5.2: Schematic of a free-electron laser. The electron beam is guided into the undulator, which consists of pairs of permanent magnets. The magnetic field causes the electrons to oscillate and emit radiation at a resonant frequency defined by the undulator magnet. Diagram taken from work by Meijer and coworkers.[269]

magnets called an undulator. The pairs of magnets have alternating polarities, producing a periodic magnetic field through which the electron beam travels in a sine curve. The acceleration of the electrons causes them to emit radiation parallel to the beam, Doppler shifted to higher frequencies by the high electron velocity. Mirrors at either end of the undulator form a laser cavity which traps the emitted light. The trapped field perturbs the paths of new electrons so that the electron motion is in phase with the trapped light, causing these electrons to emit coherently with the light already in the cavity. A small fraction of this monochromatic, coherent light is coupled out of the cavity by a small hole in one of the end mirrors.

The oscillation frequency can be modified by changing either the electron beam velocity or the magnetic field strength. In practice, this is achieved by adjusting the spacing between the rows of undulator magnets. Since the spacing is continuously tunable, the emitted radiation is also tunable across a wide range of wavelengths.

FELIX

FELIX (the Free Electron Laser for Infrared eXperiments) is an infrared free electron laser based in Nieuwegein, the Netherlands,[257] and was used in the all of the experiments discussed in this chapter. It consists of an electron gun and two linear accelerators. After

each accelerator, the electron beam can be deflected into a laser cavity comprising an undulator (Figure 5.3) and two gold-coated copper mirrors. The cavity after the first accelerator is tunable from 16 to 250 μm. After the second accelerator, the higher-velocity electrons emit light at shorter wavelengths, between 4 and 40 μm. The light from the laser cavity is guided by copper mirrors through evacuated tubes to the FELIX user station, where it is coupled into the vacuum chamber containing the experiment.

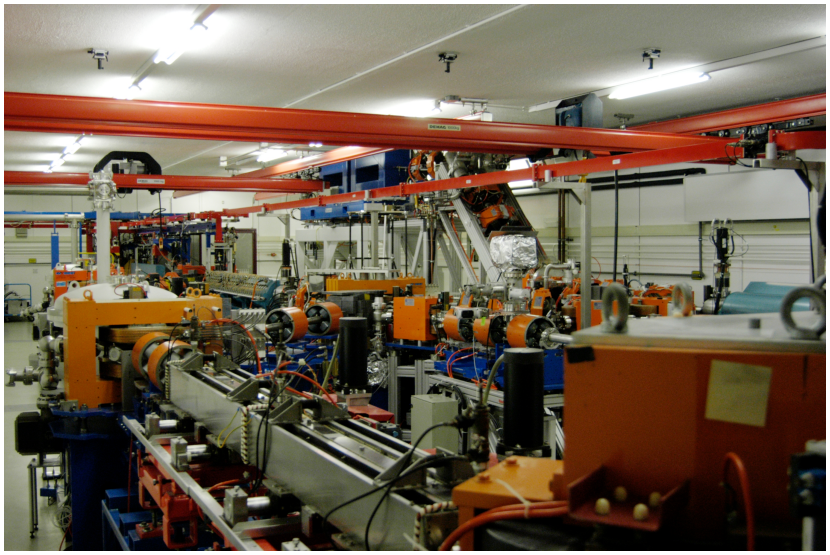


Figure 5.3: The components of the free electron laser FELIX. The long steel box in the foreground is one set of undulator magnets which cause the electron beam to radiate in the infrared.

The emitted infrared beam also contains a small proportion of higher harmonics of the fundamental frequency. This can be exploited as a convenient way of covering the high-wavenumber range where the fundamental pulse energies are very low. The third harmonic can be isolated by replacing the copper mirrors with those of a dielectric material chosen to have a maximum reflectivity at the third harmonic but very little at the fundamental frequency.[270]

FELIX runs on a duty cycle of 5 Hz, producing infrared pulses of up to 10 μs in length. Each of these macropulses is composed of micropulses, with a repetition rate of 1 GHz. Each micropulse has a width of 300 fs to several ps, and this is the limiting factor of the infrared resolution, which ranges from 0.3 to 1 % of the wavelength. The pulse energy

varies across the spectrum between *ca.* 10 to 20 mJ per macropulse. In the region where the third harmonic is used, the pulse energies fall to only a few mJ per macropulse. These pulse energies are sufficient to perform IR-MPD experiments, and the wavelength range covers many metal cluster modes and the modes of small molecules which can be adsorbed on the cluster surface.

5.3 Rhodium and adsorbed N_2O

Much of the interest in studying rhodium originates in its importance in heterogeneous catalysis, as it is commonly used in three-way catalytic converters to remove poisonous NO_x from car exhaust gases.[271] It also catalyses the formation of syn-gas,[272] and can catalyse methane reforming.[273]

The rhodium catalysts used in these processes are generally not crystalline, but are deposited or sputtered onto a supporting surface. This maximises the available surface area and also means that the metal surface is rich in defects and steps. Studying isolated clusters is a convenient way of understanding the huge complexity of such surfaces by isolating small parts and measuring their reactivity and other properties independently of any cluster-surface interactions.

5.3.1 Rhodium cluster reactivity

Reactions of rhodium clusters in the gas phase highlight this complexity, as reactivity with many species is strongly size-dependent. While reaction rates with CO or azidoacetonitrile proceed at collision rate and smoothly approach a limiting value for large clusters,[105,274] reaction rates of neighbouring cluster sizes with N_2O can vary by several orders of magnitude.[5] Similar variation is seen in the dehydrogenation of alkanes[98,275] and benzene.[276] Furthermore, individual cluster sizes can exhibit multiple reaction rates, im-

plying the presence of multiple isomers or spin-states with differing reactivity.[5,106] This suggests that cluster structure – whether electronic or geometric – has an enormous influence on reactivity.

5.3.2 Electronic properties

The electronic structure itself is also strongly size-dependent. The magnetic moments of Rh_n vary non-monotonically with cluster size, only approaching the non-magnetic bulk at around 60 atoms. The magnetic moments of small clusters are almost $1\,\mu_B$ per atom, whereas neighbouring 4*d* palladium and ruthenium clusters are not ferromagnetic at all.[277]

Another property which shows this behaviour is the electric polarisability, which is anomalously large for $n = 7$ and 10.[278] The results of this electric deflection experiment also demonstrate that neutral Rh_7 has a permanent dipole moment. This rules out the highly symmetrical pentagonal bipyramid structure that had previously been predicted by calculations.

5.3.3 Rhodium cluster structures

Many computational studies have been performed to try to explain these observations. For the reasons outlined in Section 5.2.1, DFT is the most common approach to calculating the structures of rhodium clusters. The 1993 paper of Reddy *et al.* first predicted the high spin states of Rh_n before the magnetic deflection methods were performed,[130] although in general the calculations overestimated the magnetic moments.[277] The calculated structures were close-packed, like the fcc crystal structure of bulk rhodium.[279] Later DFT studies also produced poly-tetrahedral lowest-energy isomers using plane-wave DFT[280] and the generalised gradient approximation (GGA) functional BP86.[281] Calculations based on semi-empirical potentials also find close-packed structures.[282]

More recently, Bae *et al.* applied GGA DFT using a plane wave method to rhodium clusters, and found structures based on cubic motifs up to $n = 64$.[283,284] Although these structures differed from the close-packed structures that had been previously found for rhodium and other clusters, the predicted magnetic moments were in better agreement with the results of the magnetic deflection experiment. Cubic structures were also found by groups using the GGA functionals PBE,[285] and PW-91.[286,287]

Comparisons of the performance of different functionals suggests that using a hybrid functional, which includes a percentage of exact Hartree-Fock exchange, changes the lowest-energy isomers from open, cubic motifs to close-packed structures. This was first suggested by Wang and Johnson, who calculated Ru_4 to be a square using non-hybrid functionals, and a tetrahedron using the hybrid functional PBE0.[125] Sun *et al.* confirmed this result for rhodium by calculating the structures of Rh_{13} in PBE and the hybrid functional B3LYP. PBE finds a structure based on capped cubes, whereas the B3LYP structure contains three fused octahedra.[288]

To resolve this disagreement, the IR-MPD spectra of Rh_n^+ have been recorded and compared to the calculated spectra of the cubic and close-packed isomers.[258,259] The highly symmetric cube structure of Rh_8^+ has only one infra-red active mode, which splits into peaks separated by *ca.* $20\,cm^{-1}$ if the symmetry is lowered slightly. This contrasts with the experimental spectrum, which shows two distinct peaks $50\,cm^{-1}$ apart, which is a much better match to the spectrum of the bicapped octahedral structure. This is strong evidence that the rhodium clusters prefer close-packed structures, and highlights the importance of functional choice in transition metal cluster calculations.

5.3.4 N_2O on rhodium metal surfaces

In addition to the reactivity studies of rhodium clusters with N_2O,[5] much work has been done on the interaction between N_2O and rhodium crystal surfaces. N_2O adsorbs molec-

ularly to Rh(100) and (110) and releases N_2 when heated, leaving an oxidised rhodium surface.[289,290] Some N_2O desorption is observed, but N_2 is the primary desorption component even at temperatures as low as 60 K.[291] Although decomposition has been reported on Rh(111),[292] Li and Bowker found that this surface is almost inert towards N_2O, and concluded that the N_2 formation occurs on defects rather than the Rh(111) surface itself.[293] This suggests that the N_2O reaction is strongly dependent on the structure of the substrate.

In temperature programmed desorption (TPD) experiments, the emitted N_2O shows an angular dependence. This is attributed to the presence of two adsorbed forms of N_2O: one form linear and parallel to the surface normal, and the other horizontally bridged across two rhodium atoms.[289] These structures were investigated using DFT, with the linear N_2O calculated to be bound *via* the terminal N atom.[294] Although no spectroscopic studies have been performed to confirm this binding mode, it is consistent with the nitrogen-bound structures found on other transition metal surfaces by reflection-absorption infrared spectroscopy on Pd(110),[295] and by electron energy loss spectroscopy on Pt(111)[296] and Ru(001).[297]

The mechanism of N_2O decomposition has been proposed to involve a rearrangement of the molecule from N atom-bound to horizontally bridged, followed by cleavage of the N-O bond. The reaction barriers were calculated using DFT to be 0.40 eV or 0.34 eV, depending on the periodic boundary conditions used.[298,299] This is very close to the calculated binding energy of the N_2O of 0.40 eV in both calculations, explaining why TPD causes some N_2O desorption together with the decomposition to N_2.

We have undertaken a far- and mid-IR-MPD study of $Rh_nN_2O^+$ to investigate the adsorption and reactivity on cluster surfaces, in comparison with its behaviour on rhodium metal surfaces.

5.4 Experimental methods

All experiments were carried out at the FELIX facility in the Netherlands described in Section 5.2.3. Two related IR-MPD experiments were performed: one using the argon-tagging technique, and the second in the absence of argon. Both used the metal cluster time-of-flight instrument belonging to the Fielicke and Meijer group (Figure 5.4). Cationic rhodium clusters are produced by laser ablation (532 nm, 10 Hz, ~ 10 mJ/pulse) of a rotating rhodium rod in the presence of a pulse of either helium or a helium/argon mixture. The gas pulse enters a clustering channel whose temperature can be adjusted using a cryogenically cooled reservoir. A late-mixing valve adds nitrous oxide to the clustering channel, in order to form cluster oxides and complexes with N_2O before expansion of the molecular beam into vacuum.

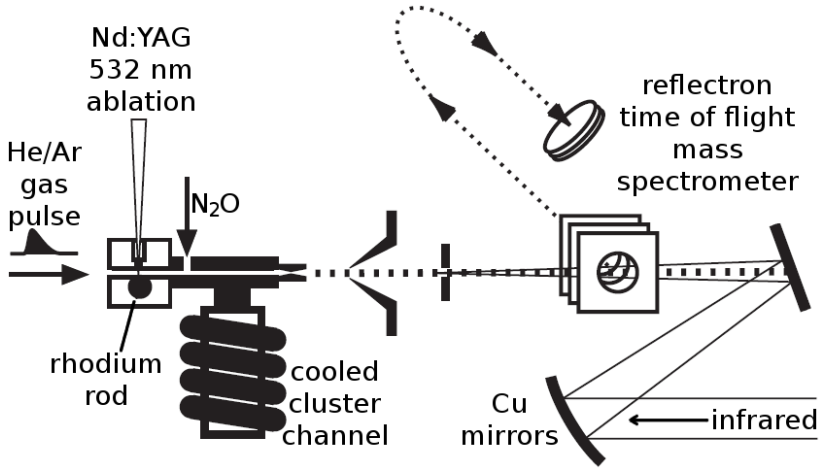


Figure 5.4: Time-of-flight instrument used in the IR-MPD experiments. The FELIX infrared beam is overlapped with the molecular beam carrying the Rh_n^+ clusters from the pulsed source. Adapted from work by Gruene *et al.*[300]

The molecular beam passes through a skimmer and a 1 mm-diameter aperture before entering the extraction region of a reflectron time-of-flight mass spectrometer, whose plates are pulsed to record the mass spectrum of the cationic clusters. On alternate shots, the molecular beam is intersected by a counter-propagating infrared pulse from the FELIX light source. If the light is resonant with an IR-active mode of one of the

clusters, it can absorb one or more photons and fragment. The alternate shots are compared to determine the proportion of clusters which have dissociated. Repeating this procedure as FELIX is scanned allows the full IR-MPD spectrum to be recorded.

5.4.1 Argon-tagging experiments

Argon tagging was used to record the full infrared spectra of the clusters between 100 and 2350 cm^{-1}. A mixture of 0.3 % argon in helium was used as the backing gas so that the clusters are formed with one or more adsorbed argon atoms. The internal energy of the clusters must be low enough for the argon atoms to bind to them, so the cluster channel was held at 173 K using the liquid nitrogen reservoir.

5.4.2 Reactivity studies

For the studies of the infrared-induced reactions on rhodium clusters, the seeded argon was omitted to simplify the number of available dissociation channels. The cluster channel was not cooled in this case but was held at 308 K, as the N_2O was observed to adsorb molecularly to the clusters even at room temperature.

As the N_2O modes were of interest in the reactivity studies, only these were scanned in this experimental variant. Spectra were recorded from 1250 to 1380 cm^{-1} (ν_1, N-O stretch), 510 to 620 cm^{-1} (ν_2, N-N-O bend), and 2190 to 2340 cm^{-1} (ν_3, N-N stretch).

5.5 Computational methods

The observed spectra and cluster reactions were compared with quantum chemical calculations performed using the computational package Turbomole.[301] Since it was necessary to calculate multiple geometric and spin-isomers of each cluster, density functional theory was chosen as the best compromise between accuracy and efficiency.

5.5.1 Functional choice

As described in Section 5.3.3, the lowest energy rhodium cluster isomer changes depending on the density functional used, with hybrid functionals favouring the octahedral structures which are a better fit to the experimental vibrational spectra. Many of the most popular functionals such as B3LYP[119,120] are less suitable for metal clusters, because their parameters have been fitted to small molecular systems of main-group elements.[124] For non-empirical functionals like TPSS[118] and PBE,[116] the parameters were chosen so that the functional's properties are as close as possible to the theoretical exact density functional. For example, the self-correlation energy of an electron should be zero, and the exchange and correlation energies should approach the correct physical limiting values as the atomic separation is increased.[302]

In practice, these *ab initio* functionals do not perform quite as well as the empirical functionals on molecules which are similar to the parameterisation set, but are more suited to systems like transition metal clusters which were not included in the parameterisation.[113] Most transition metal validation studies, however, compare calculations to experimental properties of metal atom-ligand systems, bulk metals and occasionally transition metal dimers,[111] so caution is still required when choosing a suitable function for larger transition metal clusters.

Based on the results of the Rh_n^+ IR-MPD spectra, for reasons which are unclear it seems to be necessary to use a hybrid functional when calculating rhodium clusters in order to include a fraction of exact Hartree-Fock exchange. For this reason, two hybrid functionals, PBE0 (also called PBE1, containing 25 % HF exchange)[122] and TPSSh (10 % HF exchange),[123] are used in the computational studies discussed in this chapter. PBE0 is the functional which has been used successfully in calculating bare Rh_n^+ IR-MPD spectra.[258] TPSSh has been shown to calculate metal-ligand bond dissociation energies more accurately than other functionals, which is especially relevant to the reactivity section of

this chapter, although the mean error in binding energies was still 0.3 eV.[303]

5.5.2 Basis sets

Rhodium clusters decorated with N_2O molecules were optimised using Ahlrich's triple-zeta valence plus polarisation (TZVP) basis sets for all atoms.[304] This basis set has previously been used in rhodium cluster-ligand systems to calculate $Rh_n(CO)_m^+$ infrared spectra,[305] and is considered large enough to calculate accurate transition metal-ligand bond lengths.[303] The Rh TZVP basis set replaces the 28 core electrons with an effective core potential (ECP) to efficiently treat the electrons which are not involved in bonding.

Auxiliary TZVP basis sets for all atoms were also required, in order to take advantage of Turbomole's efficient resolution of the identity (RI) approximation.[306] The auxiliary basis sets are an expansion of four-electron integrals into two-electron integrals, which increases the speed of the calculation without compromising the computational accuracy.[307,308] This method is particularly efficient for large basis sets, reducing the calculation time by over an order of magnitude.[309]

5.5.3 Structure optimisation

The calculated rhodium clusters were based on the structures previously found in the group by Harding *et al*,[259] using a combination of basin-hopping[310] and DFT with the PBE0 functional. On each cluster, N_2O was placed on a range of plausible binding sites in atop, bridged and hollow-site positions (bonded to one, two and three rhodium atoms, respectively). Other binding geometries were also optimised: N_2O bridged across two rhodium atoms, bound *via* its terminal O and N atoms; and dissociated N_2O with the O atom and the N_2 fragment bound separately to the cluster. Dissociation products N_2O, N_2, Rh_n^+ and Rh_nO^+ were also calculated in order to determine the binding energies of the two molecules to the clusters.

Each of these starting structures was optimised using the jobex module in Turbomole. This operates by performing a DFT calculation of the total electron energy using the RI approximation,[308] followed by a calculation of the potential energy gradient and the forces on the atoms. The structure is adjusted by Turbomole's statpt module to one that is predicted to be of lower energy, following the gradients and force constants in a quasi-Newton-Raphson method.[311] The RI-DFT and relaxation steps are iterated until the energy change on each cycle has fallen below a threshold fixed at 10^{-6} Ha, and the gradient is less than 10^{-3} a.u. This method is not a global optimisation, but can only find local minima in the region of the starting geometry, hence the need to optimise many plausible isomers with different cluster geometries and ligand positions.

Each structure is optimised in several spin states, in order to find the lowest-energy spin-isomer as well as the lowest-energy geometrical isomers. Once a converged structure has been found, its vibrational normal modes are calculated using the Turbomole module aoforce.[312] Each negative eigenvalue of the Hessian corresponds to a maximum in the potential energy surface along a particular dimension, which implies that the converged structure is at a transition state rather than an energy minimum. When transition states are found, they are distorted along the mode with the negative eigenvalue and reoptimised in an attempt to locate a nearby minimum. Once a local minimum has been found, its Hessian has no negative eigenvalues, and the normal mode analysis gives the harmonic frequencies of the vibrational modes with which to compare the experimental spectra.

5.5.4 Reaction pathways

To find the feasible reaction pathways, the transition states between the local minima must be calculated. Transition state searches in Turbomole also use the statpt module, which implements the Trust Imaging Minimisation Method (TRIM).[313] This algorithm takes

a starting geometry close to the transition state of interest, which has one negative eigenvalue. The corresponding eigenvector is followed to find a geometry in which the potential energy is maximised in the direction of the eigenvector but minimised in every other dimension.

For TRIM to converge, it is necessary to start with a good approximation to the geometry of the transition state. The starting structures for the N_2O reactions were estimated by inspecting the geometries of the previously calculated local minima and constructing geometries that lie between them. Transition state structures that had previously been calculated on clusters[314] and extended rhodium surfaces[298] were included as starting geometries in these calculations.

A normal mode analysis is run on each converged geometry to check that there is only one negative eigenvalue, meaning that the structure is at a saddle point on the potential energy surface. If this is the case, the cluster is distorted in both directions along this eigenvector, and reoptimised to find the closest minima on either side of the transition state. By repeating this for every transition state geometry which could be converged, the possible reaction pathways of the molecule were investigated.

5.6 $Rh_nN_2O^+$ spectroscopy

Cluster-ligand mass spectrum

The metal cluster source was tuned to produce N_2O-decorated Rh_n^+ clusters up to $n \simeq 20$, with the most abundant clusters in the range $4 \leq n \leq 8$. A small portion of the mass spectrum is given in Figure 5.5 with the major peaks identified. The N_2O from the reaction valve has adsorbed onto some clusters, and partially oxidised others to produce $Rh_nN_2O^+$ and Rh_nO^+ clusters. One or more argon atoms also adsorb to some of the clusters. All of the less intense mass peaks are assignable to rhodium clusters with

multiple adsorbed N_2O molecules, oxygen or argon atoms, or combinations of these.

Dissociation caused by infrared absorption appears in the mass spectrum as a decrease in the intensity of the mass spectrum peak, together with an increase in the signal from the fragment ions. In Figure 5.5, the infrared is tuned to the pseudo-symmetric stretch ν_1 of adsorbed N_2O. The infrared is absorbed by the $Rh_6N_2OAr^+$ cluster, and IVR transfers this energy to the weak cluster-argon bond which breaks, depleting the mass spectrum peak of this ion and enhancing the $Rh_6N_2O^+$ peak. Concomitant enhancement of the Rh_6O^+ peak suggests that N_2 is being lost from the absorbing cluster in addition to the argon atoms, in a process that will be discussed further in Section 5.7.

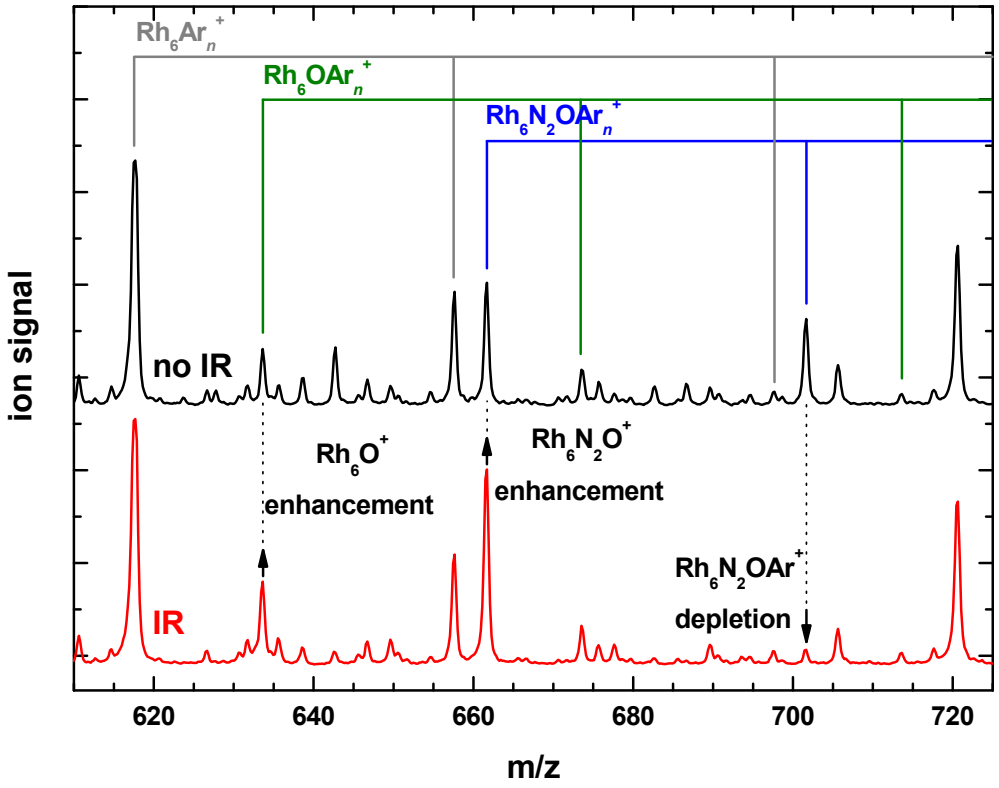


Figure 5.5: Mass spectrum of the clusters in the region of Rh_6^+, with assignments for some of the most abundant species. The upper trace (in black) is taken without the FELIX infrared beam present. The lower trace (in red) is taken with the infrared overlapped with the clusters and tuned to 1290 cm^{-1}, on resonance with a mode of $Rh_6N_2OAr_n^+$. $Rh_6N_2OAr^+$ is being depleted to form $Rh_6N_2O^+$. The Rh_6O^+ is also enhanced, suggesting a larger cluster (here, $Rh_6N_2OAr^+$) is fragmenting into this channel.

The depletions observed in this mass spectrum are large: *ca.* 80 % in the case of $Rh_6N_2OAr^+$. To avoid saturation, regions with large depletions were re-scanned with the infrared attenuated so that depletions were never more than 50 %.

Directly subtracting one trace from the other gives the absolute depletion and enhancements of the species. The relative cross-section, σ, of each cluster can also be calculated following the Beer-Lambert law:

$$\sigma = \ln\left(\frac{I_0}{I}\right) \tag{5.1}$$

where I_0 and I are the intensities of the mass spectrum in the absence and presence of the infrared, respectively.

Spectroscopy overview

The relative cross section of all the clusters was recorded as the FELIX infrared beam was scanned between 100 cm^{-1} and 2340 cm^{-1}. Figure 5.6 gives an overview of the absorptions of the $Rh_nN_2OAr^+$ clusters across the spectrum. For all cluster sizes, intense absorptions were observed in three regions: 540–580 cm^{-1}, 1280–1330 cm^{-1} and 2230–2320 cm^{-1}. These are within 50 cm^{-1} of the three infrared absorptions of the N_2O molecule, which are also marked on the spectrum. The intense depletions are, therefore, likely due to molecular N_2O adsorbed on the rhodium clusters.

Below 500 cm^{-1} there are several less intense features arising from the internal vibrational modes of the cluster and the metal-ligand modes.

5.6.1 Spectroscopy of the N_2O modes

Molecular N_2O has three normal modes, summarised in Figure 5.7: two stretches ν_1 and ν_3 and a doubly-degenerate bend ν_2. The experimental values of $\Delta G_{1/2}$ of ν_1, ν_2 and ν_3 are 1271.4, 589.8 and 2223.8 cm^{-1}, respectively.[315]

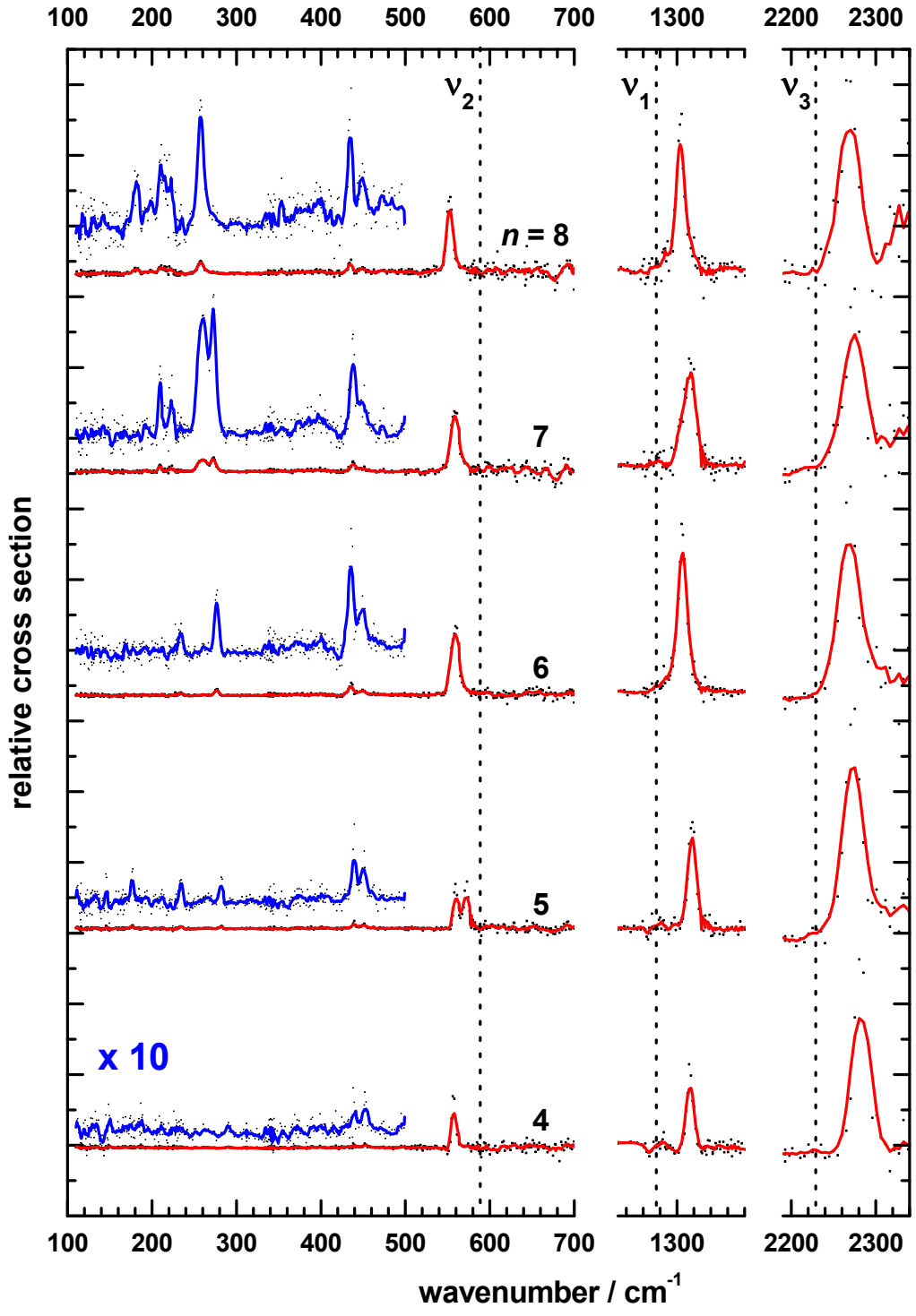


Figure 5.6: IR-MPD spectra of argon-tagged $Rh_nN_2O^+$ ($n = 4 - 8$) clusters. Dashed lines mark the absorptions of gas-phase N_2O. Strong absorptions of the clusters close to the free N_2O wavenumbers are characteristic of molecularly N_2O adsorbed on the surface of the clusters. Weaker absorptions at lower wavenumbers arise from vibrational modes of the cluster and the cluster-ligand interaction.

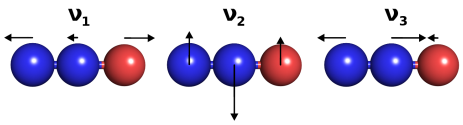
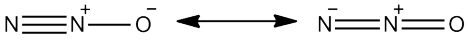


Figure 5.7: Vibrational modes of free N_2O: the pseudo-symmetric or N-O stretch, ν_1; the doubly-degenerate bend, ν_2; and the pseudo-antisymmetric or N-N stretch, ν_3.

These modes have previously been observed in vibrational spectra of N_2O molecularly adsorbed on extended surfaces, shifted slightly from their absorption frequencies in the gas phase. On transition metals, the N_2O stretches are shifted to higher wavenumbers and the bend to lower wavenumbers.[295–297] In contrast, the pseudo-symmetric stretch ν_1 is red-shifted on metal oxide surfaces such as ZnO,[316] TiO_2(110),[317] $\eta-Al_2O_3$,[318] and ZrO_2.[319] Both N_2O species are observed on TiO_2 powder[320] and Cr_2O_3.[321]



1 **2**

Figure 5.8: Resonance structures of N_2O.

The existence of the two different species is interpreted using the resonance forms of N_2O (Figure 5.8). N_2O can bond to the surface by donating electrons from the O lone-pair or the N lone-pair. Interaction of the O lone-pair with a surface stabilises Structure 1, which has a weaker N-O bond than free N_2O, and hence has a red-shifted ν_1 band. Structure 2 is isoelectronic with CO_2, whose symmetric and antisymmetric stretching modes lie at higher frequencies than the N_2O stretches. This suggests that the adsorbed N_2O species with blue-shifted modes is bound *via* the terminal N atom.[320,321]

In the infrared spectra of the $Rh_nN_2O^+$ clusters, only blue-shifted stretches are observed. Although there is some variation in the N_2O absorption wavenumbers between cluster sizes, ν_1 and ν_3 occur at wavenumbers 30 to 45 cm^{-1} higher than for free N_2O in all cases. The bend is red-shifted, usually by *ca.* 30 cm^{-1}. Figure 5.9 summarises these shifts in the experimental absorption wavenumbers. Following the reasoning applied to surface-adsorbed N_2O, these spectra are consistent with N-bound N_2O, as was observed

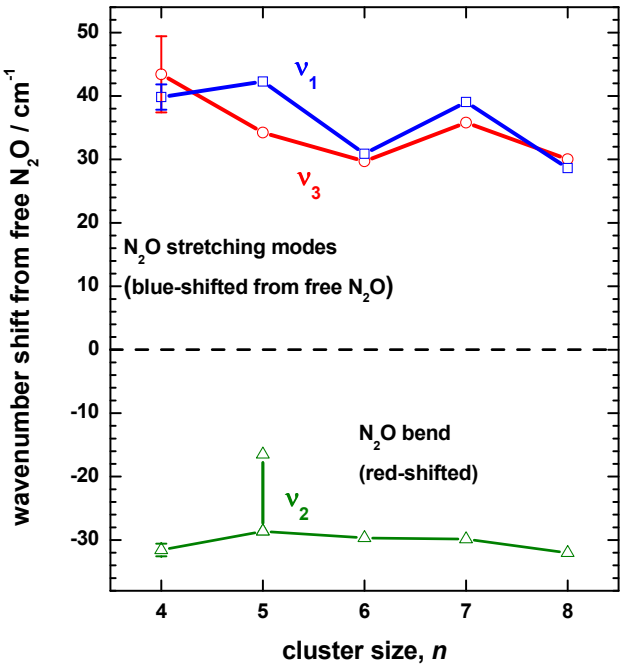


Figure 5.9: Observed shifts in N_2O vibrational wavenumbers in the $Rh_nN_2O^+$ IR-MPD spectra compared to free gas-phase N_2O. Error bars (which apply to all cluster sizes but shown only for $n = 4$) are the bandwidth of the FELIX infrared pulse.

on unoxidised transition metal surfaces.

Calculated N_2O modes

A more thorough interpretation can be made by comparing experiment with the results of DFT calculations on a range of possible binding geometries for N_2O on the clusters. N_2O was optimised on a Rh_6^+ cluster, whose lowest-lying isomer was previously calculated to be octahedral.[136] Local minima were found with linear N_2O bound atop, *via* either the terminal N or O atom, dissociated and in two bridged configurations (Figure 5.10). The results are shown for the TPSSh and PBE0 functionals, and compared with the calculated vibrational modes of free N_2O.

In both cases, dissociated N_2O (Figure 5.10(b) and (g)) lies lowest in energy, followed by the atop and then the bridged structures. In the 500-2500 cm^{-1} region there are two predicted infrared absorptions by dissociated N_2O: the N-N stretch at *ca.* 2350 cm^{-1} and an oxide mode at *ca.* 590 cm^{-1}. This spectrum does not account for the absorption at 1307 cm^{-1}, so the dissociated structure can be discounted even though it is the

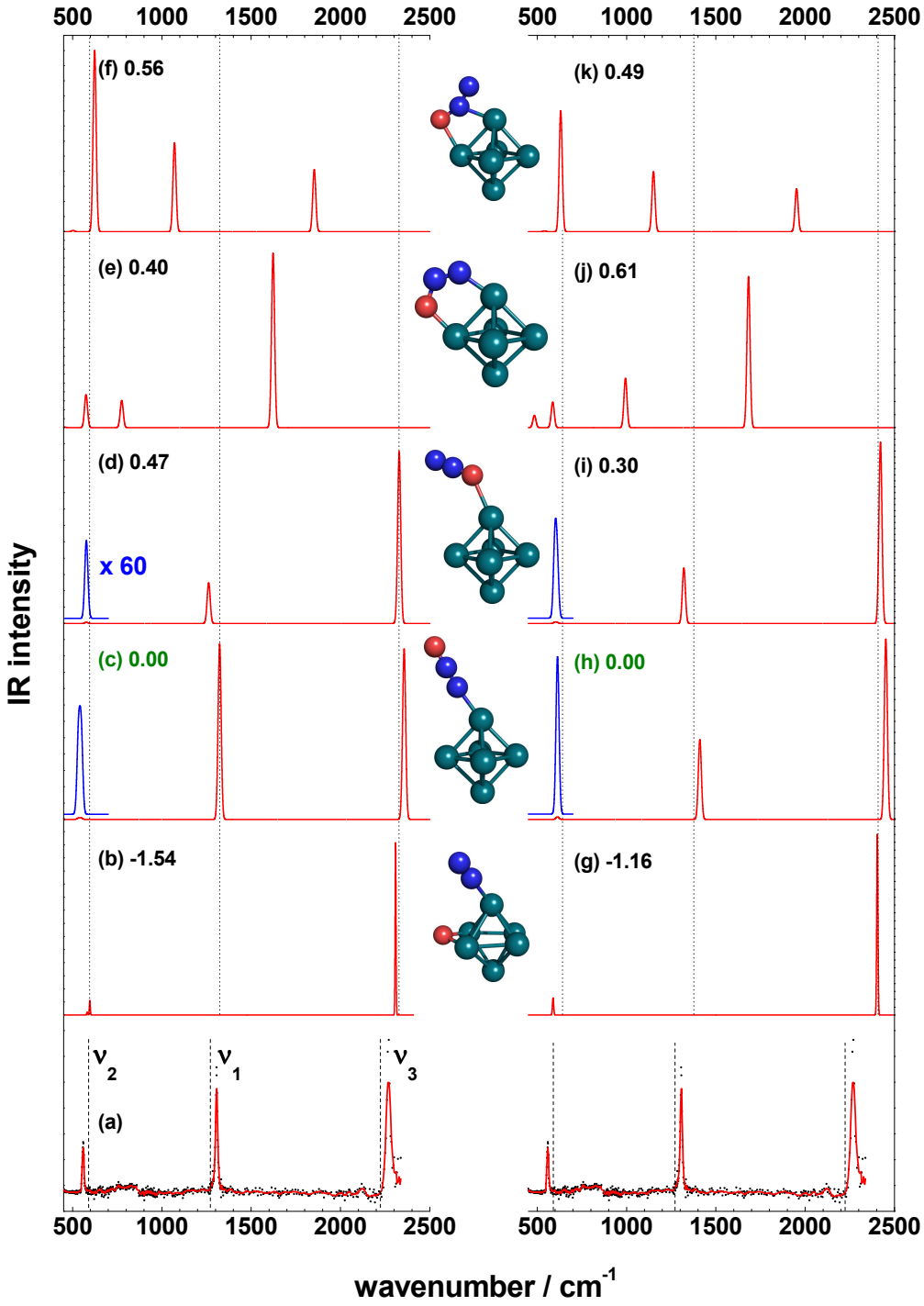


Figure 5.10: N_2O modes in the $Rh_6N_2O^+$ IR-MPD spectrum (a), with the calculated spectra of all the N_2O adsorption geometries (b)-(g). Left: structures calculated in the TPSSh functional. Right: structures calculated in PBE0. Calculated spectra are convoluted with a Gaussian of FWHM of 20 cm^{-1}. The energies of the isomers are given in eV relative to the N-bound atop structures (c) and (h). In both functionals, the best agreement with the experimental data is the N-bound atop N_2O spectrum.

calculated global minimum.

The atop structures (Figure 5.10(c), (d), (h) and (i)) have infrared-active modes within 60 cm^{-1} of the free N_2O modes. The PBE0 spectra support the interpretation of the studies of surface-adsorbed N_2O, which is that ν_1 is blue- and red-shifted in N- and O-bound N_2O, respectively. This confirms the assignment of N_2O bound by the terminal N atom to the surface of the clusters. The agreement with the TPSSh predictions is not quite so good: here ν_1 is calculated to have no shift upon adsorption to the rhodium cluster. The N-bound geometry is, however, still a better match to the experimental spectrum than that of the O-bound structure.

Distortion of the N_2O in order to bridge across two rhodium atoms (Figure 5.10(e), (f), (j) and (k)) is a significant perturbation to the vibrational structure of the molecule, lowering the absorption wavenumbers by several hundred cm^{-1}. These structures have been observed in TPD studies of N_2O on Rh crystal faces,[289] but there is no evidence for bridged N_2O on Rh_n^+.

The same adsorption geometries have been calculated on $n = 4, 5$, with the same qualitative outcome. These DFT calculations are consistent with the original argument based on resonance structures, and together they suggest that the only $Rh_nN_2O^+$ species detected by IR-MPD are those in which N_2O is molecularly adsorbed through the terminal N atom.

$Rh_5N_2O^+$ bending mode

When N_2O is adsorbed on Rh_5^+, the bending mode, ν_2, splits into two peaks separated by 18 cm^{-1} (Figure 5.6). Since the cluster modes are predicted to lie at much lower wavenumbers, both of these peaks must be due to the N_2O ligand. One possibility is the presence of multiple isomers of $Rh_5N_2O^+$. This cannot be ruled out, but if the bending mode shifts because of adsorption to a different cluster isomer then the other modes

might be expected to do the same. The two stretching modes are not split in the case of $n = 5$, and they are no broader relative to the other cluster sizes.

A second possibility is that the cluster lifts the degeneracy of the N_2O bend. DFT calculations on many different isomers confirm that the degeneracy remains when the N_2O is bound to a highly symmetrical site, but is lifted when the N_2O is bound to a lower symmetry site. TPSSh, in particular, tends to calculate structures with N_2O in an asymmetrical binding position: even on symmetrical cluster sites such as the Rh_6^+ octahedron, the structures optimised in TPSSh typically have lower symmetry because the N_2O is bound at an angle to the cluster's symmetry axis, which also lowers the degeneracy of the bending mode, causing TPSSh to predict the bending modes to be separated by up to $30\,cm^{-1}$. In PBE0 the N_2O is usually found to be parallel to the symmetry axis, predicting a small split in the N_2O bend wavenumbers which is more consistent with experiment.

5.6.2 Metal cluster modes

The vibrational modes of the metal clusters themselves lie below $300\,cm^{-1}$. Because of the small dipole moments and the larger number of photons required to cause photodissociation of the cluster-argon bond, these absorptions are very much weaker than those of the N_2O ligand. The perturbation caused by the presence of N_2O is large enough that the metal cluster modes observed here cannot be identified with those in the simultaneously-recorded IR-MPD spectra of the $Rh_nAr_m^+$ clusters.[258,259] In order to identify cluster structures from these spectra, they must be compared to calculations of the clusters bonded to N_2O ligands.

Figure 5.11 shows the $Rh_nN_2O^+$ isomers which have been calculated for comparison with the IR-MPD spectra. A wide range of cluster geometries were optimised in three or four spin states, based on previous structures calculated for the bare clusters.[259,314] For

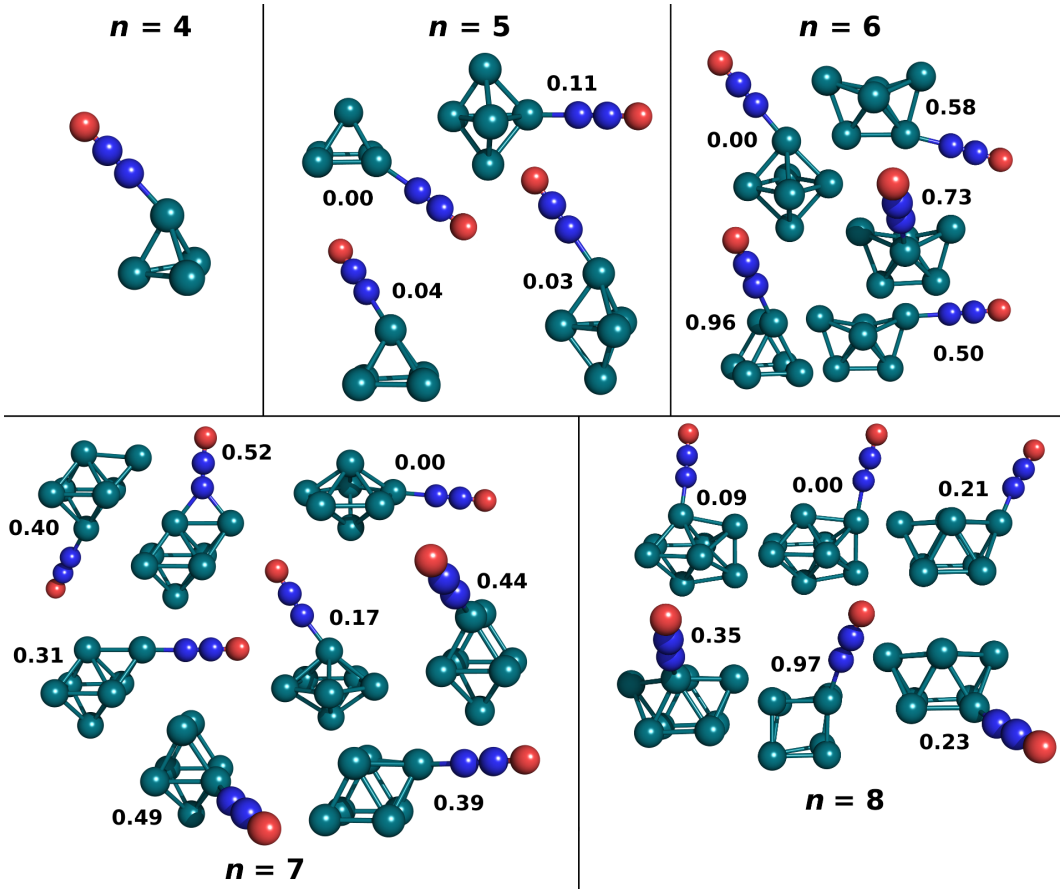


Figure 5.11: $Rh_nN_2O^+$ isomers calculated by DFT in which the N_2O is bound *via* the terminal N atom. The energy of each cluster is given in eV relative to the lowest-lying isomer of that size. All clusters were calculated using the TPSSh functional, and only the lowest-lying spin state is shown. The energies of other low-lying spin states are given in Table 5.1.

each cluster geometry, the energies of the three lowest-lying spin states are summarised in Table 5.1. The only N_2O binding mode considered was the N-bound atop geometry because of the conclusions of the N_2O vibrational mode analysis discussed in Section 5.6.1.

$Rh_4N_2O^+$

The only stable $Rh_4N_2O^+$ isomer is the tetrahedron; planar structures collapse to three-dimensional structures during optimisation. The lowest energy spin-isomer is that with $2S + 1 = 8$, with 6-tet and 10-tet structures lying *ca.* 0.3 and 1.7 eV higher, respectively. Unfortunately, the signal-to-noise ratio is not high enough to identify peaks in the $n = 4$

Table 5.1: Energies given relative to the lowest calculated structure of the same cluster size, of the $Rh_nN_2O^+$ isomers calculated in the three lowest-lying different spin states using the TPSSh functional, corresponding to the geometries shown in Figure 5.11. A range of energies is given for those clusters with several different N_2O absorption sites.

n	**cluster geometry**	**2S + 1**	**relative E / eV**
4	tetrahedron	6	0.26
		8	0.00
		10	1.64
5	square-based pyramid	7	0.13 – 0.21
		9	0.00 – 0.04
		11	0.90 – 1.08
	trigonal bipyramid	7	0.24 – 0.28
		9	0.03 – 0.11
		11	1.08
6	octahedron	8	0.06
		10	0.00
		12	0.68
	boat	8	0.73 – 1.03
		10	0.50 – 0.73
		12	0.90 – 1.02
	trigonal prism	8	0.85
		10	0.96
		12	1.30
7	pentagonal bipyramid	9	0.47 – 0.55
		11	0.00 – 0.17
		13	0.27 – 0.34
	capped octahedron	9	0.37 – 0.54
		11	0.31 – 0.52
		13	0.34 – 0.60
	capped trigonal prism	9	0.39 – 0.50
		11	0.39 – 0.49
		13	0.67 – 0.75
8	bicapped octahedron	12	0.09 – 0.29
		14	0.00 – 0.09
		16	0.32 – 0.40
	bicapped trigonal prism	12	0.25 – 0.40
		14	0.21 – 0.35
		16	0.45 – 0.56
	cube	12	0.65
		14	0.97
		16	1.10

spectrum, so the spectra predicted by DFT cannot be compared to the IR-MPD spectra.

$Rh_5N_2O^+$

Four nearly iso-energetic isomers were calculated for $Rh_5N_2O^+$, based on a square-based pyramid and a trigonal bipyramid. The lowest-lying spin state was the 9-tet, with the 7-tet lying 0.1 to 0.3 eV higher, and the 11-tet *ca.* 0.7 eV higher still.

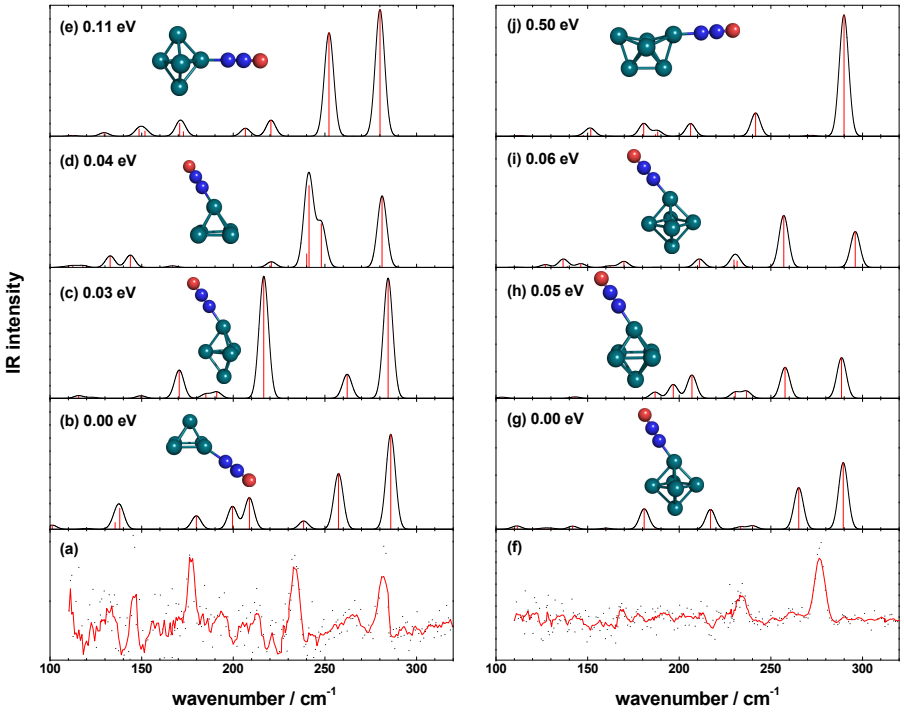


Figure 5.12: Left: (a) IR-MPD spectrum of $Rh_5N_2OAr^+$ in the region of the metal-metal modes. The spectra of the calculated lowest-lying isomers, all of which have spin $2S+1=9$, are shown above in (b)-(e). Right: (f) IR-MPD spectrum of $Rh_6N_2OAr^+$. The lowest-lying isomers are calculated to be octahedra with $2S+1=10$ (g), (h), and 8 (i). Isomer (j) is a more open boat structure, with $2S+1=10$. The relative energy of each isomer is given in eV.

The calculated spectra of the four lowest-lying isomers, all with $2S+1=9$, are given in Figure 5.12 (left half) together with the experimental IR-MPD spectrum of $Rh_5N_2OAr^+$. The absorption features in this spectrum are weak, but at least three features can be identified. The best match is isomer (c), the trigonal bipyramid, as its three most intense peaks have a similar separation to the experimental features, but none of the calculated spectra are a good match to experiment.

$Rh_6N_2O^+$

The calculated global minimum of $Rh_6N_2O^+$ is based on an octahedron with $2S+1=10$. The other stable geometric isomers, an open boat structure and a trigonal prism, both lie more than 0.5 eV higher in energy. The 8-tet octahedral structure is very low-lying, only 0.06 eV above the 10-tet.

Figure 5.12 (right half) shows the $Rh_6N_2OAr^+$ IR-MPD spectrum. There are only two modes in the experimental spectrum, suggesting that the structure is highly symmetrical. Of the calculated spectra, the 8-tet octahedron (i) is the best match to the experimental spectrum (f). Although the boat structure (j) is also a reasonable fit, it is much higher in energy, and was also found to be a very poor match to the IR-MPD spectrum of Rh_6Ar^+.[259]

$Rh_7N_2O^+$

The pentagonal bipyramid-based structures are calculated to be the lowest-lying isomers of this cluster, with the 11-tet spin state being the lowest in energy of these. Structures based on a capped octahedron and a capped trigonal prism lie 0.31 to 0.52 eV higher in energy.

The spectra of five lowest-lying structures, based on 11-tet and 13-tet pentagonal bipyramids and capped octahedra, are shown in Figure 5.13 (left half) above the IR-MPD spectrum of $Rh_7N_2OAr^+$. None of the DFT spectra can explain the intense pair of peaks between 250 and 280 cm^{-1}, which suggests that more than one isomer may be present. Rh_7^+ is one of the clusters which showed biexponential reaction rates in collisions with N_2O,[5] so the occurrence of multiple isomers in this experiment is possible.

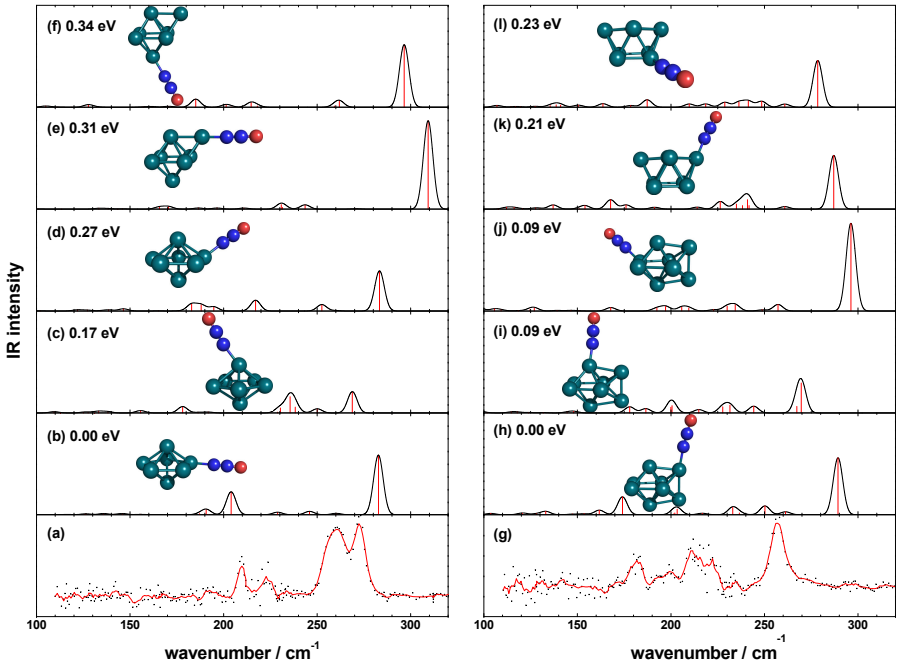


Figure 5.13: Left: IR-MPD (a) and calculated (b)-(f) spectra of $Rh_7N_2OAr^+$ in the region of the metal-metal modes. The calculated lowest-lying isomers are pentagonal bipyramids and capped octahedra with $2S+1=11$ (b), (c), (e), and 13 (d), (f). Right: Measured (g) and calculated (h)-(l) spectra of $Rh_8N_2OAr^+$. The lowest-energy isomers are bicapped octahedra and with $2S+1=14$ (h), (i), and 12 (j). The next lowest-lying isomers are based on bicapped trigonal prisms, (k), (l), both with $2S+1=12$. The relative energy of each isomer is given in eV.

$Rh_8N_2O^+$

The TPSSh putative global minimum of $Rh_8N_2O^+$ is based on a bicapped octahedron, in agreement with the IR-MPD spectrum of the bare Rh_8^+ cluster and the calculations performed in the PBE0 functional.[258] Structures based on a bicapped trigonal prism lie 0.21 to 0.35 eV higher in energy, with the cube structure, slightly distorted, almost 1 eV above the bicapped octahedron. The $2S+1=14$ spin state lies lowest, but the 12-tet structures lie less than 0.1 eV higher than the corresponding 14-tet structures.

Figure 5.13 (right half) shows the IR-MPD spectrum of $Rh_8N_2OAr^+$ (g) together with the five calculated lowest-lying isomers, which are based on the 14-tet and 12-tet bicapped octahedra and trigonal prisms. The closest matches to the experimental spectrum are bicapped octahedra structures (h) and (i), which differ only in the binding site of the N_2O. The lack of any strong features in the DFT spectra, however, preclude a definitive

assignment of the structure.

5.6.3 Absorptions in the 400-500 cm^{-1} range

The only features which cannot be explained by the calculated spectra of N-bound N_2O are the two peaks which lie at around 440 cm^{-1}, between the cluster modes and the N_2O modes (Figure 5.6). In every cluster size studied here, the peaks appear as depletions in the Ar-tagged spectra and matching enhancements in the untagged spectra, but do not correspond to any predicted vibration of the $Rh_nN_2O^+$ clusters.

Absorptions in this range can be explained by a small proportion of cluster with adsorbed N_2O that has dissociated into N + NO, since both of these adsorbed species are calculated to absorb at around 450 cm^{-1}. However, this species is also predicted to have much stronger absorptions at higher wavenumbers: the Rh-N stretch occurs at *ca.* 620 cm^{-1}, and NO absorbs at 1900 or 1600 cm^{-1}, depending on the geometry of its binding to the cluster. Since these modes do not appear in any of the IR-MPD spectrum, this form of dissociated N_2O is unlikely to be the cause of the modes which are observed at around 440 cm^{-1}.

The wavenumbers of these two absorptions are 434-439 cm^{-1} and 449-451 cm^{-1}, with some variation between cluster sizes. These values are 1/3 of the ν_1 absorption and 1/5 of ν_3, respectively, suggesting that the two peaks are artifacts due to N_2O absorbing higher harmonics of the infrared beam. The odd-numbered harmonics are known to be contaminants in free electron laser output – indeed, the third harmonic is isolated for use in spectroscopy experiments by using coated cavity mirrors.[270]

The size-dependence of the peak intensity also mirrors the relative intensities of ν_1 and ν_3, with the lower-wavenumber peak growing in relative intensity as the cluster size is increased (Figure 5.6). It seems likely, therefore, that these peaks are best explained by third- and fifth-harmonic contamination rather than another cluster isomer.

5.7 Infrared-induced $Rh_nN_2O^+$ reactivity

The IR-MPD experiments described above involved monitoring the loss of argon atoms from the clusters. The heating of the cluster after photon-absorption and IVR that breaks the cluster-argon bond can also lead to other thermally-induced processes in the cluster. This section discusses the unexpected observation of cluster reactivity caused by heating the $Rh_nN_2O^+$ clusters by infrared absorption.

5.7.1 Spectroscopic evidence

Argon-tagged IR-MPD spectra

The N_2O introduced into the experiment binds molecularly to some clusters to produce the $Rh_nN_2O^+$ clusters whose spectra were analysed in Section 5.6. In the cluster source,

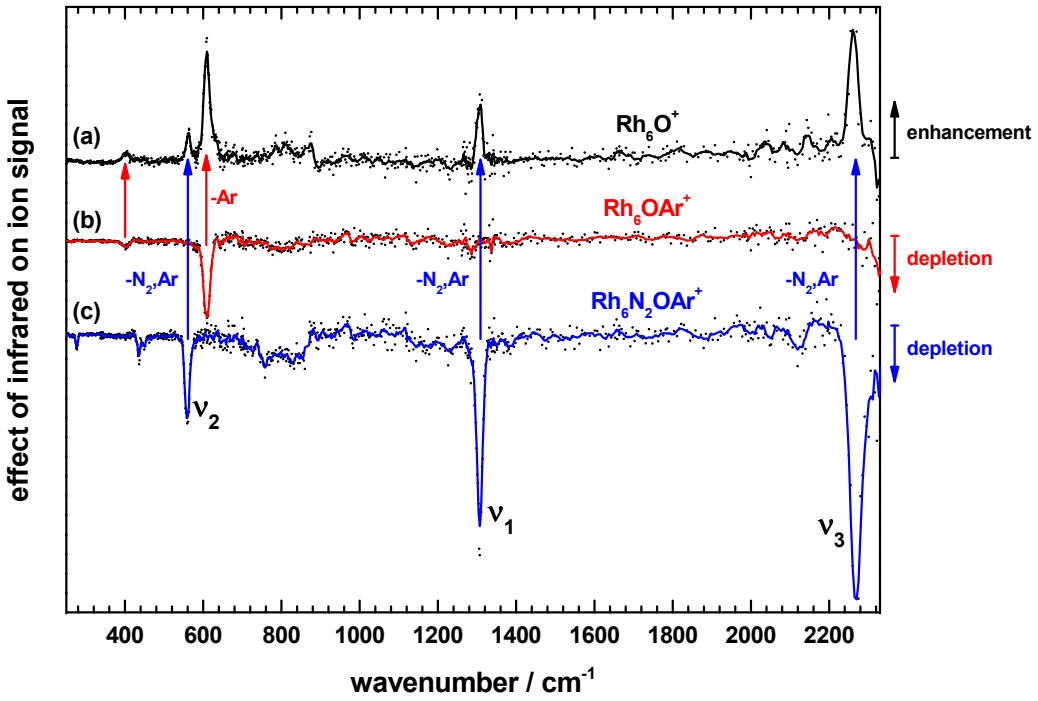


Figure 5.14: The Rh_6O^+ ion signal (a) is enhanced at 609 cm^{-1} and 403 cm^{-1} due to argon-loss from Rh_6OAr^+ (b) when the infrared is resonant with vibrational modes of the oxide. The signal is also enhanced at the wavenumbers of the $Rh_6N_2O^+$ depletions (c), suggesting that this is fragmenting to form Rh_6O^+.

however, some of the N_2O reacts with the clusters to produce the oxide clusters, $Rh_nO_m^+$, observed in the mass spectrum (Figure 5.5). The absorption spectra of the argon-tagged oxides were recorded in the same FELIX scans as those of the N_2O complexes. Disappointingly low signal in the metal-metal region precludes assigning their structures, but the cluster-oxygen stretch does absorb very strongly at around $600\,cm^{-1}$.

The Rh_6OAr^+ spectrum is given in Figure 5.14(b), showing this strong feature and a weaker band at $400\,cm^{-1}$. The Rh_6O^+ spectrum (Figure 5.14(a)) shows a corresponding *enhancement* at the same wavenumbers. There are, however, additional enhancements in this spectrum which cannot be explained by argon-loss from Rh_6OAr^+. Instead, the parent ion appears to be $Rh_6N_2OAr_m^+$, because its depletions lie at the same wavenumbers as the oxide enhancement peaks (Figure 5.14(c)). This implies that heating the N_2O-complexed cluster by infrared absorption causes the loss of Ar *and* N_2, and the production of a partially oxidised cluster:

$$Rh_6N_2OAr_m^+ + h\nu \rightarrow Rh_6O^+ + N_2 + mAr \tag{5.2}$$

IR-MPD in absence of argon

The same process was observed on cluster sizes $n = 4, 6, 7, 8$, but pairing the parent ions with the products was complicated by the presence of the argon atoms, since argon-loss causes enhancement of the $Rh_nN_2O^+$ species at these wavenumbers, masking any potential depletion into oxide products. When the IR-MPD experiment is repeated in the absence of argon, these Rh_nO^+ clusters do indeed show enhancement around the N_2O vibrational modes.

There are, of course, other species present in the cluster distribution which must be considered when determining the true source of the oxide cluster products. The oxide enhancement at the wavenumbers of the N_2O modes means that the molecular N_2O is

adsorbed on the parent ion, but there are several such species in the mass spectrum besides $Rh_nN_2O^+$.

Species containing only rhodium and two or more oxygen atoms cannot cause the monoxide enhancement, as their IR-MPD spectra do not show any absorptions above 800 cm^{-1}. A more realistic possibility are the clusters with a co-adsorbed N_2O molecule and O atom. These are produced by the cluster source, and have a mid-infrared absorption spectrum which consists of N_2O modes and the Rh-O modes seen in the $Rh_nOAr_m^+$ spectra. Infrared-heating of these $Rh_nON_2O^+$ clusters could conceivably lead to N_2O loss, producing the observed Rh_nO^+ enhancement. While this process cannot be ruled out, it does not account for the majority of the oxide production, as the absolute magnitude of the $Rh_nON_2O^+$ depletion is smaller than the corresponding Rh_nO^+ enhancement. The spectrum of $Rh_6ON_2O^+$ in the N_2O bend region is given as an example in Figure 5.15. Here the oxide enhancement is too large to be explained by N_2O desorption.

The only absorbing species whose depletions are large enough to account for the ox-

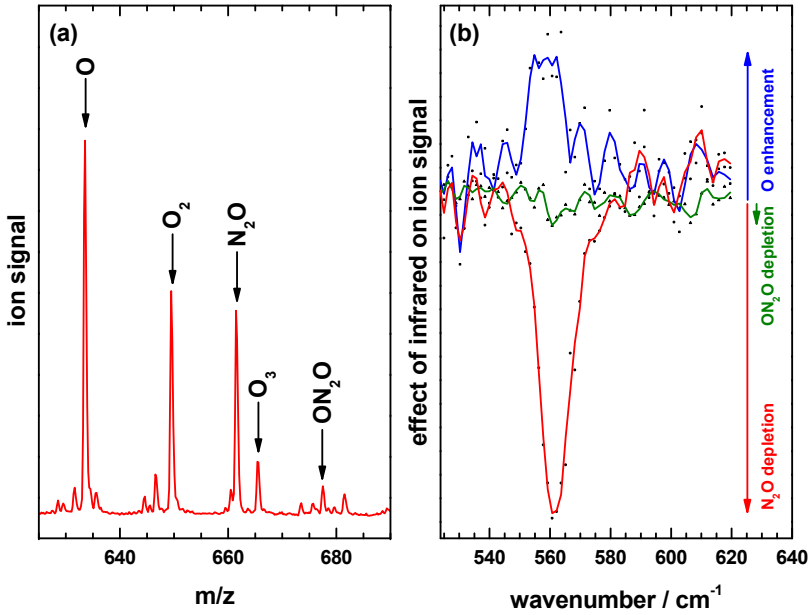


Figure 5.15: The Rh_6O^+ enhancement is not due to simple desorption of N_2O from $Rh_6ON_2O^+$. This species has relatively low abundance, as shown in the mass spectrum (a). Its absolute depletion is almost zero and cannot account for the total production of the monoxide (b).

ide enhancement are the $Rh_nN_2O^+$ clusters (Figure 5.16). The absorption wavenumbers of N_2O are the same as those measured in the argon-tagging experiments, implying that the cluster structure is unchanged when complexed without argon. This means that N_2O is still molecularly bound on the cluster surface, and must react to lose N_2 and form the oxide cluster.

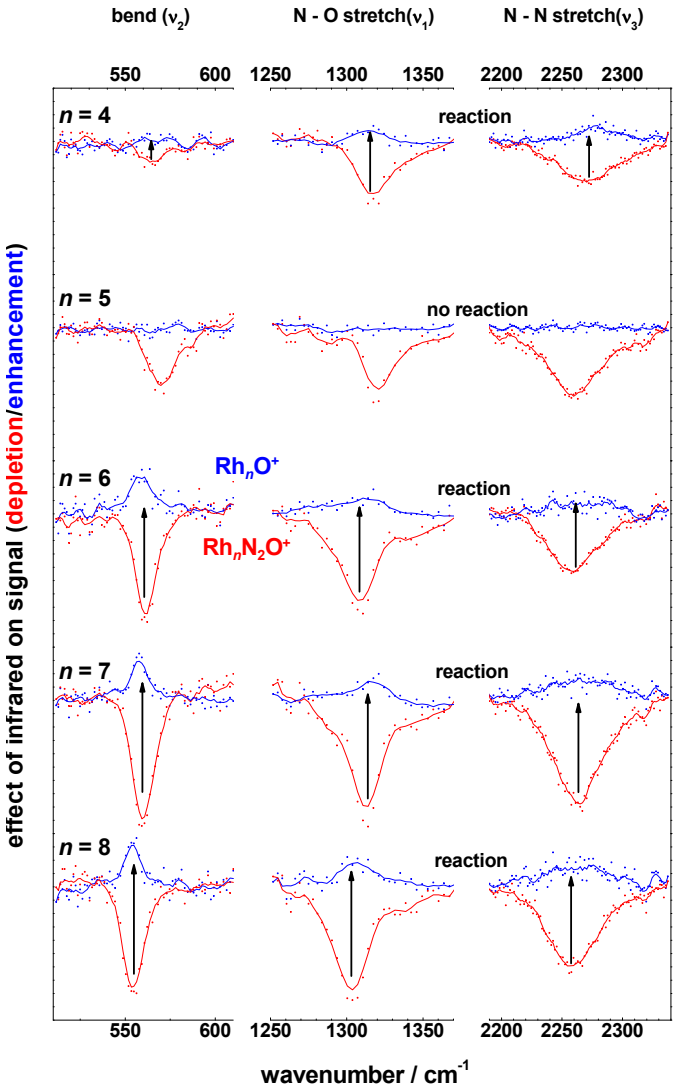


Figure 5.16: Infrared-induced reactivity on $Rh_nN_2O^+$ clusters with $n = 4-8$. Infrared absorption by the N_2O ligand results in a cluster surface reaction producing N_2 which desorbs, leaving the Rh_nO^+ fragment. All clusters except $n = 5$ exhibit N_2O decomposition, irrespective of the N_2O mode which is excited.

Branching ratios

With the exception of $n = 5$, all the $Rh_nN_2O^+$ clusters studied undergo N_2O decomposition after infrared absorption. The extent of reaction can be quantified by comparing

the enhancement of the monoxide cluster to the total depletion of the parent ion. The results of this are given in Table 5.2 for each of the N_2O modes.

Table 5.2: Reaction branching ratios calculated as Rh_nO^+ enhancement as a fraction of $Rh_nN_2O^+$ depletion. Each of these values is the average over several scans. Each scan shows the same qualitative depletion and enhancement, but variations between scans lead to uncertainties of around ±0.10 in each of these values.

n	ν_1	ν_2	ν_3
4	0.21	0.04	0.25
5	-0.07	-0.03	0.00
6	0.24	0.34	0.14
7	0.20	0.25	0.20
8	0.29	0.23	0.23

For the reactive clusters, the reaction channel only accounts for up to a third of the total $Rh_nN_2O^+$ depletion. The competing pathway is most likely N_2O loss, producing bare cluster ions. Unfortunately, this enhancement is too small to be detectable on top of the already large bare cluster signal, so this dissociation pathway cannot be confirmed.

N_2O decomposition is observed on all clusters except $n = 5$, consistent with the earlier results from the argon-tagging experiments. The $Rh_5N_2O^+$ cluster shows clear depletion for all N_2O modes, but there is no detectable oxide enhancement (Figure 5.16). The product of $Rh_5N_2O^+$ dissociation is not Rh_5O^+, but there must be a cationic species being produced to balance the loss of the N_2O complex. The most likely process is simple N_2O desorption to give bare Rh_5^+ clusters. As explained above, however, this channel cannot easily be measured because of the difficulty in detecting a small increase on a large background.

Low $Rh_5N_2O^+$ reactivity has been observed before, in FT-ICR single-collision experiments between rhodium cluster cations and N_2O.[5] Despite the differences in the reaction initiation – involving a collision step in FT-ICR, and starting from adsorbed N_2O in this experiment – the reactivities of these small rhodium clusters are strikingly similar.

Of the reactive clusters, there is almost no mode-dependence within the error of the measurements. Only ν_2 for $n = 4$ appears to be less reactive. This is in contrast with the

vibrationally mediated photodissociation observed on species such as V^+OCO, in which reactive and dissociative pathways are favoured depending on the excited vibrational mode.[322] Instead, the same photodissociation process appears to be occurring irrespective of the excited mode. This suggests that the N_2O decomposition process is thermal, and can occur when the absorption of any of the modes heats the cluster.

5.7.2 DFT reaction pathways

Since the spectroscopy of the adsorbed N_2O reveals that it is molecularly bound through the terminal N atom, the infrared-induced loss of N_2 must proceed *via* a pathway that brings the oxygen atom into contact with the surface and breaks the N-O bond. Possible mechanisms for this reaction have been investigated using DFT by calculating transition states and intermediate minima along the reaction pathways between N-bound N_2O and the oxide cluster after N_2 loss.

$Rh_6N_2O^+$ reaction pathways

The octahedral structure of Rh_6^+ is the best-established of these clusters, so it was used as the basis for calculation of a comprehensive search of the possible pathways for N_2O decomposition. The reaction pathways considered here were based on those previously calculated on clusters using PBE,[314] and those calculated on extended rhodium surfaces.[298]

Figures 5.17 and 5.18 summarise the converged reaction profiles calculated for the $Rh_6N_2O^+$ cluster in the TPSSh functional. The energies given in these figures are for clusters with spin multiplicity $2S + 1 = 8$, but the 10-tet profiles are qualitatively the same. All of the possible pathways are exothermic, but the energy of each transition state strongly depends on the N_2O interaction with the rhodium cluster. The binding energy of the N_2O is found to be 0.68 eV when bound through the N atom, but only

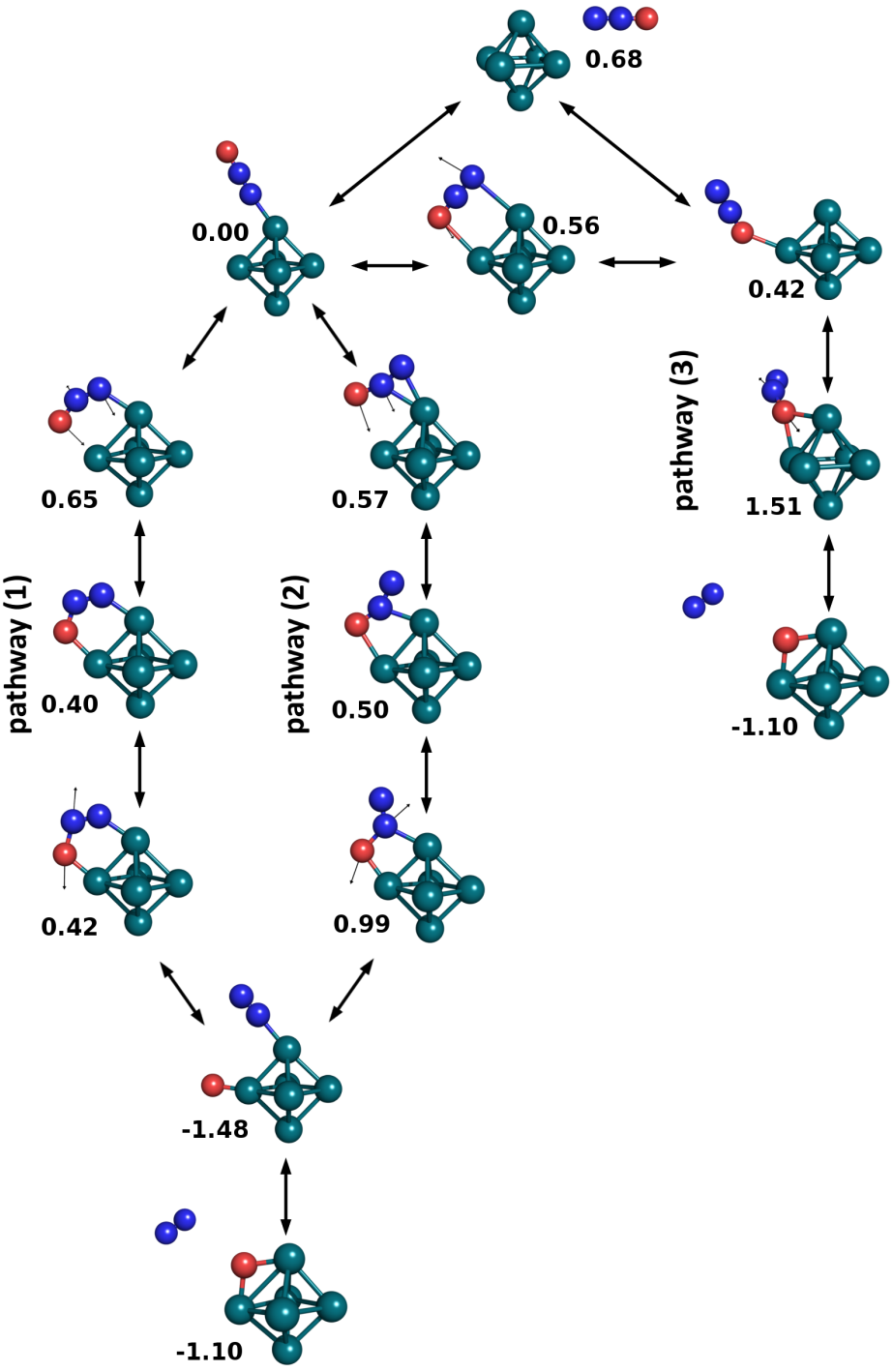


Figure 5.17: Dissociation pathways for N_2O on an octahedral Rh_6^+ cluster with $2S+1=8$. The relative energy of each structure is given in eV. For each transition state, the force vectors corresponding to the negative eigenvalue are plotted on the structure.

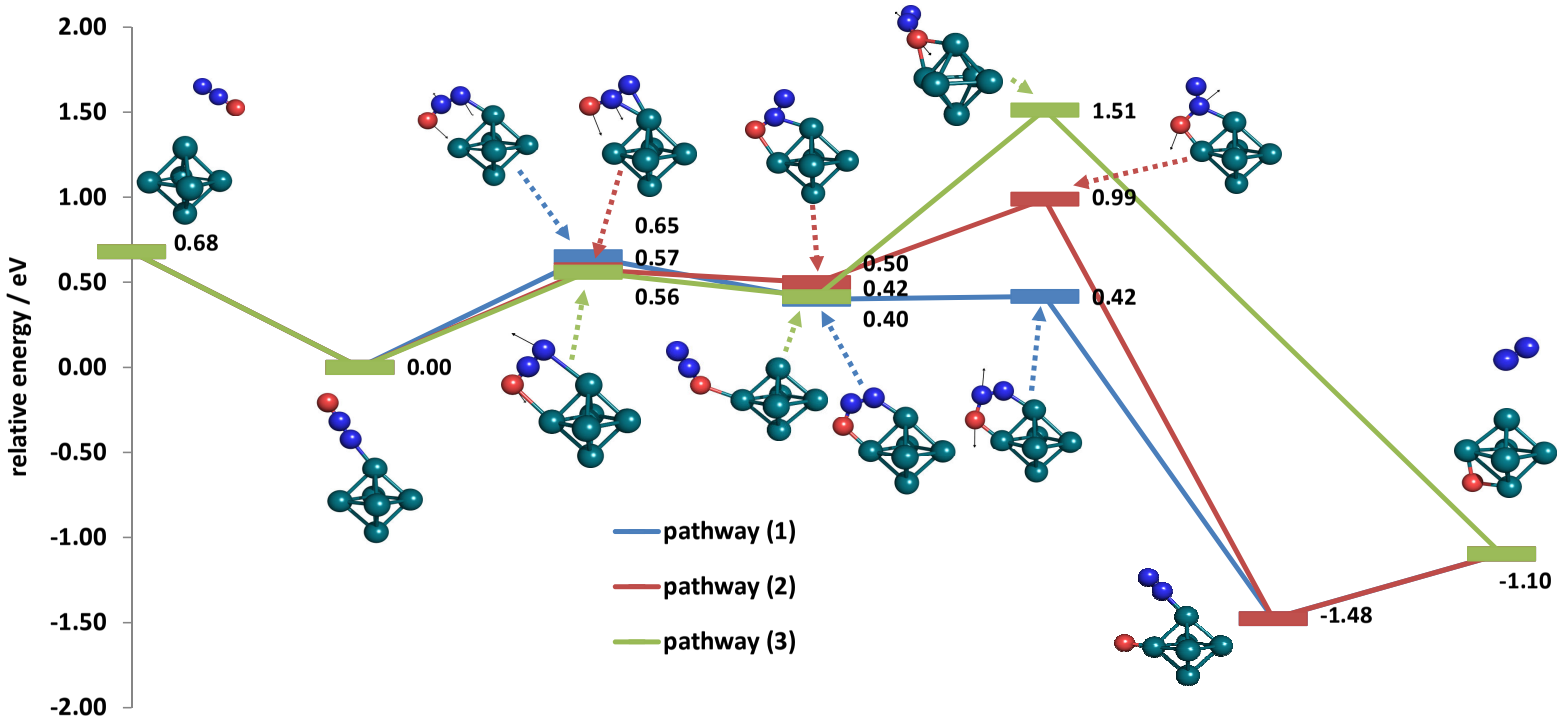


Figure 5.18: Dissociation pathways for N_2O on an octahedral Rh_6^+ cluster with $2S+1=8$. For each transition state, the force vectors corresponding to the negative eigenvalue are plotted on the structure. The pathways are labelled (1) to (3) based on the labels given in Figure 5.17.

0.26 eV when bound through the O atom. A relatively low-lying (0.56 eV) transition state can interconvert these two atop structures by turning the N_2O molecule along one of the edges of the octahedron.

Once the N_2O is bound by the oxygen atom, the N_2O can dissociate in a single step to form Rh_6O^+ and release N_2 (pathway (3)), but this requires overcoming a reaction barrier of 1.51 eV. Two lower-energy pathways are possible if the N_2O remains N-bound but swings around to bring another atom in contact with the rhodium cluster before N-O bond dissociation. If the N_2O bridges across a cluster edge so that it is bound by both terminal atoms (pathway (1)), the highest barrier to overcome is 0.65 eV, lower than the binding energy of the N_2O. A second pathway (pathway (2)), with a maximum barrier height of 0.99 eV, involves N_2O bridged by the O atom and the central N atom. In both pathways with bridged structures, the product with dissociated N_2O can lose N_2 to give the Rh_6O^+ product observed experimentally.

Because the transition states in the lowest energy pathway (pathway (1)) lie below the N_2O binding energy, this reaction can compete with the cluster-N_2O dissociation when the cluster is heated by infrared excitation, explaining why the reaction is observed in the IR-MPD experiments. Figure 5.19(a) gives the reaction profile for this pathway in the 8-tet and 10-tet spin multiplicities, showing that the transition states lie below the binding energy in both of these low-lying spin states. The 10-tet pathway differs slightly from the 8-tet: once the first transition state is overcome, in which the N_2O bends round to bring the O atom towards the cluster, the reaction proceeds to the dissociated geometry without any further intermediates or transition states.

For comparison, the same pathway calculated in PBE0 is shown in Figure 5.19(b). PBE0 finds intermediates and transition states with very similar structures to TPSSh, but the calculated energies imply that N_2O loss would be favoured rather than N_2O decomposition. Within the uncertainties of DFT, these two energies are equal, but the PBE0

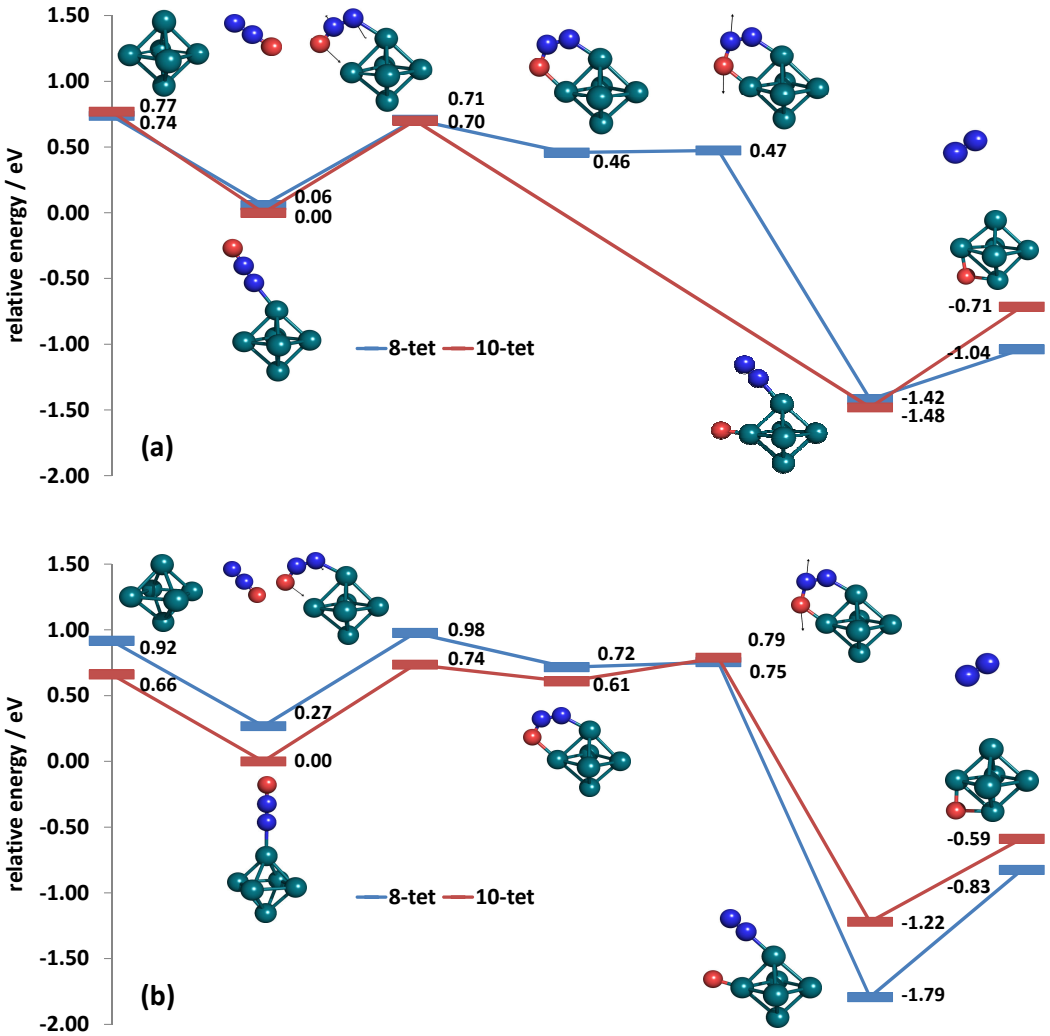


Figure 5.19: DFT reaction profile for the dissociation of N_2O on octahedral Rh_6^+ (pathway (1) in Figures 5.17 and 5.18), calculated with (a) the TPSSh functional and (b) the PBE0 functional. The two lowest-energy spin states are shown: $2S+1=8$ and 10. All energies are given in eV relative to the lowest-lying structure with molecularly adsorbed N_2O. The calculated structures are very similar in both functionals, but in TPSSh the reaction barriers all lie below the energy required to remove the N_2O molecule, while in PBE0 the reverse is true.

energies still disagree with the outcome of the experiment, which shows that the reaction does occur and hence the reaction barrier does lie lower than the N_2O dissociation energy.

$Rh_4N_2O^+$ reaction pathways

The tetrahedral Rh_4^+ cluster was used to calculate the equivalent reaction profile for $Rh_4N_2O^+$ (Figure 5.20). The same bridged intermediate and transition states are found

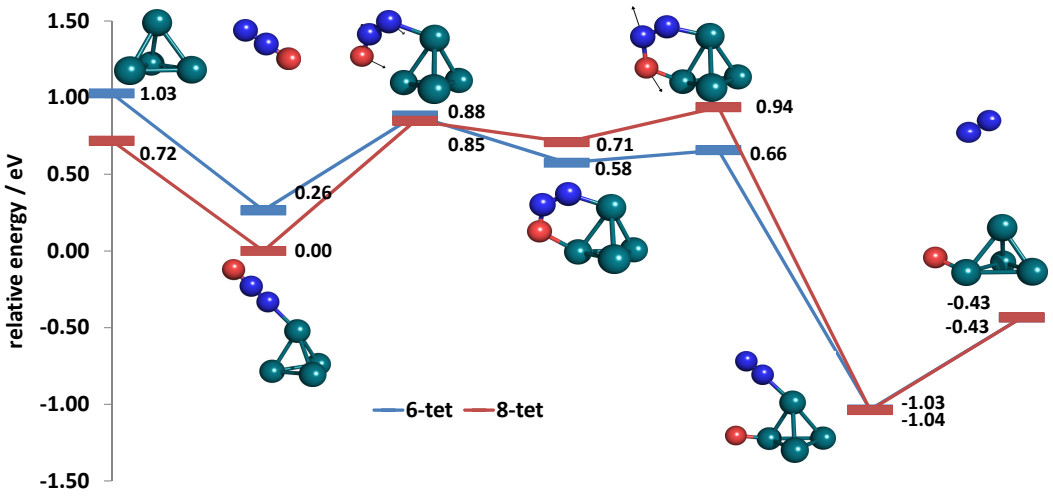


Figure 5.20: DFT reaction profile for the dissociation of N_2O on tetrahedral Rh_4^+, calculated with the TPSSh functional. The two lowest-energy spin states are shown: $2S+1=6$ and 8. All energies are given in eV relative to the lowest-lying structure with molecularly adsorbed N_2O.

for this cluster, but here the N_2O binding energy is 0.22 eV *lower* than the transition barrier. This cannot account for the $Rh_4N_2O^+$ reactivity observed experimentally.

Unlike $n=6$, however, there are qualitative differences in the barrier heights of the two lowest-lying spin isomers. When the reaction takes place on the 6-tet cluster, the barriers do lie below the N_2O binding energy. This suggests that the cluster's electronic structure may influence the energetics of the N_2O dissociation, and that at least some of the $Rh_4N_2O^+$ is present in the slightly higher energy 6-tet spin state.

$Rh_5N_2O^+$ reaction pathways

The clusters with $n=5$ were also investigated to try to explain their anomalously low reactivity. Because the IR-MPD structural assignment was inconclusive, reaction pathways were calculated on both the square-based pyramid and trigonal bipyramid structures.

Even restricting the calculations to the N_2O geometries of the $n=6$ calculation, involving N_2O bridged by the terminal atoms, there are still many non-equivalent pathways possible on these clusters, depending on which edge the molecule bridges. Figure 5.21 shows two of these pathways on the two cluster geometries. The results are similar

for both the square-based pyramid and the trigonal bipyramid: for the lowest-lying spin state ($2S+1=9$), the reaction barriers are higher than the N_2O binding energy, predicting that N_2O desorption is favoured over reaction. In the 7-tet multiplicity, the energies are reversed.

There is some geometry-dependence in the reaction barriers, which are higher on the square-based pyramid than on the trigonal bipyramid, but overall the electronic structure of the underlying cluster appears to have a stronger effect than the geometric structure.

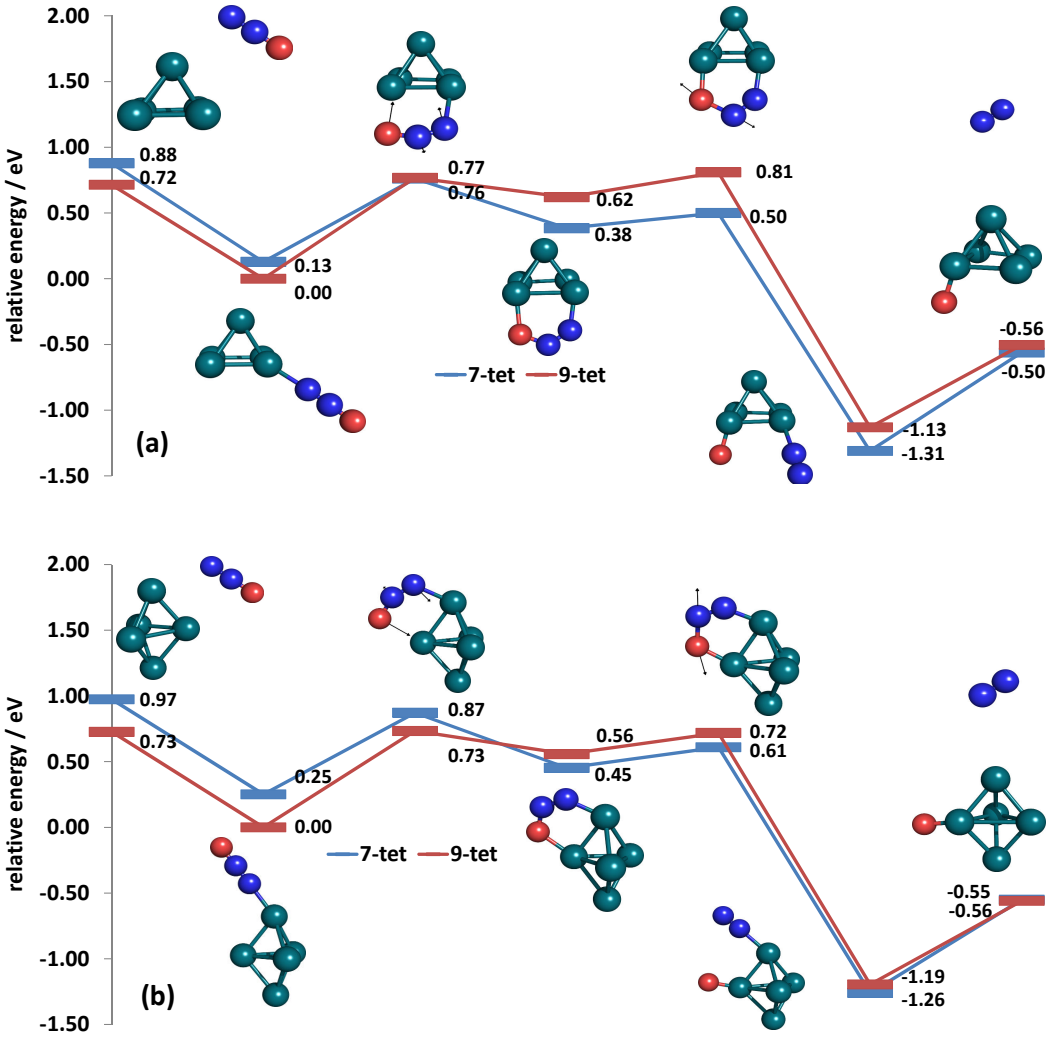


Figure 5.21: TPSSh reaction profile for the dissociation of N_2O on Rh_5^+, based on the trigonal bipyramid (a) and square pyramid (b). All energies are given in eV relative to the lowest-lying structure with molecularly adsorbed N_2O. In both geometries, the reaction pathway of lowest-spin isomer involves at least one barrier which is higher than the dissociation limit.

The result is the same for reaction pathways not shown in Figure 5.21, suggesting that the origin of the low reactivity Rh_5^+ is its electronic structure.

5.7.3 Discussion

The N_2O reaction observed on the cluster surfaces is analogous to that observed in temperature programmed desorption experiments on rhodium metal, in which N_2O also decomposes to N_2 and surface oxide. In calculations supporting these TPD experiments, the lowest energy pathway found by DFT calculations on rhodium surfaces is very similar to that found on the clusters, with nitrogen-bound N_2O rearranging to a bridged form before dissociation.[298]

The major difference between TPD and the cluster reaction is that the infrared must be absorbed by a chromophore in order to heat the cluster. The infrared heating induces the reaction, which has barrier heights that are calculated to lie in the range 0.6-0.7 eV. Overcoming these barriers requires several photons to be absorbed: 4, 9 or 3 if the absorbing mode is ν_1, ν_2 or ν_3, respectively. This is an absolute minimum number, since in practice not all of the absorbed energy will be transferred into the normal mode involved in the reaction, but is distributed amongst all vibrational degrees of freedom. This large number of absorbed photons is not unusual, as similar multiple-photon processes have been previously observed. For example, in the loss of H_2 from cationic vanadium clusters a minimum of 14 photons must be absorbed.[267]

The absorption of multiple photons is made possible by the high pulse energies produced by FELIX. Since the pulses are composed of short micropulses, the photon absorption is more likely to be sequential than coherent, with IVR redistributing the energy to the rest of the cluster between each photon absorption. IVR is known to be fast on the timescale of the experiments from the argon-tagging experiments, in which the argon is lost before the clusters are extracted by the mass spectrometer. This fast IVR also allows

enough photons to be absorbed to induce the N_2O reaction.

Furthermore, IVR and sequential photon absorption also explain why the reaction is apparently so mode-independent, with only small differences in the reaction branching ratio between different modes of the same cluster (Table 5.2). This is because the cluster can be heated above the reaction barrier regardless of which mode was originally excited. The same reaction is not observed at the wavenumbers of the far-infrared absorptions because this would require several times more photons to be absorbed by the weakly-absorbing cluster modes.

The DFT calculations predict the barrier to reaction to lie very close to the N_2O binding energy, irrespective of cluster size. These two processes represent competing pathways to dissociation once enough infrared photons have been absorbed. Even though TPSSh predicts a lower barrier to reaction than to N_2O loss, the experimental branching ratios suggest that only up to one third of the clusters undergo reaction. This is probably because the reaction involves a rearrangement of the N_2O on the cluster surface, requiring the oxygen atom to come into contact with the surface in a pseudo-bimolecular reaction. Once this has happened, a metastable intermediate is formed which can go on to dissociate and form the reaction products, but could also reverse and produce the original atop structure. In contrast, cluster-N_2O dissociation is unimolecular and essentially irreversible under the low-concentration conditions in the molecular beam. Despite the lower-energy reaction barriers, it is unsurprising that the majority of the clusters simply lose N_2O rather than undergo reaction.

5.8 Conclusions

IR-MPD has been applied to N_2O-complexed rhodium clusters to investigate their structures and infrared-induced reactions. Argon-tagging action spectroscopy was used to record the mid- and far-infrared spectra of $Rh_6N_2O^+$ for clusters with $4 \leq n \leq 8$. The

absorption frequencies of the N_2O identified it as being molecularly adsorbed on the surface of each cluster, bound in an atop geometry through the terminal N atom. The far-infrared spectra of the rhodium cluster modes provided tentative assignments for some cluster geometries: a trigonal bipyramid, octahedron, and bicapped octahedron for $n = 5, 6$ and 8.

Unexpectedly, heating the clusters through the N_2O modes is observed to induce reactions on the clusters, causing the N_2O to dissociate, leaving partially oxidised clusters Rh_nO^+ and releasing molecular nitrogen. This process is thermally-driven, analogous to surface TPD, with each of the N_2O modes absorbing infrared when resonant with the mode, and heating the cluster by IVR to drive the reaction over the transition barrier. These reactions are believed to be the first observed infrared-driven reactions on cluster surfaces. The reaction pathway determined by DFT calculations involves the N_2O rearranging into a bridged structure which has a lower barrier to dissociation than when the molecule is bound atop.

Of the cluster sizes studied, only $Rh_5N_2O^+$ is unreactive. Although its IR-MPD spectrum indicates the presence of molecularly adsorbed N_2O, it is not observed to dissociate to produce Rh_5O^+. Calculations of reaction pathways suggest that the there are several possible pathways depending on the original geometry of the cluster, but that the lowest-energy spin state has a reaction barrier which is larger than the N_2O binding energy. This suggests that all of the observed $Rh_5N_2O^+$ depletion is caused by N_2O loss.

Comparisons of the calculations performed in two different hybrid density functionals, TPSSh (10 % HF exchange) and PBE0 (25 % HF exchange) were performed because of the known difficulties in accurately calculating the properties of rhodium clusters. PBE0, which has previously been found to perform well for bare rhodium clusters,[258,259] performed better than TPSSh in calculating the spectra of the N_2O modes, correctly predicting the shifts on the absorption frequencies induced by the clusters. The transition

states for N_2O dissociation, however, were calculated by PBE0 to lie higher than the N_2O binding energy, which cannot explain the reactions observed in IR-MPD. TPSSh, on the other hand, does find reaction pathways which are consistent with experiment, with transition states lower in energy than the N_2O binding energy. Neither functional is fully satisfactory for the calculation of both minima and transition states, but TPSSh is probably the better compromise for finding the true minima geometries while also explaining the experimental reactivities.

Future work

The observation of these reactions opens up the possibility of using infrared radiation to induce more complex reactions, such as a whole catalytic cycle with N_2O and CO. We plan to return to the FELIX facility early in 2011 to run a similar experiment on platinum clusters with coadsorbed CO molecules and O atoms to try to induce a CO oxidation reaction by infrared absorption, either through the C-O stretch absorption or a cluster-oxide mode.

The difficulty in interpreting the $Rh_nN_2O^+$ reactions highlights the challenges in applying DFT to transition metals, especially clusters, when the functionals are usually optimised for main group chemistry or atomic and solid properties. More work is needed on developing functionals suited to these systems, and understanding why Hartree-Fock exchange has such a large effect on the structures and transition state energies of rhodium clusters.

Chapter 6

Conclusions and outlook

This project has involved the application of a wide range of experimental techniques for investigating the physical and chemical properties of small transition metal clusters. These include laser vapourisation cluster sources, time-of-flight mass spectrometry, photoionisation, infrared multiple photon dissociation and velocity map imaging. It has involved technique and instrument-development, both laboratory and national facility-based experiments and a significant fraction of computational work to help interpret the results obtained.

Chapter 2 describes a new instrument for photodissociation and photoionisation experiments of transition metal clusters. It comprises a newly-designed laser vapourisation source, loosely based on the design of Bondybey *et al.*,[138] and a home-built time-of-flight mass spectrometer. The latter was first simulated to optimise the dimensions of the electrodes in order to achieve Wiley-McLaren first-order focusing.[41] The electrodes can be pulsed or held at a DC potential in order to investigate ionic and neutral clusters, respectively. After essential characterisation using the spectroscopy of NO, neutral and cationic vanadium oxide clusters were produced by the cluster source and detected by the mass spectrometer, confirming that the source can be used to generate metal clusters with

good intensity up to around $n = 10$.

The ToF instrument was first applied to record the spectrum of the astrophysically-important vanadium monoxide molecule in the visible region of the spectrum (Chapter 3). Broadband (1+2) and (1+1′) REMPI spectra reveal an intense vibrational progression assignable to eight bands of the $C\,^4\Sigma^- - X\,^4\Sigma^-$ transition. Repeating these spectra at higher-resolution confirmed the assignment and allowed the band origins and rotational constants to be determined. The $(4, 0)$ band of the $B\,^4\Pi - X\,^4\Sigma^-$ transition was also recorded with rotational resolution in each of its four spin-orbit components.

In addition to the previously-observed $C - X$ and $B - X$ transitions, two new, formally spin-forbidden transitions were recorded in high-resolution REMPI, from the ground state to the $2\,^2\Pi$ and $3\,^2\Pi$ states. The former was identified as a $^2\Pi$ state arising from the $\sigma\delta\pi$ configuration, on the basis of its spin-orbit coupling constant and the rotational constant, which agrees with that of the $2\,^2\Pi$ state observed in emission spectroscopy.[158] This assignment allows the energies of the quartet manifold to be connected, for the first time, to the six known doublet states of VO. The upper state of the other spin-forbidden transition is assigned to a new $^2\Pi$ state arising from the $\delta^2\sigma$ configuration.

Higher-resolution spectra are required to confirm the assignment of these new $2\,^2\Pi - X\,^4\Sigma^-$ and $3\,^2\Pi - X\,^4\Sigma^-$ bands. This could be achieved by repeating the spectra with a lower-bandwidth pulse-amplified ring dye laser. There are also additional bands in the broadband spectrum which could not be identified here. Since they could not be assigned to any of the previously observed states, their assignment should lead to a better understanding of the electronic structure of VO.

Photoionisation spectroscopy has also been applied to the Au_2 molecule (Chapter 4). Its REMPI spectrum is weak in the region studied due to the competition with dissociation. The photodissociation spectrum of Au_2 was recorded at the two-photon level between 35500 and 37200 cm^{-1}. A dense spectrum of overlapping vibrational progres-

sions, much less clear than the REMPI spectra previously observed in the visible spectral region,[67] was observed in both the Au_2 and Au channel. Four vibrational progressions are observed, leading up to their respective dissociation limits, including two arising from vibrationally hot Au_2.

Velocity map images, recorded on 54 features across the Au_2 spectrum, reveal the nature of the atomic Au photodissociation fragments. Although Au products are detected in a total of 13 of the 16 energetically accessible product channels within detectable range, not all of these products are observed in every image: product channels open and close across the spectral region. From this we can infer the presence of dissociative curve crossings of the excited states. These excited states are deduced to be of 0_g^+ symmetry from the angular distribution of the Au fragments.

When photodissociated by a single photon at 157 nm, Au_2 fragments into ground and excited state gold atoms, whose states are determined by velocity map imaging. The seven highest-energy fragment channels were observed, out of the nine energetically-accessible channels. A second ionisation laser, tuned to a REMPI channel of excited $^2D_{5/2}$ Au, confirmed this assignment. Calculating the potential energy curves of excited states of Au_2 is a challenge for theory, given the large number of electrons and the relativistic effects involved in Au bonding, but excited state calculations are essential for a better understanding of the Au_2 dissociation observed in these experiments.

Dissociation of larger clusters is considered in Chapter 5, which describes experiments performed at the FELIX free electron laser facility, involving infrared multiple-photon dissociation experiments on rhodium clusters complexed with N_2O. Spectra of the argon-tagged $Rh_nN_2O^+$ complexes using the inert messenger atom technique were recorded which, by comparison with calculated spectra, yield information of the nature of the binding and the electronic and geometrical structure of the complexes. Strong absorptions consistent with molecularly adsorbed N_2O are observed in the mid-infrared

spectrum of all of the cluster sizes studied. The shifts from free N_2O are indicative of N_2O bound through the terminal N atom, as is observed on transition metal surfaces.[295,297] Far-infrared spectra of the metal cluster modes allowed a tentative assignment to be made of the underlying cluster geometries.

The unexpected observation of infrared-induced decomposition of N_2O on the surface of the cluster was interpreted as a thermal process caused by the clusters being heated by resonant infrared absorption, analogous to the temperature-programmed desorption of N_2 from N_2O on rhodium surfaces.[289,290] This cluster surface reaction occurs on all the cluster sizes studied with the exception of $n = 5$, whose low reactivity was previously observed in FT-ICR experiments.[5]

Density functional theory calculations of the $Rh_nN_2O^+$ structures were carried out in order to compare the experimental spectra with theoretical predictions, and to find reaction pathways for the N_2O decomposition. Two hybrid functionals, containing a fraction of Hartree-Fock exchange, were used because previous work on rhodium clusters had concluded that HF exchange is needed to calculated the correct global minimum.[258,259] The two functionals used in this chapter, TPSSh (10 % HF exchange) and PBE0 (25 % HF exchange) predict qualitatively similar low-lying isomers and reaction pathways. PBE0 performs better than TPSSh when calculating the infrared spectra of the N_2O modes, but predicts reaction transition states which are inconsistent with the experimentally observed reactivity. The TPSSh reaction barriers, however, lie lower than the N_2O dissociation energy, in better agreement with experiment. More work is needed to understand why the exact fraction of HF exchange in density functionals appears to be so essential in the treatment of metal clusters.

There are many other reactions which are observed on metal surfaces that could conceivably be induced on clusters in the way N_2O is decomposed in this study. For example, the intense absorption of the CO stretch could be used as a chromophore to

heat a cluster and induce CO oxidation by adsorbed oxygen. We plan to return to FELIX in early 2011 to attempt this infrared-induced reaction on platinum clusters, since the oxidation of CO occurs on commercial platinum catalytic converters. If the reaction is indeed thermal, it should also be possible to heat the cluster through a platinum-oxygen mode to produce the same reaction products.

This project has studied three metal cluster systems using several mass spectrometry-based techniques, applying laser spectroscopy from the far-infrared to the vacuum-ultraviolet regions of the spectrum. Investigating the geometric and electronic structure of clusters is challenging, but these experiments demonstrate how photoionisation and photodissociation spectroscopy can be used to determine the underlying structure and, in the case of rhodium clusters, to reveal how this structure is related to reactivity. The results obtained here also highlight the need for the development of computational techniques which are better suited to treating the complexities that make this state of matter so fascinating.

Bibliography

[1] Armentrout, P. B. *Annu. Rev. Phys. Chem.* **52**, 423–461 (2001).

[2] Mitchell, S. A., Lian, L., Rayner, D. M., and Hackett, P. A. *J. Chem. Phys.* **103**, 5539–5547 (1995).

[3] Tiggesbäumer, J., Köller, L., Lutz, H. O., and Meiwes-Broer, K. H. *Chem. Phys. Lett.* **190**, 42–47 (1992).

[4] Elkind, J. L., Weiss, F. D., Alford, J. M., Laaksonen, R. T., and Smalley, R. E. *J. Chem. Phys.* **88**, 5215–5224 (1988).

[5] Harding, D., Ford, M. S., Walsh, T. R., and Mackenzie, S. R. *Phys. Chem. Chem. Phys.* **9**, 2130–2136 (2007).

[6] Bérces, A., Hackett, P. A., Lian, L., Mitchell, S. A., and Rayner, D. M. *J. Chem. Phys.* **108**, 5476–5490 (1998).

[7] DeLouise, L. A. and Winograd, N. *Surf. Sci.* **159**, 199–213 (1985).

[8] Foster, P. J., Leckenby, R. E., and Robbins, E. J. *J. Phys. B* **2**, 478–483 (1969).

[9] de Heer, W. A. *Rev. Mod. Phys.* **65**, 611–676 (1993).

[10] Larsen, R. A., Neoh, S. K., and Herschbach, D. R. *Rev. Sci. Instrum.* **45**, 1511–1516 (1974).

[11] Kappes, M. M., Kunz, R. W., and Schumacher, E. *Chem. Phys. Lett.* **91**, 413–418 (1982).

[12] Katakuse, I., Ichihara, T., Fujita, Y., Matsuo, T., Sakurai, T., and Matsuda, H. *Int. J. Mass. Spectrom. Ion Processes* **67**, 229–236 (1985).

[13] Haberland, H., Mall, M., Moseler, M., Qiang, Y., Reiners, T., and Thurner, Y. *J. Vac. Sci. Technol. A* **12**, 2925–2930 (1994).

[14] Lincoln, K. A. *Int. J. Mass. Spectrom. Ion Phys.* **2**, 75–83 (1969).

[15] Dietz, T. G., Duncan, M. A., Powers, D. E., and Smalley, R. E. *J. Chem. Phys.* **74**, 6511–6512 (1981).

[16] Bondybey, V. E. and English, J. H. *J. Chem. Phys.* **74**, 6978–6979 (1981).

[17] Hopkins, J. B., Langridge-Smith, P. R. R., Morse, M. D., and Smalley, R. E. *J. Chem. Phys.* **78**, 1627–1637 (1983).

[18] Fielicke, A., Kirilyuk, A., Ratsch, C., Behler, J., Scheffler, M., von Helden, G., and Meijer, G. *Phys. Rev. Lett.* **93**, 023401 (2004).

[19] Maruyama, S., Anderson, L. R., and Smalley, R. E. *Rev. Sci. Instrum.* **61**, 3686–3693 (1990).

[20] Cha, C.-Y., Ganteför, G., and Eberhardt, W. *Rev. Sci. Instrum.* **63**, 5661–5666 (1992).

[21] Ganteför, G., Siekmann, H. R., Lutz, H. O., and Meiwes-Broer, K. H. *Chem. Phys. Lett.* **165**, 293–296 (1990).

[22] Kraus, D., Saykally, R. J., and Bondybey, V. E. *Chem. Phys.* **247**, 431–434 (1999).

[23] Rohlfing, E. A. and Valentini, J. J. *Chem. Phys. Lett.* **126**, 113–118 (1986).

[24] Knight, W. D., Clemenger, K., de Heer, W. A., Saunders, W. A., Chou, M. Y., and Cohen, M. L. *Phys. Rev. Lett.* **52**, 2141–2143 (1984).

[25] Martin, T. P., Bergmann, T., Göhlich, H., and Lange, T. *Chem. Phys. Lett.* **176**, 343–347 (1991).

[26] Honea, E. C., Homer, M. L., Persson, J. L., and Whetten, R. L. *Chem. Phys. Lett.* **171**, 147–154 (1990).

[27] Parks, E. K., Winter, B. J., Klots, T. D., and Riley, S. J. *J. Chem. Phys.* **94**, 1882–1902 (1991).

[28] Riley, S. J. *J. Non-Crystalline Solids* **205–207**, 781–787 (1996).

[29] Parks, E. K., Weiller, B. H., Bechthold, P. S., Hoffman, W. F., Neiman, G. C., Pobo, L. G., and Riley, S. J. *J. Chem. Phys.* **88**, 1622–1632 (1988).

[30] Parks, E. K., Zhu, L., Ho, J., and Riley, S. J. *J. Chem. Phys.* **102**, 7377–7389 (1995).

[31] Weis, P., Gilb, S., Gerhardt, P., and Kappes, M. M. *Int. J. Mass. Spectrom.* **216**, 59–73 (2002).

[32] Weis, P., Bierweiler, T., Gilb, S., and Kappes, M. M. *Chem. Phys. Lett.* **355**, 355–364 (2002).

[33] Gilb, S., Weis, P., Furche, F., Ahlrichs, R., and Kappes, M. M. *J. Chem. Phys.* **116**, 4094–4101 (2002).

[34] Weis, P., Bierweiler, T., Vollmer, E., and Kappes, M. M. *J. Chem. Phys.* **117**, 9293–9297 (2002).

[35] Maier-Borst, M., Douglas B. Cameron, Rokni, M., and Parks, J. H. *Phys. Rev. A* **59**, R3162–R3165 (1999).

[36] Blom, M. N., Schooss, D., Stairs, J. R., and Kappes, M. M. *J. Chem. Phys.* **124**, 244308 (2006).

[37] Lechtken, A., Schooss, D., Stairs, J. R., Blom, M. N., Furche, F., Morgner, N., Kostko, O., von Issendorff, B., and Kappes, M. M. *Angew. Chem. Int. Ed.* **46**, 2944–2948 (2007).

[38] Schooss, D., Blom, M. N., Parks, J. H., von Issendorff, B., Haberland, H., and Kappes, M. M. *Nano Lett.* **5**, 1972–1977 (2005).

[39] Walther, C., Becker, S., Dietrich, G., Kluge, H.-J., Lindinger, M., and Lützenkirchen and L. Schweikhard and J. Ziegler, K. *Z. Phys. D* **38**, 51–58 (1996).

[40] Lindinger, M., Dasgupta, K., Dietrich, G., Krückeberg, S., Kuznetsov, S., and Lützenkirchen and L. Schweikhard and C. Walther and J. Ziegler, K. *Z. Phys. D* **40** (1997).

[41] Wiley, W. C. and McLaren, I. H. *Rev. Sci. Instrum.* **26**, 1150–1157 (1955).

[42] Fielicke, A., von Helden, G., Meijer, G., Pedersen, D. B., Simard, B., and Rayner, D. M. *J. Phys. Chem. B* **108**, 14591–14598 (2004).

[43] Boesl, U., Neusser, H. J., Winkauf, R., and Schlag, E. W. *J. Phys. Chem.* **86**, 4857–4863 (1982).

[44] LaiHing, K., Cheng, P. Y., Taylor, T. G., Willey, K. F., Peshke, M., and Duncan, M. A. *Anal. Chem.* **61**, 1458–1460 (1989).

[45] Willey, K. F., Cheng, P. Y., Bishop, M. B., and Duncan, M. A. *J. Am. Chem. Soc.* **113**, 4721–4728 (1991).

[46] de Heer, W. A., Selby, K., Kresin, V., Masui, J., Vollmer, M., Châtelain, A., and Knight, W. D. *Phys. Rev. Lett.* **59**, 1805–1808 (1987).

[47] Jarrold, M. F., Ray, U., Bower, J. E., and Creegan, K. M. *J. Chem. Soc. Faraday Trans.* **86**, 2537–2543 (1990).

[48] Fielicke, A., von Helden, G., Meijer, G., Simard, B., Dénommée, S., and Rayner, D. M. *J. Am. Chem. Soc.* **125**, 11184–11185 (2003).

[49] Jaeger, T. D., Fielicke, A., von Helden, G., Meijer, G., and Duncan, M. A. *Chem. Phys. Lett.* **392**, 409–414 (2004).

[50] Inoue, K., Ohashi, K., Iino, T., Judai, K., Nishi, N., and Sekiya, H. *Phys. Chem. Chem. Phys.* **9**, 4793–4802 (2007).

[51] Salter, T. E., Mikhailov, V., and Ellis, A. M. *J. Phys. Chem. A.* **111**, 8344–8351 (2007).

[52] Schweizer, A., Weber, J. M., Gilb, S., Schneider, H., Schooss, D., and Kappes, M. M. *J. Chem. Phys.* **119**, 3699–3710 (2003).

[53] Fielicke, A., Rabin, I., and Meijer, G. *J. Phys. Chem. A* **110**, 8060–8063 (2006).

[54] Gehrke, R., Gruene, P., Fielicke, A., Meijer, G., and Reuter, K. *J. Chem. Phys.* **130**, 034306 (2009).

[55] Fielicke, A., Ratsch, C., von Helden, G., and Meijer, G. *J. Chem. Phys.* **127**, 234306 (2007).

[56] Iino, T., Ohashi, K., Inoue, K., Judai, K., Nishi, N., and Sekiya, H. *J. Chem. Phys.* **126**, 194302 (2007).

[57] Walker, N. R., Walters, R. S., Pillai, E. D., and Duncan, M. A. *J. Chem. Phys.* **119**, 10471–10474 (2003).

[58] Walker, N. R., Walters, R. S., Tsai, M.-K., Jordan, K. D., and Duncan, M. A. *J. Phys. Chem. A* **109**, 7057–7067 (2005).

[59] Rohlfing, E. A., Cox, D. M., and Kaldor, A. *Chem. Phys. Lett.* **99**, 161–166 (1983).

[60] Whetten, R. L., Zakin, M. R., Cox, D. M., Trevor, D. J., and Kaldor, A. *J. Chem. Phys.* **85**, 1697–1698 (1986).

[61] Yang, S. and Knickelbein, M. B. *Chem. Phys. Lett.* **99**, 161–166 (1983).

[62] Knickelbein, M. B. and Yang, S. *J. Chem. Phys.* **93**, 5760–5767 (1990).

[63] Collings, B. A., Rayner, D. M., and Hackett, P. A. *Int. J. Mass. Spectrom. Ion Processes* **125**, 207–214 (1993).

[64] Kappes, M. M., Schär, M., Röthlisberger, U., Yeretzian, C., and Schumacher, E. *Chem. Phys. Lett.* **143**, 251–258 (1988).

[65] Knickelbein, M. B. *Chem. Phys. Lett.* **192**, 129–134 (1992).

[66] Alameddin, G., Hunter, J., Cameron, D., and Kappes, M. M. *Chem. Phys. Lett.* **192**, 122–128 (1992).

[67] Bishea, G. A. and Morse, M. D. *J. Chem. Phys.* **95**, 5646–5659 (1991).

[68] Morse, M. D., Hansen, G. P., Langridge-Smith, P. R. R., Zheng, L.-S., Geusic, M. E., Michalopoulos, D. L., and Smalley, R. E. *J. Chem. Phys.* **80**, 5400–5405 (1984).

[69] Yeh, C. S., Robbins, D. L., Pilgrim, J. S., and Duncan, M. A. *Chem. Phys. Lett.* **206**, 509–514 (1993).

[70] Spain, E. M. and Morse, M. D. *J. Chem. Phys.* **97**, 4605–4615 (1992).

[71] Bishea, G. A. and Morse, M. D. *J. Chem. Phys.* **95**, 8779–8792 (1991).

[72] Pinegar, J. C., Langenberg, J. D., and Morse, M. D. *Chem. Phys. Lett.* **212**, 458–462 (1993).

[73] Bishea, G. A., Arrington, C. A., Behm, J. M., and Morse, M. D. *J. Chem. Phys.* **95**, 8765–8778 (1991).

[74] Yang, D.-S., James, A. M., Rayner, D. M., and Hackett, P. A. *J. Chem. Phys.* **102**, 3129–3134 (1995).

[75] Németh, G. I., Ungar, H., Yeretzian, C., Selzle, H. L., and Schlag, E. W. *Chem. Phys. Lett.* **228**, 1–8 (1994).

[76] Yang, D.-S., Zgierski, M. Z., Rayner, D. M., Hackett, P. A., Martinez, A., Salahub, D. R., Roy, P.-N., and Carrington, Jr., T. *J. Chem. Phys.* **103**, 5335–5342 (1995).

[77] Yang, D.-S., Zgierski, M. Z., and Hackett, P. A. *J. Chem. Phys.* **108**, 3591–3597 (1998).

[78] Yang, D.-S. and Hackett, P. A. *J. Electron Spectrosc. Relat. Phenom.* **106**, 153–169 (2000).

[79] Yang, D.-S., James, A. M., Rayner, D. M., and Hackett, P. A. *Chem. Phys. Lett.* **231**, 177–182 (1994).

[80] Ford, M. S. and Mackenzie, S. R. *J. Chem. Phys.* **123**, 084308 (2005).

[81] Zhang, L.-S., Brucat, P. J., Pettiette, C. L., Yang, S., and Smalley, R. E. *J. Chem. Phys.* **83**, 4273–4274 (1985).

[82] Taylor, K. J., Pettiette-Hall, C. L., Cheshnovsky, O., and Smalley, R. E. *J. Chem. Phys.* **96**, 3319–3329 (1992).

[83] Zhai, H.-J. and Wang, L.-S. *Chem. Phys. Lett.* **500**, 185–195 (2010).

[84] Huang, W., Pal, R., Wang, L.-M., Zeng, X. C., and Wang, L.-S. *J. Chem. Phys.* **132**, 054305 (2010).

[85] Bartels, C., Hock, C., Huwer, J., Kuhnen, R., Schwöbel, J., and von Issendorff, B. *Science* **323**, 1323–1327 (2009).

[86] Bragg, A. E., Verlet, J. R. R., Kammrath, A., Cheshnovsky, O., and Neumark, D. M. *J. Chem. Phys.* **122**, 054314 (2005).

[87] Wu, X., Qin, Z., Xie, H., Cong, R., Wu, X., Tang, Z., and Fan, H. *J. Chem. Phys.* **133**, 044303 (2010).

[88] Balaj, O. P., Balteanu, I., Roßteuscher, T. T. J., Beyer, M. K., and Bondybey, V. E. *Angew. Chem. Int. Ed.* **43**, 6519–6522 (2004).

[89] Anderson, M. L., Ford, M. S., Derrick, P. J., Drewello, T., Woodruff, D. P., and Mackenzie, S. R. *J. Phys. Chem. A* **110**, 10992–11000 (2006).

[90] Irion, M. P. and Schnabel, P. *J. Phys. Chem.* **95**, 10596–10599 (1991).

[91] Hanmura, T., Ichihashi, M., and Kondow, T. *J. Phys. Chem. A* **106**, 11465–11469 (2002).

[92] Hanmura, T., Ichihashi, M., and Kondow, T. *J. Phys. Chem. A* **106**, 4525–4528 (2002).

[93] Conceição, J., Liyanage, R., and Armentrout, P. B. *Chem. Phys.* **262**, 115–130 (2000).

[94] Liu, F., Li, M., Tan, L., and Armentrout, P. B. *J. Chem. Phys.* **128**, 194313 (2008).

[95] Liyanage, R., Conceição, J., and Armentrout, P. B. *J. Chem. Phys.* **116**, 936–945 (2002).

[96] Geusic, M. E., Morse, M. D., O'Brien, S. C., and Smalley, R. E. *Int. J. Mass. Spectrom. Ion Processes* **56**, 2123–2130 (1985).

[97] Haruta, M., Yamada, N., Kobayashi, T., and Iijima, S. *J. Catal.* **115**, 301–309 (1989).

[98] Balteanu, I., Balaj, O. P., Beyer, M. K., and Bondybey, V. E. *Int. J. Mass. Spectrom.* **255–256**, 71–75 (2006).

[99] Richtsmeier, S. C., Parks, E. K., Liu, K., Pobo, L. G., and Riley, S. J. *J. Chem. Phys.* **82**, 3659–2665 (1985).

[100] Øiestad, Å. M. L. and Uggerud, E. *Chem. Phys.* **262**, 169–177 (2000).

[101] Mitchell, S. A., Rayner, D. M., Bartlett, T., and Hackett, P. A. *J. Chem. Phys.* **104**, 4012–4018 (1996).

[102] Lee, T. H. and Ervin, K. M. *J. Chem. Phys.* **98**, 10023–10031 (1994).

[103] Winter, B. J., Parks, E. K., and Riley, S. J. *J. Chem. Phys.* **94**, 8618–8621 (1991).

[104] Cox, D. M., Brickman, R., Creegan, K., and Kaldor, A. *Z. Phys. D* **19**, 353–355 (1991).

[105] Balteanu, I., Achatz, U., Balaj, O. P., Fox, B. S., Beyer, M. K., and Bondybey, V. E. *Int. J. Mass. Spectrom.* **229**, 61–65 (2003).

[106] Ford, M. S., Anderson, M. L., Barrow, M. P., Woodruff, D. P., Drewello, T., Derrick, P. J., and Mackenzie, S. R. *Phys. Chem. Chem. Phys.* **123**, 975–980 (2005).

[107] Johnston, R. L. *Atomic and molecular clusters*, chapter 4. Taylor & Francis (2002).

[108] Majumdar, D. and Balasubrmanian, K. *J. Chem. Phys.* **108**, 2495–2503 (1998).

[109] Majumdar, D. and Balasubramanian, K. *J. Chem. Phys.* **115**, 885–898 (2001).

[110] Zaleski-Ejgierd, P. and Pyykkö, P. *J. Phys. Chem. A* **113**, 12380–12385 (2009).

[111] Cramer, C. J. and Truhlar, D. G. *Phys. Chem. Chem. Phys.* **11**, 10757–10816 (2009).

[112] Hohenberg, P. and Kohn, W. *Phys. Rev.* **136**, B864–B871 (1964).

[113] Jensen, F. *Introduction to Computational Chemistry*, chapter 6. John Wiley & Sons (2007).

[114] Perdew, J. P. and Wang, Y. *Phys. Rev. B* **45**, 13244–13249 (1992).

[115] Lee, C., Yang, W., and Parr, R. G. *Phys. Rev. B* **37**, 785–789 (1988).

[116] Perdew, J. P., Burke, K., and Ernzerhof, M. *Phys. Rev. Lett* **77**, 3865–3868 (1996).

[117] Voorhis, T. V. and Scuseria, G. E. *J. Chem. Phys.* **109**, 400–410 (1998).

[118] Tao, J., Perdew, J. P., Staroverov, V. N., and Scuseria, G. E. *Phys. Rev. Lett.* **91**, 146401 (2003).

[119] Becke, A. D. *J. Chem. Phys.* **98**, 5648–5652 (1993).

[120] Stephens, P. J., Devlin, F. J., Chabalowski, C. F., and Frisch, M. J. *J. Phys. Chem.* **98**, 11623–11627 (1994).

[121] Sousa, S. F., Fernandes, P. A., and Ramos, M. J. *J. Phys. Chem. A* **111**, 10439–10452 (2007).

[122] Perdew, J. P., Ernzerhof, M., and Burke, K. *J. Chem. Phys.* **105**, 9982–9958 (1996).

[123] Staroverov, V. N., Scuseria, G. E., Tao, J., and Perdew, J. P. *J. Chem. Phys.* **119**, 12129–12137 (2003).

[124] Paier, J., Marsman, M., and Kresse, G. *J. Chem. Phys.* **127**, 024103 (2007).

[125] Wang, L.-L. and Johnson, D. D. *J. Phys. Chem. B* **109**, 23113–23117 (2005).

[126] Ratsch, C., Fielicke, A., Kirilyuk, A., Behler, J., von Helden, G., Meijer, G., and Scheffler, M. *J. Chem. Phys.* **122**, 124302 (2005).

[127] Ricks, A. M., Bakker, J. M., Douberly, G. E., and Duncan, M. A. *J. Phys. Chem. A* **113**, 4701–4708 (2009).

[128] Johansson, M. P., Lechtken, A., Schooss, D., Kappes, M. M., and Furche, F. *Phys. Rev. A* **77**, 053202 (2008).

[129] Weis, P., Welz, O., Vollmer, E., and Kappes, M. M. *J. Chem. Phys.* **120**, 677–684 (2004).

[130] Reddy, B. V., Khanna, S. N., and Dunlap, B. I. *Phys. Rev. Lett.* **70**, 3323–3326 (1993).

[131] Cox, A. J., Louderbeck, J. G., and Bloomfield, L. A. *Phys. Rev. Lett.* **71**, 923–926 (1993).

[132] Knickelbein, M. B. *Phys. Rev. Lett.* **86**, 5255–5257 (2001).

[133] Briere, T. M., Sluiter, M. H. F., Kumar, V., and Kawazoe, Y. *Phys. Rev. B* **66**, 064412 (2002).

[134] Gloess, A. N., Schneider, H., Weber, J. M., and Kappes, M. M. *J. Chem. Phys.* **128**, 114312 (2008).

[135] Harb, M., Rabilloud, F., and Simon, D. *J. Chem. Phys.* **131**, 174302 (2009).

[136] Harding, D., Mackenzie, S. R., and Walsh, T. R. *J. Phys. Chem. B.* **110**, 18272–18277 (2006).

[137] Guilhaus, M., Selby, D., and Mlynski, V. *Mass Spectrom. Rev.* **19**, 65–107 (2000).

[138] Berg, C., Schindler, T., Niedner-Schatteburg, G., and Bondybey, V. E. *J. Chem. Phys.* **102**, 4870–4884 (1995).

[139] Cheng, P. Y., Wiley, K. F., and Duncan, M. A. *Chem. Phys. Lett.* **163**, 469–474 (1989).

[140] Vidali, G., Ihm, G., Kim, H.-Y., and Cole, M. W. *Surf. Sci. Rep.* **12**, 135–181 (1991).

[141] Cameron, A. E. and Eggers, Jr., D. F. *Rev. Sci. Instrum.* **19**, 605–607 (1948).

[142] Manura, D. J. and Dahl, D. A. *SIMION Version 8.0 User Manual*. Scientific Instrument Services Inc., (2007).

[143] Jacobs, D. C., Madix, R. J., and Zare, R. N. *J. Chem. Phys.* **85**, 5469–5479 (1986).

[144] Johnson, P. M. *Acc. Chem. Res.* **13**, 20–26 (1980).

[145] Zare, R. N. *Angular Momentum: Understanding Spatial Aspects in Chemistry and Physics*. John Wiley & Sons, (1988).

[146] Brown, J. M., Cole, A. R. H., and Honey, F. R. *Mol. Phys.* **23**, 287–295 (1972).

[147] Luque, J. and Crosley, D. R. *LIFBASE: Database and Spectral Simulation Program (Version 1.6)*. SRI International Report MP 99-009, (1999).

[148] Li, S., Alemany, M. M. G., and Chelikowsky, J. R. *J. Chem. Phys.* **121**, 5893–5898 (2004).

[149] Matsuda, Y. and Bernstein, E. R. *J. Phys. Chem. A* **109**, 3803–3811 (2005).

[150] Ralchenko, Y., Kramida, A. E., and Reader, J. *NIST Atomic Spectra Database (version 3.1.5), [Online]. Available: http://physics.nist.gov/asd3 [2008, June 7].* National Institute of Standards and Technology, Gaithersburg, MD, (2008).

[151] Bernath, P. F. *Spectra of Atoms and Molecules*. Oxford University Press, (2005).

[152] Hopkins, W. S., Hamilton, S. M., and Mackenzie, S. R. *J. Chem. Phys.* **130**, 144308 (2009).

[153] Paul W. Merrill, A. J. D. and Keenan, P. C. *Astrophys. J.* **136**, 21 (1962).

[154] Kasai, P. H. *J. Chem. Phys.* **49**, 4979–4984 (1968).

[155] Cheung, A. S.-C., Taylor, A. W., and Merer, A. J. *J. Mol. Spectrosc.* **92**, 391–409 (1982).

[156] Adam, A. G., Barnes, M., Berno, B., Bower, R. D., and Merer, A. J. *J. Mol. Spectrosc.* **170**, 94–130 (1995).

[157] Cheung, A. S.-C., Hansen, R. C., and Merer, A. J. *J. Mol. Spectrosc.* **91**, 165–208 (1982).

[158] Merer, A. J., Huang, G., Cheung, A. S.-C., and Taylor, A. W. *J. Mol. Spectrosc.* **125**, 465–503 (1987).

[159] Lars Karlsson, Bo Lindgren, C. L. and Sassenberg, U. *J. Mol. Spectrosc.* **181**, 274–278 (1997).

[160] Harrington, J. and Weisshaar, J. C. *J. Chem. Phys.* **97**, 2809–2812 (1992).

[161] Ram, R. S., Bernath, P. F., Davis, S. P., and Merer, A. J. *J. Mol. Spectrosc.* **211**, 279–283 (2002).

[162] Ram, R. S. and Bernath, P. F. *J. Mol. Spectrosc.* **229**, 57–62 (2005).

[163] Wu, H. and Wang, L.-S. *J. Chem. Phys.* **108**, 5310–5318 (1998).

[164] Western, C. M. pgopher*, a Program for Simulating Rotational Structure, v. 7.0.101*. University of Bristol, http://pgopher.chm.bris.ac.uk/, (2010).

[165] J. A. Harrington, R. M. Seel, G. R. H. and Nicholls, R. W. *Identification atlas of molecular spectra. 7. The VO $C^4\Sigma^- - X^4\Sigma^-$ yellow-green and $B^4\Pi - X^4\Sigma^-$ red systems*. York University, Centre for Research in Experimental Space Science, Toronto, Ontario, (1970).

[166] Cheung, A. S.-C., Hansen, R. C., Lyyra, A. M., and Merer, A. J. *J. Mol. Spectrosc.* **86**, 526–533 (1981).

[167] Flory, M. A. and Ziurys, L. M. *J. Mol Spectrosc.* **247**, 76–84 (2008).

[168] Dyke, J. M., Gravenor, B. W. J., Hastings, M. P., and Morris, A. *J. Phys. Chem.* **89**, 4613–4617 (1985).

[169] Huang, G. and Merer, A. J. *J. Mol. Spectrosc.* **153**, 32–40 (1992).

[170] Cheung, A. S.-C., Hajigeorgiou, P. G., Huang, G., Huang, S.-Z., and Merer, A. J. *J. Mol. Spectrosc.* **163**, 443–458 (1994).

[171] Hopkins, W. S., Hamilton, S. M., and Mackenzie, S. R. *Chem. Phys. Lett.* **483**, 10–15 (2009).

[172] Riley, S. J. and Wilson, K. R. *Faraday Discuss. Chem. Soc.* **53**, 132–146 (1972).

[173] Diesen, R. W., Wahr, J. C., and Adler, S. E. *J. Chem. Phys.* **50**, 3635–3636 (1969).

[174] Ashfold, M. N. R., Nahler, N. H., Orr-Ewing, A. J., Vieuxmaire, O. P. J., Toomes, R. L., Kitsopoulos, T. N., Garcia, I. A., Chestakov, D. A., Wu, S.-M., and Parker, D. H. *Phys. Chem. Chem. Phys.* **8**, 26–53 (2006).

[175] Sobhy, M. A., Reveles, J. U., Gupta, U., Khanna, S. N., and Castleman, Jr., A. W. *J. Chem. Phys.* **130**, 054304 (2009).

[176] Chestakov, D. A., Zawadzka, A., Parker, D. H., Vidma, K. V., Baklanov, A. V., and Kochubei, S. A. *Rev. Sci. Instrum.* **76**, 026102 (2005).

[177] Chestakov, D. A., Parker, D. H., and Baklanov, A. V. *J. Chem. Phys.* **122**, 084302 (2005).

[178] Dixon, R. N. *J. Chem. Phys.* **122**, 194302 (2005).

[179] Zare, R. N. and Herschbach, D. R. *Proc. IEEE* **51**, 173–182 (1963).

[180] Xu, Z., Koplitz, B., and Wittig, C. *J. Chem. Phys.* **90**, 2692–2702 (1989).

[181] Schmiedl, R., Dugan, H., Meier, W., and Welge, K. H. *Z. Phys. A* **304**, 137–142 (1982).

[182] Tonokura, K., Matsumi, Y., Kawasaki, M., and Kasatani, K. *J. Chem. Phys.* **95**, 5065–5071 (1991).

[183] Gerber, G. and Möller, R. *Phys. Rev. Lett.* **55**, 814–817 (1985).

[184] Matsumi, Y., Tonokura, K., Kawasaki, M., Inoue, G., Satyapal, S., and Bersohn, R. *J. Chem. Phys.* **94**, 2669–2674 (1991).

[185] Dixon, R. N., Nightingale, J., Western, C. M., and Yang, X. *Chem. Phys. Lett.* **151**, 328–334 (1988).

[186] Schmiedl, R., Böttner, R., Zacharias, H., Meier, U., and Welge, K. H. *Opt. Commun.* **31**, 329–333 (1979).

[187] Chandler, D. W. and Houston, P. L. *J. Chem. Phys.* **87**, 1445–1447 (1987).

[188] Chandler, D. W., Thoman, Jr., J. W., Janssen, M. H. M., and Parker, D. H. *Chem. Phys. Lett.* **156**, 151–158 (1989).

[189] Bergmann, T., Martin, T. P., and Schaber, H. *Rev. Sci. Instrum.* **60**, 347–349 (1989).

[190] Pollard, J. E., Lichtin, D. A., Janson, S. W., and Cohen, R. B. *Rev. Sci. Instrum.* **60**, 3171–3180 (1989).

[191] Eppink, A. T. J. B. and Parker, D. H. *Rev. Sci. Instrum.* **68**, 3477–3484 (1997).

[192] Matthews, S. J., Willitsch, S., and Softley, T. P. *Phys. Chem. Chem. Phys.* **9**, 5656–5663 (2007).

[193] B. R. Cosofret, H. M. L. and Houston, P. L. *J. Chem. Phys.* **117**, 8787–8799 (2002).

[194] Lambert, H. M., Davis, E. W., Tokel, O., Dixit, A. A., and Houston, P. L. *J. Chem. Phys.* **122**, 174304 (2005).

[195] Romanescu, C., Manzhos, S., Boldovsky, D., Clarke, J., and Loock, H.-P. *J. Chem. Phys.* **120**, 767–777 (2004).

[196] Rakitis, T. P., Samartzis, P. C., Toomes, R. L., Tsigaridas, L., Coriou, M., Chestakov, D., Eppink, A. T. J. B., Parker, D. H., and Kitsopoulos, T. N. *Chem. Phys. Lett.* **364**, 115–120 (2002).

[197] Cruse, H. A. and Softley, T. P. *J. Chem. Phys.* **122**, 124303 (2005).

[198] Wei, J., Riedel, J., Kuczmann, A., Renth, F., and Temps, F. *Faraday Discuss.* **127**, 267–282 (2004).

[199] Hopkins, W. S., Woodham, A. P., Plowright, R. J., Wright, T. G., and Mackenzie, S. R. *J. Chem. Phys.* **132**, 214303 (2010).

[200] Rubio-Lago, L., Zaouris, D., Sakellariou, Y., Sofikitis, D., Kistopoulos, T. N., Wang, F., Yang, X., Cronin, B., Devine, A. L., King, G. A., Nix, M. G. D., Ashfold, M. N. R., and Xantheas, S. S. *J. Chem. Phys.* **127**, 064306 (2007).

[201] Nahler, N. H., Viexmaire, O. P. J., Jones, J. R., Ashfold, M. N. R., Eppink, A. T. J. B., Coriou, A. M., and Parker, D. H. *J. Phys. Chem. A* **108**, 8077–8083 (2004).

[202] Aguirre, F. and Pratt, S. T. *J. Chem. Phys.* **118**, 6318–6326 (2003).

[203] L. P., Raffael, K. D., Marc-André, Soep, B., Mestdagh, J.-M., Caillat, J., Taïeb, R., and Maquet, A. *Phys. Rev. Lett.* **99**, 103401 (2007).

[204] Chichinin, A. I., Gericke, K.-H., Kauczok, S., and Maul, C. *Int. Rev. Phys. Chem.* **28**, 607–680 (2009).

[205] Heck, A. J. R. and Chandler, D. W. *Annu. Rev. Phys. Chem.* **46**, 335–372 (1995).

[206] Smith, L. M., Keefer, D. R., and Sudharsanan, S. I. *J. Quant. Spectrosc. Radiat. Transfer* **39**, 367–373 (1988).

[207] Winterhalter, J., Maier, D., Honerkamp, J., Schyja, V., and Helm, H. *J. Chem. Phys.* **110**, 11187–11196 (1999).

[208] Vrakking, M. J. J. *Rev. Sci. Instrum.* **72**, 4084–4089 (2001).

[209] Renth, F., Riedel, J., and Temps, F. *Rev. Sci. Instrum.* **77**, 033103 (2006).

[210] Dribinski, V., Ossadtchi, A., Mandelshtam, V. A., and Reisler, H. *Rev. Sci. Instrum.* **73**, 2634–2642 (2002).

[211] Garcia, G. A., Nahon, L., and Powis, I. *Rev. Sci. Instrum.* **75**, 4989–4996 (2004).

[212] Bordas, C., Paulig, F., Helm, H., and Huestis, D. L. *Rev. Sci. Instrum.* **67**, 2257–2268 (1996).

[213] Zhao, K., Colvin, T., Hill III, W. T., and Zhang, G. *Rev. Sci. Instrum.* **73**, 3044–3050 (2002).

[214] Roberts, G. M., Nixon, J. L., Lecointre, L., Wrede, E., and Verlet, J. R. R. *Rev. Sci. Instrum.* **80**, 053104 (2009).

[215] Hammer, B. and Nørskov, J. K. *Nature* **376**, 238–240 (1995).

[216] Special issue on gold cluster chemistry. *Chem. Soc. Rev.* **37**, 1745–2139 (2008).

[217] Goodman, D. W. *Nature* **454**, 948–949 (2008).

[218] Valden, M., Lai, X., and Goodman, D. W. *Science* **281**, 1647–1650 (1998).

[219] Edwards, P. P. and Meurig Thomas, J. *Angew. Chem. Int. Ed.* **46**, 5480–5486 (2007).

[220] Lemire, C., Meyer, R., Shaikhutdinov, S., and Freud, H.-J. *Angew. Chem. Int. Ed.* **43**, 118–121 (2004).

[221] Mills, G., Gordon, M. S., and Metiu, H. *J. Chem. Phys.* **118**, 4198–4205 (2003).

[222] Lian, L., Hackett, P. A., and Rayner, D. M. *J. Chem. Phys.* **99**, 2583–2590 (1993).

[223] Gilb, S., Weis, P., Furche, F., Ahlrichs, R., and Kappes, M. M. *J. Chem. Phys.* **116**, 4094–4101 (2002).

[224] Furche, F., Ahlrichs, R., Weis, P., Jacobs, C., Gilb, S., Bierweiler, T., and Kappes, M. M. *J. Chem. Phys.* **117**, 6982–6990 (2002).

[225] Xing, X., Yoon, B., Landman, U., and Parks, J. H. *Phys. Rev. B* **74**, 165423 (2006).

[226] Johansson, M. P., Lechtken, A., Schooss, D., Kappes, M. M., and Furche, F. *Phys. Rev. A* **77**, 053202 (2008).

[227] Gruene, P., Rayner, D. M., Redlich, B., van der Meer, A. F. G., Lyon, J. T., Meijer, G., and Fielicke, A. *Science* **321**, 674–676 (2008).

[228] Bulusu, S., Li, X., Wang, L.-S., and Zeng, X. C. *Proc. Nat. Ac. Sci.* **103**, 8326–8330 (2006).

[229] Li, J., Li, X., Zhai, H.-J., and Wang, L.-S. *Science* **299**, 864–867 (2003).

[230] Handschuh, H., Ganteför, G., Bechthold, P. S., and Eberhardt, W. *J. Chem. Phys.* **100**, 7093–7100 (1994).

[231] Häkkinen, H., Yoon, B., Landman, U., Li, X., Zhai, H.-J., and Wang, L.-S. *J. Phys. Chem. A* **107**, 6168–6175 (2003).

[232] Vogen, M., Hansen, K., Herlert, A., and Schweikhard, L. *Eur. Phys. J. D* **16**, 73–76 (2001).

[233] Häkkinen, H. *Chem. Soc. Rev.* **37**, 1847–1859 (2008).

[234] Pyykkö, P. *Angew. Chem. Int. Ed.* **43**, 4412–4456 (2004).

[235] Pyykkö, P. *Inorg. Chim. Acta* **358**, 4113–4130 (2005).

[236] Simard, B. and Hackett, P. A. *J. Chem. Phys.* **142**, 310–318 (1990).

[237] James, A. M., Kowalczyk, P., Simard, B., Pinegar, J. C., and Morse, M. D. *J. Mol. Spectrosc.* **168**, 248–257 (1994).

[238] Morse, M. D. *Chem. Rev.* **86**, 1049–1109 (1986).

[239] Okazaki, T., Saito, Y., and Kasuya, A. *Mol. Phys.* **96**, 143–145 (1999).

[240] Lecoultre, S., Rydlo, A., Félix, C., and Harbich, W. *Eur. Phys. J. D* **52**, 187–190 (2009).

[241] Fedrigo, S., Harbich, W., and Buttet, J. *J. Chem. Phys.* **99**, 5712–5717 (1993).

[242] Idrobo, J. C., Walkosz, W., Yip, S. F., Öğüt, S., Wang, J., and Jellinek, J. *Phys. Rev. B* **76**, 205422 (2007).

[243] Itkin, I. and Zaitsevskii, A. *Chem. Phys. Lett.* **374**, 143–150 (2003).

[244] Wrede, E., Laubach, S., Schulenberg, S., Brown, A., Wouters, E. R., Orr-Ewing, A. J., and Ashfold, M. N. R. *J. Chem. Phys.* **114**, 2629–2646 (2001).

[245] James, A. M., Kowalczyk, P., Simard, B., Pinegar, J. C., and Morse, M. D. *J. Mol. Spectrosc.* **168**, 248–257 (1994).

[246] Sansonetti, J., Martin, W., and Young, S. *Handbook of Basic Atomic Spectroscopic Data (version 1.1.2). [Online] Available: http://physics.nist.gov/Handbook [2010, August 30]*. National Institute of Standards and Technology, Gaithersburg, MD, (2005).

[247] Das, K. K. and Balasubramanian, K. *J. Mol. Spectrosc.* **140**, 280–294 (1990).

[248] Gallagher, T. F. *Rydberg atoms*. Cambridge University Press, (1994).

[249] Ding, G. J., Shang, R. C., Chang, L. F., Wen, K. W., Hui, Q., and Chen, D. Y. *J. Phys. B: At. Mol. Opt. Phys.* **22**, 1555–1561 (1989).

[250] Brown, C. M. and Ginter, M. L. *J. Opt. Soc. Am.* **68**, 243–246 (1978).

[251] Dubko, S. F., Efremov, V. A., Gerasimov, V. G., and MacAdam, K. B. *J. Phys. B: At. Mol. Opt. Phys.* **38**, 1107–1118 (2005).

[252] Loock, H.-P., Beaty, L. M., and Simard, B. *Phys. Rev. A* **59**, 873–875 (1999).

[253] Civiš, S., Matulková, I., Cihelka, J., Kawaguchi, K., Chernov, V. E., and Buslov, E. Y. *Phys. Rev. A* **81**, 012510 (2010).

[254] Hotop, H. and Lineberger, W. C. *J. Phys. Chem. Ref. Data* **14**, 731–750 (1985).

[255] Herzberg, G. *Molecular Spectra and Molecular Stucture I. Spectra of Diatomic Molecules*, volume 1. Van Nostron Reinhold Company, (1950).

[256] Hamilton, S. M., Hopkins, W. S., Harding, D. J., Walsh, T. R., Gruene, P., Haertelt, M., Fielicke, A., Meijer, G., Mackenzie, S. R., and Neville, S. *J. Am. Chem. Soc.* **132**, 1448–1449 (2010).

[257] Oepts, D., van der Meer, A. F. G., and van Amersfoort, P. W. *Infrared Phys. Technol.* **36**, 297–308 (1995).

[258] Harding, D. J., Walsh, T. R., Hamilton, S. M., Hopkins, W. S., Mackenzie, S. R., Gruene, P., Haertelt, M., Meijer, G., and Fielicke, A. *J. Chem. Phys.* **132**, 011101 (2010).

[259] Harding, D. J., Gruene, P., Haertelt, M., Meijer, G., Fielicke, A., Hamilton, S. M., Hopkins, W. S., Mackenzie, S. R., Neville, S., and Walsh, T. R. *J. Chem. Phys.* **133**, 214304 (2010).

[260] Hansen, K., Herlert, A., Schweikhard, L., and Vogel, M. *Phys. Rev. A* **73**, 063202 (2006).

[261] Terasaki, A. *J. Phys. Chem. A* **111**, 7671–7689 (2007).

[262] Gregoire, G., Velasquez, J., and Duncan, M. A. *Chem. Phys. Lett.* **349**, 451–457 (2001).

[263] Fielicke, A., Gruene, P., Meijer, G., and Rayner, D. M. *Surf. Sci.* **603**, 1427–1433 (2009).

[264] Fielicke, A., von Helden, G., Meijer, G., Simard, B., and Rayner, D. M. *Phys. Chem. Chem. Phys.* **7**, 3906–3909 (2005).

[265] Koretsky, G. M. and Knickelbein, M. B. *Chem. Phys. Lett.* **267**, 485–490 (1997).

[266] Hirabayashi, S., Okawa, R., Ichihashi, M., Kawazoe, Y., and Kondow, T. *J. Chem. Phys.* **130**, 164304 (2009).

[267] Swart, I., de Groot, F. M. F., Weckhyusen, B. M., Gruene, P., Meijer, G., and Fielicke, A. *J. Phys. Chem. A* **112**, 1139–1149 (2008).

[268] Davis, C. C. *Lasers and Electro-Optics*. Cambridge University Press, (1996).

[269] von Helden, G., van Heijnsbergen, D., and Meijer, G. *J. Phys. Chem. A* **107**, 1671–1688 (2003).

[270] Bakker, J. M., Satink, R. G., von Helden, G., and Meijer, G. *Phys. Chem. Chem. Phys.* **4**, 24–33 (2002).

[271] Zhdanov, V. P. and Kasemo, B. *Surf. Sci. Rep.* **29**, 30–90 (1997).

[272] Vernon, P. D. F., Green, M. L. H., Cheetham, A. K., and Ashcroft, A. T. *Catal. Lett.* **6**, 181–186 (1990).

[273] Wei, J. and Iglesia, E. *J. Catal.* **225**, 116–127 (2004).

[274] Balteanu, I., Balaj, O. P., Fox-Beyer, B. S., Rodrigues, P., Barros, M. T., Moutinho, A. M. C., Costa, M. L., Beyer, M. K., and Bondybey, V. E. *Organometallics* **23**, 1978–1985 (2004).

[275] Adlhart, C. and Uggerud, E. *J. Chem. Phys.* **123**, 214709 (2005).

[276] Berg, C., Beyer, M., Achatz, U., Joos, S., Niedner-Schatteburg, G., and Bondybey, V. E. *J. Chem. Phys.* **108**, 5398–5403 (1998).

[277] Cox, A. J., Louderbeck, J. G., Aspel, S. E., and Bloomfield, L. A. *Phys. Rev. B* **49**, 12295–12298 (1994).

[278] Beyer, M. K. and Knickelbein, M. B. *J. Chem. Phys.* **126**, 104301 (2007).

[279] Lide, D. R., editor. *CRC Handbook of Chemistry and Physics*. CRC Press, (2008-2009).

[280] Futschek, T., Marsman, M., and Hafner, J. *J. Phys.: Condens. Matter* **17**, 5927–5963 (2005).

[281] Bertin, V., Lopez-Rendón, R., del Angel, G., Poulain, E., Avilés, R., and Uc-Rosas, V. *Int. J. Quantum Chem.* **110**, 1152–1164 (2009).

[282] Aguilera-Granja, F., Rodríguez-López, J. L., Michaelian, K., Berlanga-Ramírez, E. O., and Vega, A. *Phys. Rev. B* **66**, 224410 (2002).

[283] Bae, Y.-C., Osanai, H., Kumar, V., and Kawazoe, Y. *Phys. Rev. B* **70**, 195413 (2004).

[284] Bae, Y.-C., Kumar, V., Osanai, H., and Kawazoe, Y. *Phys. Rev. B* **72**, 125427 (2005).

[285] Aguilera-Granja, F., Balbás, L. C., and Vega, A. *J. Phys. Chem. A* **113**, 13483–13491 (2009).

[286] Shetty, S., Strych, S., Jansen, A. P. J., and van Santen, R. A. *Can. J. Chem.* **87**, 824–831 (2009).

[287] Wang, L.-L. and Johnson, D. D. *Phys. Rev. B* **75**, 235405 (2007).

[288] Sun, Y., Fournier, R., and Zhang, M. *Phys. Rev. A* **79**, 043202 (2009).

[289] Matsushima, T. and Kokalj, A. *Surf. Sci.* **601**, 3996–4000 (2007).

[290] Imamura, K., Horino, H., Rzeźnicka, I., Kobal, I., Kokalj, A., Ohno, Y., Nieuwenhuys, B. E., Hiratsuka, A., and Matsushima, T. *Surf. Sci.* **566–568**, 1076–1081 (2004).

[291] Matsushima, T., Imamura, K., Horino, H., Hiratsuka, A., Ma, Y.-S., Rzeźnicka, I., and Nakagoe, O. *App. Surf. Sci.* **244**, 141–144 (2005).

[292] Wehner, S., Paffett, M. T., and Zaera, F. *J. Phys. Chem. B* **108**, 18683–18692 (2004).

[293] Li, Y. and Bowker, M. *Surf. Sci.* **348**, 67–76 (1996).

[294] Kokalj, A. and Matsushima, T. *J. Chem. Phys.* **122**, 034708 (2005).

[295] Haq, S. and Hodgson, A. *Surf. Sci.* **463**, 1–10 (2000).

[296] Avery, N. R. *Surf. Sci.* **131**, 501–510 (1983).

[297] Madey, T. E., Avery, N. R., Anton, A. B., Toby, B. H., and Weinberg, W. H. *J. Vac. Sci. Technol. A* **1**, 1220–1221 (1983).

[298] Ricart, J. M., Ample, F., Clotet, A., Curulla, D., Niemantsverdriet, J. W., Paul, J. F., and Pérez-Ramírez, J. *J. Catal.* **232**, 179–185 (2005).

[299] Paul, J.-F., Pérez-Ramírez, J., Ample, F., and Ricart, J. M. *J. Phys. Chem. B* **108**, 17921–17927 (2004).

[300] Gruene, P., Meijer, G., and Fielicke, A. *J. Chem. Phys.* **127**, 234307 (2007).

[301] *TURBOMOLE V6.1 2009, a development of University of Karlsruhe and Forschungszentrum Karlsruhe GmbH, 1989-2007, TURBOMOLE GmbH, since 2007; available from* `http://www.turbomole.com`.

[302] Perdew, J. P., Tao, J., Staroverov, V. N., and Scuseria, G. E. *J. Chem. Phys.* **120**, 6898–6911 (2004).

[303] Jensen, K. P. *J. Phys. Chem. A* **113**, 10133–10141 (2009).

[304] Weigend, F. and Ahlrichs, R. *Phys. Chem. Chem. Phys.* **7**, 3297–3305 (2005).

[305] Swart, I., de Groot, F. M. F., Weckhuysen, B. M., Rayner, D. M., Meijer, G., and Fielicke, A. *J. Am. Chem. Soc.* **130**, 2126–2127 (2008).

[306] Weigend, F., Häser, M., Patzelt, H., and Ahlrichs, R. *Chem. Phys. Lett.* **294**, 143–152 (1998).

[307] Klopper, W. and Samson, C. C. M. *J. Chem. Phys.* **116**, 6397–6410 (2002).

[308] Eichkorn, K., Treutler, O., Öhm, H., Häser, M., and Ahlrichs, R. *Chem. Phys. Lett.* **240**, 283–290 (1995).

[309] Weigend, F., Köhn, A., and Hättig, C. *J. Chem. Phys.* **116**, 3175–3183 (2002).

[310] Wales, D. J. and Doye, J. P. K. *J. Phys. Chem. A* **101**, 5111–5116 (1997).

[311] Jensen, F. *Introduction to Computational Chemistry*, chapter 12. John Wiley & Sons (2007).

[312] Deglmann, P., Furche, F., and Ahlrichs, R. *Chem. Phys. Lett.* **362**, 511–518 (2002).

[313] Helgaker, T. *Chem. Phys. Lett.* **182**, 503–510 (1991).

[314] Harding, D. J. *Structure and Reactivity of Transition Metal Clusters*. PhD thesis, University of Warwick, (2008).

[315] Teffo, J.-L. and Chédin, A. *J. Mol. Spectrosc.* **135**, 389–409 (1989).

[316] Hussain, G., Rahman, M. M., and Sheppard, N. *Specrochimica Acta* **47A**, 1525–1530 (1991).

[317] Henderson, M. A., Szanyi, J., and Peden, C. H. F. *Catal. Today* **85**, 251–266 (2003).

[318] Morterra, C., Boccuzzi, F., Coluccia, S., and Ghiotti, G. *J. Catal.* **65**, 231–234 (1980).

[319] Miller, T. M. and Grassian, V. H. *J. Am. Chem. Soc.* **117**, 10969–10975 (1995).

[320] Rusu, C. N. and J. T. Yates, J. *J. Phys. Chem. B* **105**, 2596–2603 (2001).

[321] Borello, E., Cerruti, L., Ghiotti, G., and Guglielminotti, E. *Inorg. Chim. Acta* **6**, 45–48 (1972).

[322] Citir, M. and Metz, R. B. *J. Chem. Phys.* **128**, 024307 (2008).